University of Alberta

Two-Dimensional Modeling of the Scoliotic Spine

by

Jody L. Lilley ©

A thesis submitted to the Faculty of Graduate Studies and Research in partial
fulfillment of the requirements for the degree of Master of Science

Department of Mechanical Engineering

Edmonton, Alberta
Spring, 2006

Library and
Archives Canada

Published Heritage
Branch

395 Wellington Street
Ottawa ON K1A 0N4
Canada

Bibliothèque et
Archives Canada

Direction du
Patrimoine de l'édition

395, rue Wellington
Ottawa ON K1A 0N4
Canada

Your file Votre référence
ISBN: 0-494-13844-0
Our file Notre référence
ISBN: 0-494-13844-0

NOTICE:
The author has granted a non-exclusive license allowing Library and Archives Canada to reproduce, publish, archive, preserve, conserve, communicate to the public by telecommunication or on the Internet, loan, distribute and sell theses worldwide, for commercial or non-commercial purposes, in microform, paper, electronic and/or any other formats.

The author retains copyright ownership and moral rights in this thesis. Neither the thesis nor substantial extracts from it may be printed or otherwise reproduced without the author's permission.

AVIS:
L'auteur a accordé une licence non exclusive permettant à la Bibliothèque et Archives Canada de reproduire, publier, archiver, sauvegarder, conserver, transmettre au public par télécommunication ou par l'Internet, prêter, distribuer et vendre des thèses partout dans le monde, à des fins commerciales ou autres, sur support microforme, papier, électronique et/ou autres formats.

L'auteur conserve la propriété du droit d'auteur et des droits moraux qui protège cette thèse. Ni la thèse ni des extraits substantiels de celle-ci ne doivent être imprimés ou autrement reproduits sans son autorisation.

In compliance with the Canadian Privacy Act some supporting forms may have been removed from this thesis.

While these forms may be included in the document page count, their removal does not represent any loss of content from the thesis.

Conformément à la loi canadienne sur la protection de la vie privée, quelques formulaires secondaires ont été enlevés de cette thèse.

Bien que ces formulaires aient inclus dans la pagination, il n'y aura aucun contenu manquant.

Canada

For Mom

Abstract

Scoliosis is a complex three-dimensional deformation of the spine and thoracic cage for which surgery is used in severe cases to straighten the spine. A patient specific finite element model of the scoliotic spine would enable surgeons to test different surgical procedures, thereby optimizing correction of the spine.

A two-dimensional model of the scoliotic spine and thoracic cage was created. The model incorporates nonlinear features, including contact elements, nonlinear geometry, and nonlinear material properties. In addition, several time saving features such as condensation and sparse matrix storage have been utilized. The material properties of the intervertebral discs were found to have the greatest effect on the spinal correction, while the vertebral bodies, sternum and intertransverse ligaments were found to have little to no effect. Further testing on the articular facets and thoracic cage will be required once the model is upgraded to a complete three-dimensional pre-surgical tool.

Acknowledgements

I would like to take this opportunity to thank everyone who helped and supported me in completing this research.

Thank you to my supervisor, Dr. Ken Fyfe for always asking the right questions when I was stuck and for letting me work things out at my own pace. I would also like to thank Dr. Don Raboud for taking on a supervisory role so late in the project.

Thanks to Jim Raso of the Glenrose Rehabilitiation Hospital for his guidance throughout my research. I would also like to thank Julie Mondoux for answering all of my questions about surgical procedures and for always going an extra step in helping me find the information I was looking for.

I would also like to thank everyone who struggled through the exams and assignments with me, especially Maureen, Kelly, Steve, and Simon. With your help, the work was almost fun!

And most of all, thank you to my family for all of their support. Special thanks to Judianne and Jenn for the many hours spent entertaining Nathan so that I could write. And, thank you to my husband and best friend, David, for his ongoing support and confidence in my abilities.

Contents

1 Introduction 1
- 1.1 Objectives 2
- 1.2 Thesis Outline 2

2 Anatomy and Biomechanics of the Vertebral Column and Ribcage 4
- 2.1 The Vertebral Column 6
  - 2.1.1 Vertebra 6
  - 2.1.2 Intervertebral Discs 12
  - 2.1.3 Ligaments 15
- 2.2 Thoracic Cage 16
- 2.3 Material Properties 18

3 Adolescent Idiopathic Scoliosis 20
- 3.1 Characteristics 20
  - 3.1.1 Lateral Deviation 20
  - 3.1.2 Axial Rotation 23
  - 3.1.3 Ribcage Deformity 26
- 3.2 Treatment 26
  - 3.2.1 Observation 26
  - 3.2.2 Bracing 26
  - 3.2.3 Surgery 27

4 Finite Element Analysis 30
- 4.1 Overview of the Finite Element Method 30
- 4.2 Derivation of the Finite Element Equations 30
- 4.3 Element Derivations 32
  - 4.3.1 Elastic Truss Element 32
  - 4.3.2 Nonlinear Strain Truss Element 32
  - 4.3.3 Triangular Element 33
  - 4.3.4 Quadrilateral Element 35

4.4 Matrix Storage 35
4.5 Condensation 36
4.6 Constraint Application 38
  4.6.1 Allaire's Method 38
  4.6.2 Elimination Method 38
  4.6.3 Penalty Approach 39
  4.6.4 Constraint Equations 40
4.7 Nonlinearities 41
  4.7.1 Material Nonlinearities 44
  4.7.2 Geometric Nonlinearities 44
  4.7.3 Contact Elements 48

5 Existing Finite Element Models of the Spine **51**
5.1 A Mechanical Model of the Normal Human Spine 51
5.2 A Finite Element Model of the Ribcage 52
5.3 Simulation of Scoliosis Derotation Maneuver 53
5.4 Simulation of Scoliosis Surgery using FEM 53
5.5 Modeling of the Spine and Thorax for the Analysis of Scoliotic Deformities Using FEM 54
5.6 Virtual Reality Scoliosis Surgery Simulator 55
5.7 Conclusions 56

6 The Scoliotic Spine Model **57**
6.1 Graphical User Interface 57
6.2 Creating the Geometry 58
  6.2.1 Vertebrae and Intervertebral Discs 58
  6.2.2 Ligaments 73
  6.2.3 Thoracic Cage 74
6.3 Applying Boundary Conditions 76
6.4 Creating Loads 78
6.5 Nonlinear Solver 79
6.6 Results 80
6.7 Additional Features 80
  6.7.1 Create ANSYS file 80
  6.7.2 Condensation Optional 84
  6.7.3 List Options 84
  6.7.4 Display Options 86
  6.7.5 Print to Screen 89

7 Results **91**
7.1 Linear Validation of the Model 91
7.1.1 Hand Calculation 92
7.1.2 ANSYS 92
7.2 Nonlinear Validation of the Model 92
7.2.1 Test Case 92
7.2.2 Convergence Testing 94
7.2.3 Nonlinear Verification 99
7.3 Sensitivity Analysis 107
7.3.1 Material Properties 109
7.3.2 Facet Contact Elements 121
7.3.3 Load steps 121
7.4 Real Time Capabilities 128
7.4.1 Condensation 128
7.4.2 Sparse Matrix Storage 129
7.4.3 Application of Boundary Conditions 131

8 Discussion **133**
8.1 Overview 133
8.2 Conclusions 133
8.3 Future Work 135
8.3.1 Expansion to a Three-dimensional Model 135
8.3.2 Improved Modeling of Scoliotic Surgery 136
8.3.3 Real Time Capabilities 137
8.3.4 Improve ease of use by Surgeons 139

A Element Derivations **144**
A.1 Nonlinear Strain-Displacement Truss Element 144
A.2 Nonlinear Strain-Displacement Beam Element 145

List of Tables

2.1 Material Properties of the Vertebral Column and Thoracic Cage . . . 19

6.1 Vertebral Body Dimension Notations 60

7.1 Loading conditions for the sensitivity analysis 94
7.2 Original Material Properties 109

8.1 Number of Elements Required for Three-dimensional Model 138

List of Figures

2.1 Schematic of the sectional planes used to describe anatomical features. Modified from Integrated Publishing[14]. 5

2.2 Flexion, extension, lateral bending and axial rotation of the spine. Modified from Kapandji[15]. 5

2.3 Sagittal view of the human vertebral column. Modified from Netter[22] 7

2.4 Lateral view and inferior view of a typical vertebra. Modified from Martini[19]. 9

2.5 Posterior oblique view of a typical thoracic and a typical lumbar vertebra. Modified from Kapandiji[15]. 10

2.6 The role of the facet joints in the thoracic and lumbar spine when subject to an axial torque. Modified from White & Panjabi[37]. . . . 10

2.7 Orientation of the facet joints. Card angle measurements are taken by first rotating the card angle from the transverse plane by an amount α followed by an amount β. Modified from Panjabi[24]. 11

2.8 Facet orientation of the vertebrae. Modified from Panjabi[24]. 11

2.9 Depiction of the intervertebral discs. Cutaway of laminated bands of annular fibers to show that adjacent bands of the fibers are oriented in opposite directions. Modifies from White & Panjabi[37]. 12

2.10 Internal forces acting withing the intervertebral disc during compression and tension. Modified from [15]. 13

2.11 Depiction of the movement of the intervertebral disc nucleus during extension, flexion, and lateral bending. Modified from [15]. 14

2.12 Illustration of the forces exerted on the intervertebral disc during axial rotation of the spine. Modified from [15]. 14

2.13 Ligaments of the Vertebral Column. 15

2.14 Stress-strain curve of a typical ligament in tension. Modified from Myklebust[21]. 16

2.15 Components of the thoracic cage. Modified from Netter[22]. 17

2.16 Superior view of the costovertebral articulation. 17

2.17 Left lateral view of the costovertebral joint. Modified from Netter[22]. 18

3.1 Depiction of a scoliotic curve. Modified from Keim[16]. 21
3.2 King Classification of scoliotic curves. Modified from King et al.[17]. 21
3.3 Measurement of the Scoliotic curve. Modified from Pope et al.([28]), Keim[16], White & Panjabi[37]. 22
3.4 Vertebral and intervertebral disc wedge angles. Modified from Stokes et al. [31]. 23
3.5 Lateral bending tests performed to differentiate between structural curves and functional curves. As shown here, the lumbar curve is functional while the thoracic curve is structural. Modified from Keim[16]. 24
3.6 Axial rotation of the scoliotic spine. Modified from White et al.[37]. . 24
3.7 Axial deformation of the vertebrae typical in scoliosis patients. Modified from White et al.[37]. 25
3.8 Typical deformation of the thoracic cage in scoliosis patients. Modified from Keim[16]. 25
3.9 Sample hook typically used for scoliosis surgery. Modified from Zeller and Dubousset[39]. 27
3.10 Superior view of the insertion of pedicles screws into a vertebra. Modified from Spine-Health[30]. 28
3.11 Posterior View of sample instrument placement for a scoliotic curve. Note that only hooks are used in this example. Modified from Zeller and Dubousset[39]. 29

4.1 Flowchart of the basic steps involved in finite element analysis. Modified from Fyfe[11]. 31
4.2 Illustration of a two-dimensional truss element. 33
4.3 Illustration of a typical two-dimensional triangular element. 34
4.4 Transformation of a two-dimensional isoparametric element from the x-y plane into a unit element in the η-ξ plane. 35
4.5 Representation of a typical global stiffness matrix. The markers represent the non-zero members. 36
4.6 Illustraion of condensation, a procedure used to decrease the number of degrees of freedom in a system without compromising accuracy. . . 37
4.7 Depiction of the penalty approach applied to a beam element. 39
4.8 Illustration of an angled roller constraint. A constraint equation can be used to constrain the x and y deflection. 40
4.9 Illustration of a nonlinear solution not using iterations (A) and using the Newton-Raphson iterative technique (B). Modified from ANSYS[1]. 43
4.10 Modeling of a ligament placed in tension. For clarity, Newton Raphson iterative steps were not displayed in this figure. 44
4.11 Sample loading of a beam used to illustrate geometric nonlinearities. . 45

4.12 Nonlinear and linear deflection of the free end of a cantilever beam. Several load steps were required to obtain sufficient accuracy of the nonlinear solver. 47
4.13 Illustration of the Pinball algorithm to check for contact. Modified from ANSYS[1]. 49
4.14 Illustration of vector used to check for contact between point K and the target surface. 50

6.1 Graphical user interface of the current finite element model. 58
6.2 Anterior view of the vertebral body measurements obtained from Panjabi et al. Dimension notations shown in Table 6.1. Modified from Panjabi[24]. 59
6.3 Posterior view of the Spinal Model for Cobb angles $\alpha = 60\,°$, $\beta = 50\,°$, and Lumbar Obliquity, $LO = 10\,°$. 61
6.4 Graphical user interface of the 'Create Geometry' section of the Control Window. The entries for the test geometry are shown. 62
6.5 The top (a) and bottom (b) points are located for L4 and L5 using the geometric data from Panjabi et al. and the scoliotic parameters. . . 63
6.6 The beta curve is created by locating a geometric center, determining the curve length and assuming a starting angle of rotation of $L3$. . . . 63
6.7 The alpha curve is created by locating the geometric center and determining the required curve length. 64
6.8 The remaining vertebral superior to the alpha curve are created by assuming the vertebral body rotation decreases by 50% compared to the vertebra inferior to it. 64
6.9 The vertebral points for the defined scoliotic curve. 65
6.10 Location of the keypoints, numbered 1-10, from the data points previously described. 65
6.11 Vertebral body wedge angles described by Stokes et al.[31]. 66
6.12 Anterior view of the four locations recorded to be read into the finite element model. 67
6.13 Creation of the vertebral body keypoints from the recorded x-ray data. 67
6.14 Segregation of the vertebral body into 2 mesh areas. 68
6.15 Sample discretization of the vertebral bodies. 69
6.16 Location of the screw and hook hardpoints for the spinal model. . . . 70
6.17 Condensation of a vertebral body from 32 nodes to 18 nodes. 71
6.18 Articular facets are modeled as triangular elements on the superior vertebra which can contact the top of the inferior vertebra. 71

6.19 Facet height restrictions are placed on intervertebral spaces that are too large or too small as shown on the left side and right side of this model respectively. 72
6.20 Intertransverse ligaments are modeled as nonlinear two-dimensional cable elements connecting the transverse processes of adjacent vertebrae. 73
6.21 Mulitlinear material properties used for the intertransverse ligaments. 74
6.22 Thoracic model of the scoliotic spine. The thoracic cage is shown here comprised of 10 rib pairs and a sternum. 75
6.23 Constraint section of the graphical user interface. 76
6.24 Dialog box prompting the user to select the degree of freedom to be constrained. 77
6.25 Depiction of y-direction constraints applied to the bottom vertebra. . 77
6.26 Load application section withing the Control Window of the GUI. Loads must be applied one at a time. 78
6.27 Graphical depiction of a 200 N load applied to the left screw of $L1$. . 79
6.28 Control section for the nonlinear solver. The user can change the default number of load steps, the maximum allowable error, and the maximum number of iterations. 80
6.29 Flowchart illustrating the procedure for the nonlinear solver. Note that the dark grey boxes are part of the Newton-Raphson iteration, while the lighter grey boxes are indicate the steps within each load step. 81
6.30 Visual display of the corrected scoliotic geometry. The dark grey vertebral bodies show the initial geometry. 82
6.31 Results section of the graphical user interface. 82
6.32 File menu options available. 83
6.33 Drop down menu selection to toggle condensation on and off. 83
6.34 Illustration of the model with and without condensation used. 84
6.35 List menu options. 85
6.36 Sample list of loading conditions. 85
6.37 Sample midline discrepancy results for a test run. 86
6.38 Plot control options available. These options can also be accessed in the visual display window. 87
6.39 Discretization of vertebral bodies with and without condensation. . . 87
6.40 Display of element numbers for vertebrae and intervertebral disc elements. 88
6.41 Plotting control option to display the vertebra names. 88
6.42 Option to display α and β Cobb angles. 89
6.43 Display of the geometric midline ($x = 0$) to enhance visualization of the geometric deformity. 90

7.1 Validation test case on a single vertebral motion unit. 91
7.2 Illustration of the test case used for the sensitivity analysis. 93
7.3 Resulting correction of the test case scoliotic spine. Note the original geometry in the background. 95
7.4 Displacement of the center nodes of the vertebral bodies and intervertebral discs using the original material properties. 96
7.5 Locations of nodes 182, 412, and 634. The displacements of these nodes will be used to examine the effects of different parameters. . . . 97
7.6 Convergence testing of the test model. 98
7.7 Verification testing comparing the results from ANSYS and femSpine. Note that the intertransverse ligaments were omitted from the figure for clarity. 101
7.8 Location of intertransverse ligament #21. This ligament is subjected to the largest strain compared to the remaining 33 ligaments following the test run. 102
7.9 Location of intertransverse ligament #11. This ligament is subjected to the smallest strain compared to the remaining 33 ligaments following the test run. 102
7.10 Change in strain, modulus of elasticity, and length of intertransverse ligament #21 following each load step of the test run. 103
7.11 Change in strain, modulus of elasticity, and length of intertransverse ligament #11 following each load step of the test run. 104
7.12 Initial articular facet contact locations. Note that the contact status of these locations changed after the first load step as the resulting internal forces were pulling the joint apart. 105
7.13 Internal forces on the articular facet joints between vertebrae $T3$ - $T4$ and vertebrae $T8$ - $T9$. 106
7.14 Illustration of the initial geometry and the final geometry of the articular facets between $T12$ and $L1$. Contact occurs following load step #7. 107
7.15 Internal force acting on the left articular facet joint between vertebrae $T12$ - $L1$ due to contact. 108
7.16 Resulting displacement of the spine using $E = 100\,\text{MPa}$ and $E = 12000\,\text{MPa}$ for the vertebral bodies. 110
7.17 Deflection of nodes 634 (top graph) and 182 (bottom graph) using vertebral body stiffnesses ranging from $E = 50\,\text{MPa}$ to $E = 15000\,\text{MPa}$. 111
7.18 x deflection of the centerline nodes of the spine using a varying modulus of elasticity for the intervertebral discs. 112
7.19 y deflection of the centerline nodes of the spine using a varying modulus of elasticity for the intervertebral discs. 113

7.20 Deflection of nodes 634 (top graph) and 182 (bottom graph) using intervertebral disc stiffnesses ranging from $E = 1\,\mathrm{MPa}$ to $E = 10\,\mathrm{MPa}$. 114
7.21 Histogram illustrating the final change in strain of the intertransverse ligaments using the test run. 115
7.22 Change in displacement of the centerline nodes of the spine due to using the nonlinear strain-displacement truss element to model the intertransverse ligaments instead of the linear strain-displacement truss element. 116
7.23 Effect of prestress on the spinal deflection. Note that a positive change in displacement indicates a larger deflection for the test case without prestress. 117
7.24 Resulting displacement of the spine for different values of the modulus of elasticity for the intertransverse ligaments. 118
7.25 Deflection of nodes 634 (top graph) and 182 (bottom graph) with varying stiffnesses of the intertransverse ligaments. 119
7.26 Resulting displacement of the spine using $E = 10\,\mathrm{MPa}$, $E = 100\,\mathrm{MPa}$, and $E = 12000\,\mathrm{MPa}$ for the ribs. 120
7.27 Deflection of nodes 634 (top graph), 412 (middle graph) and 182 (bottom graph) using rib stiffnesses ranging from $E = 10\,\mathrm{MPa}$ to $E = 12000\,\mathrm{MPa}$. 122
7.28 Resulting displacement of the spine using $E = 2\,\mathrm{MPa}$ and $E = 1000\,\mathrm{MPa}$ for the sternum to ground truss element. 123
7.29 Deflection of nodes 634 (top graph) and 182 (bottom graph) using sternum to ground stiffnesses ranging from $E = 1\,\mathrm{MPa}$ to $E = 1000\,\mathrm{MPa}$. 124
7.30 Change in deflection of the spine with and without contact elements (No Contact−Contact). 125
7.31 Centerline node deflections of the spine for 1 load step and 10 load steps. 126
7.32 Calculated displacement of node 634 and 182 in the y and x directions respectively for a varying number of load steps. 127
7.33 Plot of the spinal displacement with and without using condensed vertebrae stiffness matrices. 129
7.34 Illustration of the unconstrained global stiffness matrix for the test case. 130
7.35 Modified profile report from Matlab. 132

8.1 Current time requirements to solve femSpine for an increasing number of elements. 139

Chapter 1

Introduction

Scoliosis is a complex three-dimensional deformation of the spine and thoracic cage. The majority of scoliosis cases are known as Adolescent Idiopathic Scoliosis, AIS, meaning that the deformity begins in adolescence and that the cause is unknown. Oftentimes, the deformity is minimal and can be corrected with exercises and/or bracing. However, the deformity can become quite large, at which point surgery is recommended. This highly invasive surgery involves instrumenting the vertebrae with hooks and screws and then attaching metal rods to straighten the spine. Currently, each surgeon performing the correction has his own favorite method and instruments to correct the spine. As a result, the surgical method used is more dependent on the surgeon performing the procedure than on the scoliotic deformity itself.

To reduce this effect and to further understand the mechanics of the scoliotic spine, several models of the spine have been created [2] [27] [31] [33] [35] [36]. Ideally, the models could be used by surgeons to test different surgical procedures to determine the ideal method for each individual patient. However, these models are not appropriate for this use for several reasons. Most of the current models were created using a commercial finite element analysis package [2] [31] [33] [35] [36], which is unable to account for all of the nonlinear properties inherent to the surgical procedure, is too complex for an untrained surgeon to use, and is too general to enable real time processing. In addition, some of the models were based on normal spinal motions and articulations and do not account for scoliotic deformities[35] [36]. Additionally, due to the large variation in scoliotic deformities between patients, it is imperative to use patient specific geometry and material properties to obtain accurate results for each patient. Furthermore, not all of the models allow for large deformations which occur during scoliosis surgery [36].

Based on these deficiencies of the current models, there is a need to create a pre-surgical tool that is patient specific in terms of geometry and material properties, incorporates large deflections, enables real time processing and includes a user friendly interface that surgeons will use.

1.1 Objectives

The long term objective of this study is to develop a three-dimensional model of the scoliotic vertebral column and thoracic cage for use as a pre-operative tool by the surgeon. Such a tool will enable testing of the various surgical procedures currently used to determine the ideal method for each individual patient.

The first step towards this goal was to create and validate a two-dimensional prototype of the computer model which incorporates all of the necessary features of the final model including nonlinear geometry capabilities to account for large deflection, nonlinear material properties to properly model components of the spine, and contact elements to represent the articular facets. This model was then evaluated using convergence testing, a sensitivity analysis, and spinal unit comparison tests to determine the feasibility of achieving a pre-surgical tool. This first step is the basis for the current work presented.

1.2 Thesis Outline

An introduction to the anatomy of the normal vertebral column and thoracic cage will be covered in Chapter 2 before getting into a detailed description of scoliosis in Chapter 3. Some basic concepts of finite element modeling will be reviewed in Chapter 4 in addition to a description of several advanced techniques required for the model. Chapter 5 will consist of a detailed description of the advantages and limitations of several finite element models of the spine currently available.

With the problem outlined and the required principles understood, a detailed account of the model is included in Chapter 6. Chapter 7 contains several validation tests, sensitivity analyses and real time comparison testing of the current model. A discussion regarding the potential of the model and the future work required to attain the final goal of a pre-surgical tool for scoliosis surgery is included in Chapter 8.

Chapter 2

Anatomy and Biomechanics of the Vertebral Column and Ribcage

This chapter will describe the basic anatomy and biomechanics of the human spine and thorax necessary for a complete understanding of the deformations involved in scoliosis.

Before beginning an in depth discussion of the anatomy of the spine and thorax, a basic understanding of planes of the body and terms of movement is required. As shown in Figure 2.1, the sections of the body can be separated by three planes. The sagittal plane and the frontal, or coronal plane are both parallel to the long axis of the body and divide the body into right and left, and anterior (front) and posterior (back) sections, respectively. The transverse plane lies at a right angle to both the sagittal and frontal plane, dividing the body into superior (upper) and inferior (lower) sections.

Movements of the spine can be described in relation to these planes. As shown in Figure 2.2, flexion and extension are anterior and posterior motions of the trunk in the sagittal plane respectively. Lateral bending is a left or right motion of the upper body in the frontal plane. The third type of motion is axial rotation, a rotation of the spine about the long axis of the body. In normal human motion, several of these motions can be combined, resulting in highly complicated vertebral column kinematics. These planes and terms of motion will be used extensively to describe spinal anatomy, scoliosis, and the finite element model of the scoliotic spine.

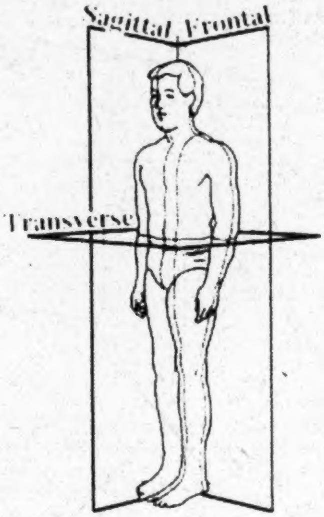

Figure 2.1: Schematic of the sectional planes used to describe anatomical features. Modified from Integrated Publishing[14].

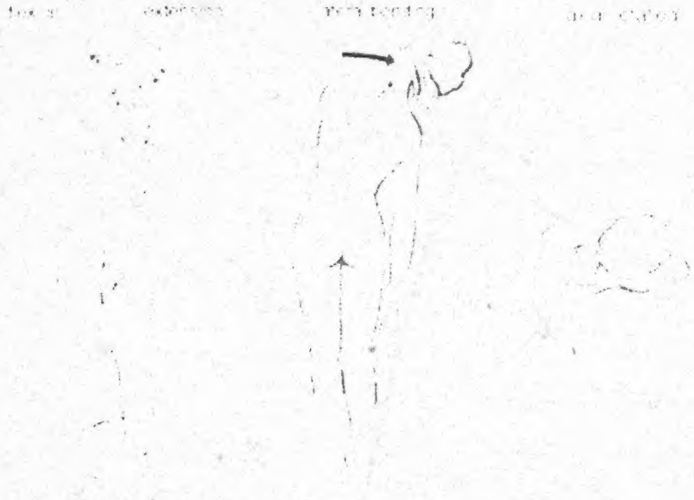

Figure 2.2: Flexion, extension, lateral bending and axial rotation of the spine. Modified from Kapandji[15].

In this chapter, the anatomy of the vertebral column and thoracic cage will be discussed. Please note that muscles are absent from this discussion because while they do play a significant role in stability and function, the anaesthetic routinely used during scoliosis surgery causes muscles to become flaccid. Therefore, all supporting muscles and tendons are neglected in the scoliotic model.

2.1 The Vertebral Column

The human vertebral column, depicted in Figure 2.3, consists of 26 articulating vertebrae which transfer loads from the head and trunk to the pelvis while allowing sufficient motion of the body core. The column also creates a support structure for the spinal cord. There are five distinct regions of the spine: cervical, thoracic, lumbar, sacral and coccygeal. Note that in the sagittal view of the normal spine, four spinal curves exist to allow the weight of the body to be transmitted to the lower limbs. Typically, adolescent idiopathic scoliosis affects only the thoracic and lumbar regions of the spine. Therefore, further discussion will be limited to these regions.

The thoracic spine consists of twelve vertebrae: the most superior is labelled Thoracic 1($T1$) and the most inferior Thoracic 12 ($T12$). Each vertebra in the thoracic region articulates with a pair of ribs, discussed in greater detail later in this chapter.

The lumbar spine consists of five large vertebrae, labeled Lumbar 1 to Lumbar 5 ($L1$-$L5$) from top to bottom. The lumbar vertebrae are typically large as they must support the weight of the head, neck, upper limbs, and trunk of the body.

2.1.1 Vertebra

The typical human vertebra, illustrated in Figure 2.4, can be separated into the vertebral arch and the vertebral body. Both components are composed of a cortical bone shell with a cancellous (or spongy) bone core. Cortical bone is a solid, strong material which is resistant to bending while cancellous bone is lightweight and known to be highly resistive to compressive loading.

The vertebral body is the large anterior portion of the vertebrae which allows the transfer of weight along the vertebral column. The body is attached to an

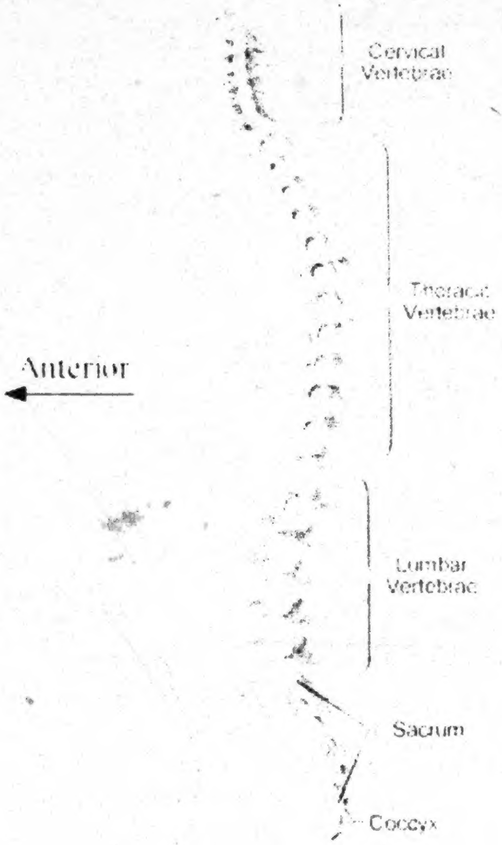

Figure 2.3: Sagittal view of the human vertebral column. Modified from Netter[22]

intervertebral disc on the superior and inferior side.

The spinal cord, located posterior to the vertebral body is enclosed in the canal, known as the vertebral foramen, outlined by the vertebral arch. The arch is composed of pedicles, which attach to the vertebral body and form the base of the vertebral arch and laminae which complete the enclosure of the arch. The vertebral arch also serves to control the range of motion in the spinal column through the spinous, transverse and articular processes. The spinous process projects posteriorly from the laminae while the transverse processes extend laterally off the junction of the laminae and pedicles. The articular processes also arise at the laminae-pedicle junction, extending in both the inferior and superior direction at each side of the vertebrae. At the ends of the articular processes are the articular facets, which articulate with the adjacent vertebral facets to restrict motion of the spine.

Anatomical Differences Between Thoracic and Lumbar Vertebrae

As shown in Figure 2.5, although the features are similar between the lumbar and thoracic vertebrae, several anatomical differences do exist. Of these, the following differences are most pertinent to the present work:

- Lumbar vertebrae are usually wider but shorter than thoracic vertebrae, allowing the lumbar region to carry larger loads.
- Thoracic vertebrae have costal articular facets, the attachment points for the ribs.
- Orientation of the articular facets change between the regions to resist axial rotation in the lumbar spine while resisting extension and lateral bending in the thoracic region.

This last point is further illustrated in Figure 2.6. In the thoracic region, the facets joints lie in a coronal plane that is tilted forward, thus allowing flexion, extension and rotation but restricting lateral bending. However, in the lumbar region the facets are oriented in the sagittal plane, thereby allowing flexion, extension and lateral bending while limiting rotation.

As shown in Figure 2.7, facet orientation can be described in terms of α and β card angles, described by Panjabi[24]. Panjabi recorded these angles from several cadavers to determine if significant differences existed between the vertebrae. His data was modified and is shown in Figure 2.8. Note the trend for α to increase further down the spine and the large discontinuity in β values between the thoracic and lumbar spines. This explains the differences in resistance to axial motion in Figure 2.6.

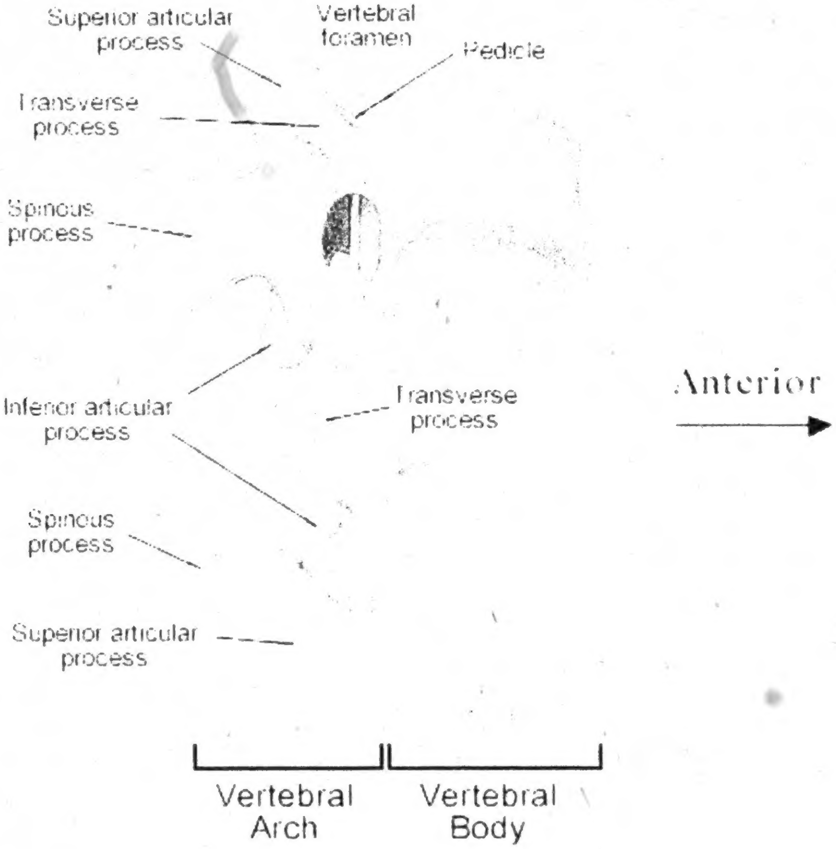
Superior articular process
Vertebral foramen
Pedicle
Transverse process
Spinous process
Inferior articular process
Transverse process
Anterior
Spinous process
Superior articular process
Vertebral Arch
Vertebral Body

Figure 2.4: Lateral view and inferior view of a typical vertebra. Modified from Martini[19].

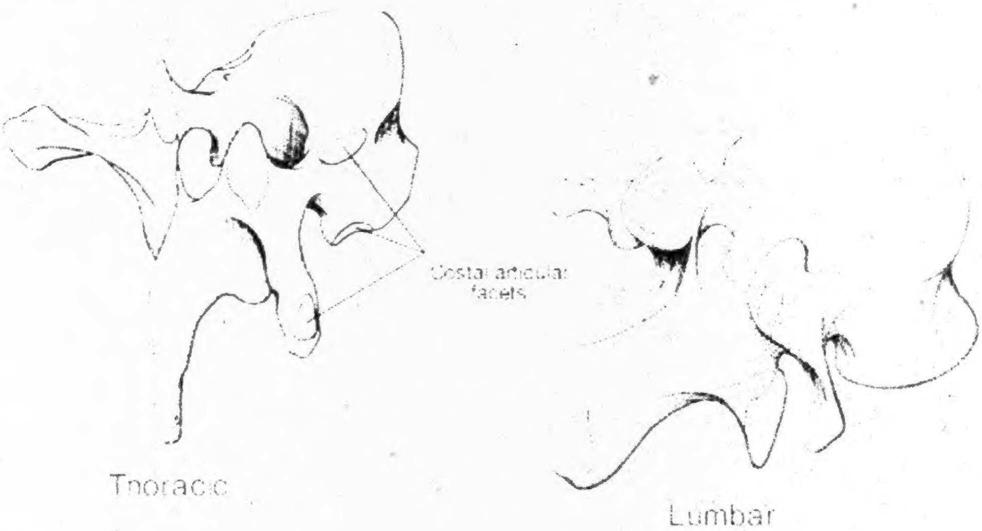
Costal articular facets
Thoracic
Lumbar

Figure 2.5: Posterior oblique view of a typical thoracic and a typical lumbar vertebra. Modified from Kapandiji[15].

Lumbar region

Figure 2.6: The role of the facet joints in the thoracic and lumbar spine when subject to an axial torque. Modified from White & Panjabi[37].

Figure 2.7: Orientation of the facet joints. Card angle measurements are taken by first rotating the card angle from the transverse plane by an amount α followed by an amount β. Modified from Panjabi[24].

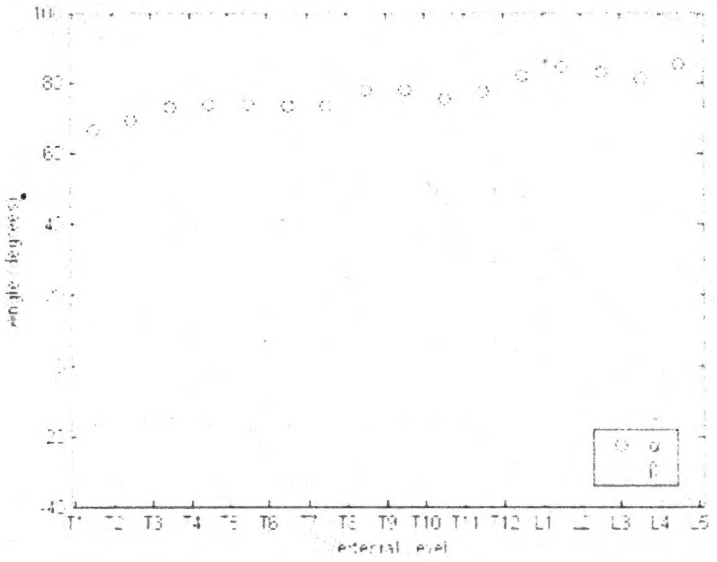

Figure 2.8: Facet orientation of the vertebrae. Modified from Panjabi[24].

2.1.2 Intervertebral Discs

The intervertebral discs, as the name suggests, are located in between adjacent vertebral bodies and account for 20 to 30% of the total height of the vertebral column[37]. The disc is generally found to increase in thickness from the thoracic region to the lumbar region; with averages of 5 mm in the thoracic region and 9 mm in the lumbar region[15].

Each intervertebral disc is composed of three distinct parts: the nucleus pulposes, the annulus fibrosis, and the cartilaginous end-plates. Filling 30 to 50% of the total disc area is the nucleus pulposes. This structure is a high water content body composed of a translucent network of fibrous strands in a gel like substance. Enclosing the nucleus is the annulus fibrosis, made up of concentric laminated bands of annular fibers. As illustrated in Figure 2.9, any two adjacent annular bands are oriented in opposite directions. Separating the disc from the vertebral body are the hyaline cartilage end plates.

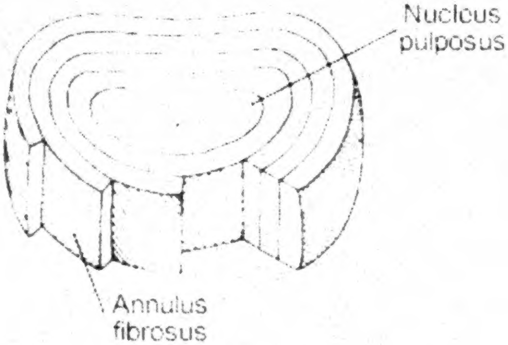

Figure 2.9: Depiction of the intervertebral discs. Cutaway of laminated bands of annular fibers to show that adjacent bands of the fibers are oriented in opposite directions. Modifies from White & Panjabi[37].

Motion of the vertebral bodies about the intervertebral disc is often likened to a swivel[15]. The nucleus pulposes acts as a ball held in between two planes while the surrounding annulus acts in compression or tension depending on the physiological motion. Figure 2.10 depicts the internal forces acting within the disc during compression and tension. The intervertebral disc is often held in compression due to the mass of the torso. In this state the nucleus is flattened and subject to an increase in internal pressure. The resulting widening of the nucleus causes the annulus fibers to bulge and thus be subject to tensile forces. Axial tension within the spinal column can be created through spinal traction. In this state the annulus fibers are placed in tension while the internal pressure of the nucleus is reduced.

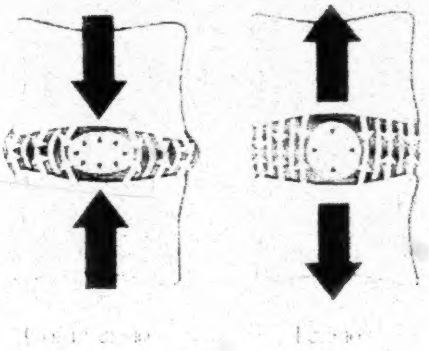

Figure 2.10: Internal forces acting withing the intervertebral disc during compression and tension. Modified from [15].

Extension, flexion, and lateral bending of the spinal column shown in Figure 2.11, cause the nucleus to move away from the side being compressed. This causes the annulus to bulge away from the motion, creating tension in the fibers. The remaining annulus is subject to a compression loading.

During axial rotation of the spine, shown in Figure 2.12, because adjacent annular bands are oriented in opposite directions, only half of the bands act in tension (while the other half will act in tension if the spine is rotated in the other direction). This tension in the annulus increases the pressure of the nucleus in proportion to the angle of rotation.

To protect the spine, intervertebral discs are viscoelastic and nonlinear in nature. Since scoliotic surgery does not impose fast rate loading, the viscoelasticity of the discs can be neglected for the purpose of this model. The nonlinear material properties of the disc have been found to be similar to those of the spinal ligaments.

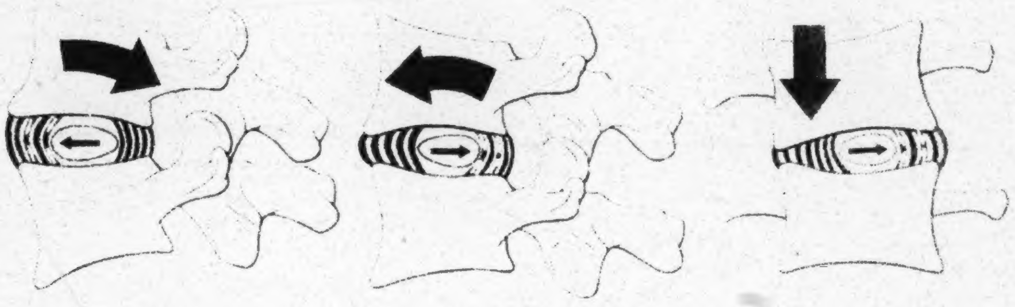

Figure 2.11: Depiction of the movement of the intervertebral disc nucleus during extension, flexion, and lateral bending. Modified from [15].

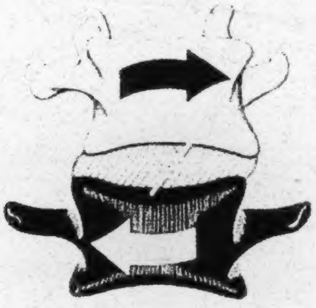

Figure 2.12: Illustration of the forces exerted on the intervertebral disc during axial rotation of the spine. Modified from [15].

2.1.3 Ligaments

Spinal ligaments are important as they allow motion between vertebrae, protect the spinal cord by restricting motion, and provide stability to the spine. As shown in Figure 2.13, there are seven ligaments connecting adjacent vertebrae; the anterior and posterior longitudinal ligament, the intertransverse ligaments, the facet capsular ligaments, the interspinous ligaments and the supraspinous ligament.

The anterior longitudinal ligament runs the length of the vertebral column and is attached firmly to the vertebral bodies but not as firmly to the intervertebral discs. The width is generally narrower in the thoracic region where the ligament is also often thicker. The anterior longitudinal ligament primarily resists extension, but also resists lateral bending.

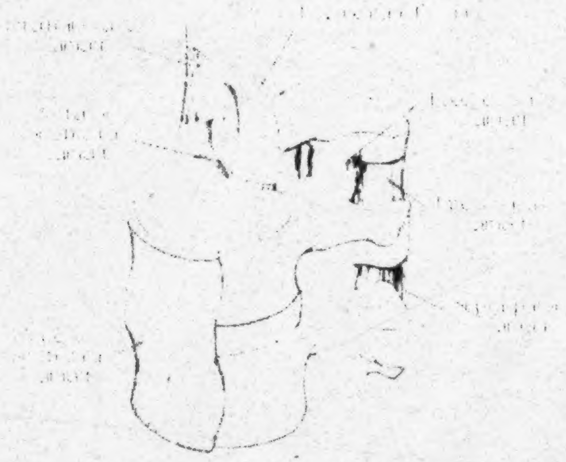

Figure 2.13: Ligaments of the Vertebral Column. Modified from White and Panjabi[37].

The posterior longitudinal ligament parallels the anterior longitudinal ligament but does not attach to the surface of the vertebral body, inserting only at the superior and inferior edges. This ligament has been shown to limit flexion, bending and to slightly affect axial rotation of the spine.

The intertransverse ligaments connect transverse processes of adjacent vertebrae. As such, they are responsible for additional stiffness against lateral bending and extension. The effects of this ligament are negligible in the lumbar region because of their negligible cross-sectional size [37].

The capsular ligaments join adjacent superior and inferior articular process surfaces, providing additional support to the articular facets. As such, their function in the spine is dependent on the orientation of these facets discussed previously. These ligaments also allow gliding movements to occur between facet surfaces.

The ligamentum flavum is a highly elastic ligament connecting the laminae of adjacent vertebrae. It is important in protecting the spine and spinal cord against hyperflexion.

The interspinous and supraspinous ligaments connect adjacent spinous processes together and are also imperative in preventing hyperflexion of the spine.

Ligaments behave like cable structures in that they resist tensile forces but buckle when subjected to compression loads and are therefore unable to provide stiffness in compression. As shown in Figure 2.14, ligaments act in a nonlinear fashion when subjected to tensile forces. This property allows small strains, but the ligament stiffens with increasing strain, thereby protecting the spinal column.

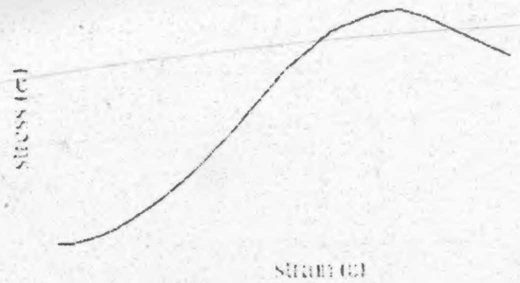

Figure 2.14: Stress-strain curve of a typical ligament in tension. Modified from Myklebust[21].

2.2 Thoracic Cage

The thoracic cage, shown in Figure 2.15, articulates with the thoracic region of the spine and serves to protect vital organs of the body while stiffening the spine. Each thoracic vertebra articulates with a similarly named rib pair. For example, Rib Pair 1 articulates with $T1$. Note that ribs 1 through 7 are true ribs, meaning that they are attached directly to the sternum by means of individual costal cartilage. Ribs 8 through 10 are termed false ribs because they attach to the sternum via fused costal cartilage while the remaining two rib pairs are floating ribs as they do not attach directly to the sternum.

Sternum
7
True ribs
Costal cartilages
11
False ribs
12
Floating ribs

Figure 2.15: Components of the thoracic cage. Modified from Netter[22].

Rib articulation with the vertebral column is depicted in Figure 2.16. As shown the ribs articulate both with the transverse process, termed the costo-transverse joint, and the vertebral body, the costo-vertebral joint

Several ligaments control the articulations at the costo-vertebral and costo-transverse joints as shown in Figure 2.17. The costo-vertebral joint is limited to small gliding motions due to the radiate ligament and as such significantly increases the stiffness of the spine. The costo-transverse joint is somewhat weaker, but is strengthened by three ligaments: the superior costo-transverse ligament, the lateral costo-transverse ligament, and the inferior costo-transverse ligament. This joint permits a larger amount of motion than the costo-vertebral joint.

Figure 2.16: Superior view of the costovertebral articulation. Modified from Kapandji[15].

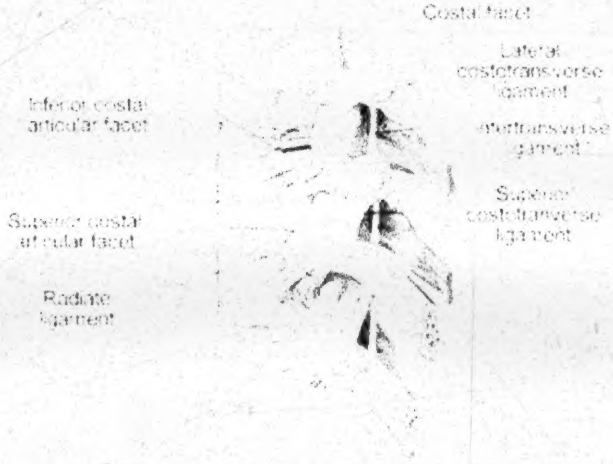
Costal facet
Lateral costotransverse ligament
Inferior costal articular facet
Intertransverse ligament
Superior costal articular facet
Superior costotransverse ligament
Radiate ligament

Figure 2.17: Left lateral view of the costovertebral joint. Modified from Netter[22].

2.3 Material Properties

Due to the large variability in mechanical testing and the viscoelastic properties of tissue, material properties of the vertebrae and intervertebral discs found in the literature are often widely scattered. Ultimately, mechanical personalization should be performed to obtain material properties specific to each patient. Research is currently underway to determine the feasibility and accuracy of obtaining this information. Currently, the values shown in Table 2.1, obtained from Skalli[29], are widely used and will therefore be used for the purpose of this project. However, the ability to change these values will be built into the model.

Table 2.1: Material Properties of the Vertebral Column and Thoracic Cage

Part	**Young's Modulus (N/mm2)**	**Poissons' Ratio**
Cortical Bone	12000	0.3
Cancellous Bone	100	0.3
Intervertebral Disc	2	0.41
Spinal Ligaments	10	0.3

This basic anatomy and biomechanical description of the normal human spine and thorax will aid in the understanding the scoliotic deformity, discussed in the following chapter.

Chapter 3

Adolescent Idiopathic Scoliosis

This chapter provides a general description of scoliosis, focussing on Adolescent Idiopathic Scoliosis (AIS), in addition to treatments used to prevent further progression.

3.1 Characteristics

Scoliosis, depicted in Figure 3.1, is defined as a complex three-dimensional deformity of the torso, characterized by a lateral deviation and axial rotation of the spine, accompanied by ribcage deformity. There are several known causes of scoliosis, from neuromuscular disorders to congenital defects during formation of the spine. However, approximately 80% of scoliosis cases are idiopathic, meaning they have no identifiable cause. Idiopathic scoliosis can be further categorized depending on the age of presentation: infancy, childhood, and adolescence. The latter, adolescent idiopathic scoliosis is recognized as the most prevalent form and the focus for this study.

3.1.1 Lateral Deviation

The lateral deviation of the spine can be described through several techniques and measurements. King et al.[17] presented a classification system for lateral spinal curve patterns used primarily to select an appropriate surgical method. This classification system is depicted in Figure 3.2. Type I and II are defined as s-shaped curves dominant in the lumbar and thoracic regions respectively. Type III is a single thoro-

Figure 3.1: Depiction of a scoliotic curve. Modified from Keim[16].

columbar curve while Type IV is a long thoracic curve. Type V can be defined as a double thoracic curve. Note that other classification systems have been proposed, however, the King classification is still the most widely used today.

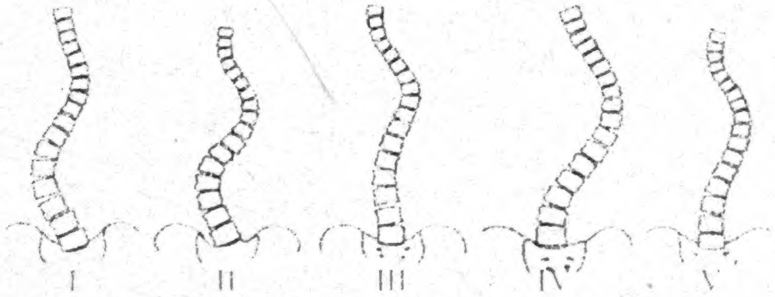

Figure 3.2: King Classification of scoliotic curves. Modified from King et al.[17].

Several parameters, depicted in Figure 3.3, can be used to describe the severity of the lateral deformity of scoliosis curvatures. Cobb Angles are measured by first identifying the end vertebrae of the curve then lines are drawn parallel to the end vertebrae and the angle between them is measured[7]. For a double curve, the curvature of the upper curve is denoted Cobb Angle α while the lower curve is labelled Cobb Angle β. Decompensation is the lateral shift of the spine between $T1$ and the sacrum. An obliquity may also exist at the base of $L5$, termed the "Lumbar Obliquity".

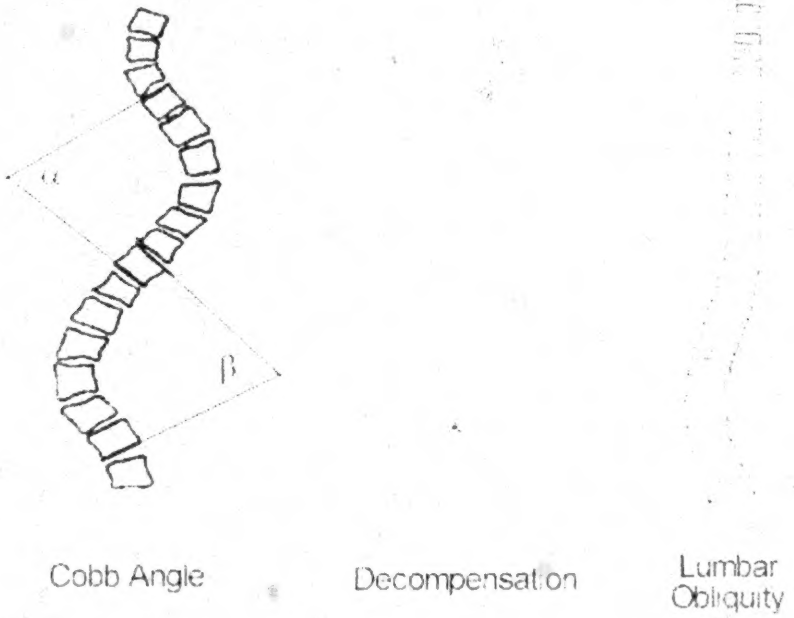

Figure 3.3: Measurement of the Scoliotic curve. Modified from Pope et al.([28]), Keim[16], White & Panjabi[37].

The lateral curvature of the scoliotic spine is a result of both vertebral and intervertebral disc wedging shown in Figure 3.4. When vertebral deformation is present, the curve is termed structural scoliosis, whereas when only disc wedging is the involved, the curve is termed a functional or compensatory curve. Figure 3.5 depicts the lateral bending test which is typically performed to differentiate between structural and functional curves. Since the deformation of a functional curve is due to disc wedging only, as the patient bends in the direction opposite to the curve, the curve will correct. However, a structural curve will not correct completely during the lateral bending test. Shown here is a typical double curve with a structural thoracic curve and a functional lumbar curve. The functional curve typically arises secondarily to align the torso laterally with the pelvis, decreasing decompensation. In a study performed to further define structural curves, Stokes et al. [31] found that the mean wedging angle of the apical vertebra was 17% of the measured Cobb angle while the average vertebral wedging of the ±1 and ±2 positioned vertebrae was 12% and 5% of the Cobb angle respectively.

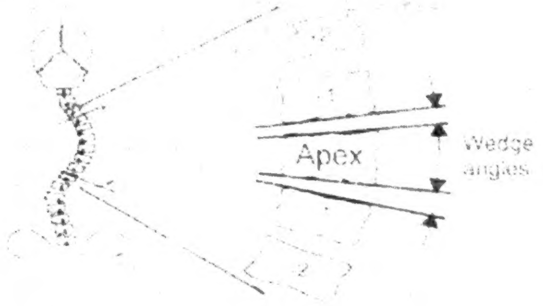

Figure 3.4: Vertebral and intervertebral disc wedge angles. Modified from Stokes et al. [31].

3.1.2 Axial Rotation

In the sagittal plane of a scoliosis patient, one will generally observe a flattening of the back due to the axial rotation of the vertebrae which causes the normal curves of the back to rotate into the frontal plane. As shown in Figure 3.6, axial rotation can be measured by the location of the spinous process in relation to the vertebral body from a posterior x-ray. The amount of rotation of the curve can be graded at the apical vertebra using a zero to IV rating described by Nash and Moe[7] where zero is symmetric and grade IV is when the pedicle is past the center of the vertebral body. Similar to wedging in the lateral plane, the vertebra can also deform axially as shown in Figure 3.7.

Standing
Left Bending
Right Bending

Figure 3.5: Lateral bending tests performed to differentiate between structural curves and functional curves. As shown here, the lumbar curve is functional while the thoracic curve is structural. Modified from Keim[16].

Figure 3.6: Axial rotation of the scoliotic spine. Modified from White et al.[37].

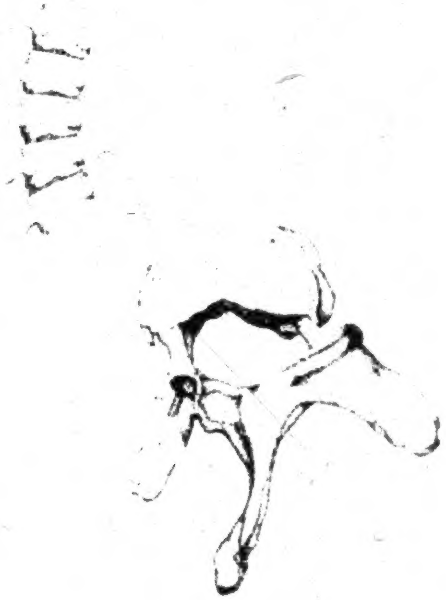

Figure 3.7: Axial deformation of the vertebrae typical in scoliosis patients. Modified from White et al.[37].

Figure 3.8: Typical deformation of the thoracic cage in scoliosis patients. Modified from Keim[16].

3.1.3 Ribcage Deformity

In conjunction with the three-dimensional deformity of the vertebral column, the ribcage will often deform as depicted in Figure 3.8. This deformation is often described as a rib hump most noticeable from a posterior view during flexion of the spine.

3.2 Treatment

Treatment of scoliosis is dependent on many factors including the physical maturity of the patient and the severity of the curve. Note that scoliosis will typically only progress rapidly during growth phases. Standard treatments involve observation, bracing or surgical fusion. Note that there are alternative techniques such as electrical stimulation, exercise, and manipulation which currently have not been proven to alter the progression of adolescent idiopathic scoliosis.

3.2.1 Observation

Typically in patients with a curve with a Cobb Angle less than 20° the curve is simply observed over set intervals. In most cases the curve will not progress further.

3.2.2 Bracing

Should the curve progress to 20°, a specialized brace is constructed to apply pressure to specific regions of the ribcage to prevent further progression of the curve. The patient will typically be instructed to wear the brace for approximately 22 hours a day and will also be given a set of exercises to perform. Again, the curve is monitored for progression over set intervals. The effectiveness of bracing is often compromised due to patients not wearing the brace for the specified amount of time and/or not wearing the brace at the prescribed tightness. Research is currently being performed to monitor the correlation between brace effectiveness and patient compliance.

3.2.3 Surgery

If the curve reaches 45° and the patient is still growing, surgical fusion is prescribed to prevent further deformity which may compromise respiratory or cardiopulmonary systems. Surgical methods vary between surgeons and individual patients, however, a typical surgery follows these steps:

- The patient is placed face down (prone) on the operating table and anesthetized.
- An incision is made down centre of patient's back and the muscles posteriorly attached to the vertebra are removed.
- Hooks and screws, depicted in Figures 3.9 and 3.10, are placed at predefined locations on the spine. These locations are dependent not only on the scoliotic deformation, but on the surgeon performing the procedure. A sample placement is illustrated in Figure 3.11.

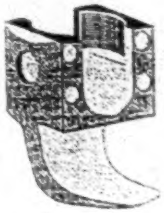

Figure 3.9: Sample hook typically used for scoliosis surgery. Modified from Zeller and Dubousset[39].

- The correcting and fixation rods are shaped by the surgeon.
- The correcting rod is placed on the concave side of the curve and is inserted at either end of the instrumentation, wherever it fits best.
- Each hook and screw is attached separately to the rod. Note that each surgeon has a preferred sequence and that sequence also depends on type of scoliotic curve and length of instrumentation.

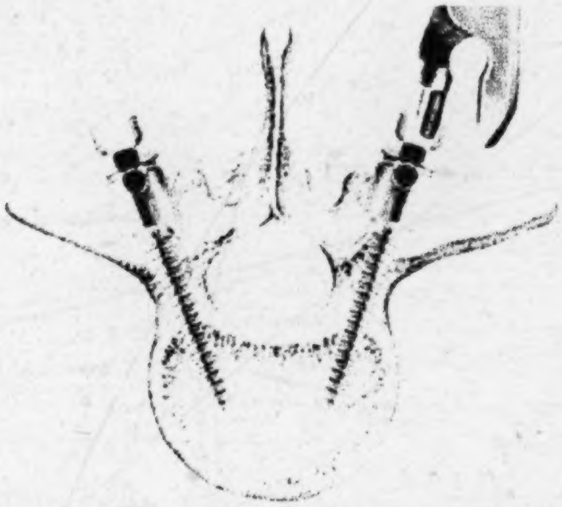

Figure 3.10: Superior view of the insertion of pedicles screws into a vertebra. Modified from Spine-Health[30].

- The rod is then rotated to move the spinal curvature into the sagittal plane. In some cases, the spinal curve is corrected by translation instead of rotation. Again, this depends on the scoliotic curve and the surgeon's discretion.
- The fixation rod is placed on the convex side of the curve and hooks and screws are attached sequentially.
- Decortication, or removal of exterior surface of vertebrae, and grafting are performed to fuse the spine.

Currently, force data is being obtained in surgery through the use of instrumented screws and hooks. Forces in all three anatomical planes can be obtained, however, individual screws can only obtain data in two directions. In addition, forces are obtained from the rod rotation device during the rotation of the spine. Displacement measurements are also taken using active markers in surgery. Ultimately, a presurgical tool could be validated using the force and displacement data from previous surgeries.

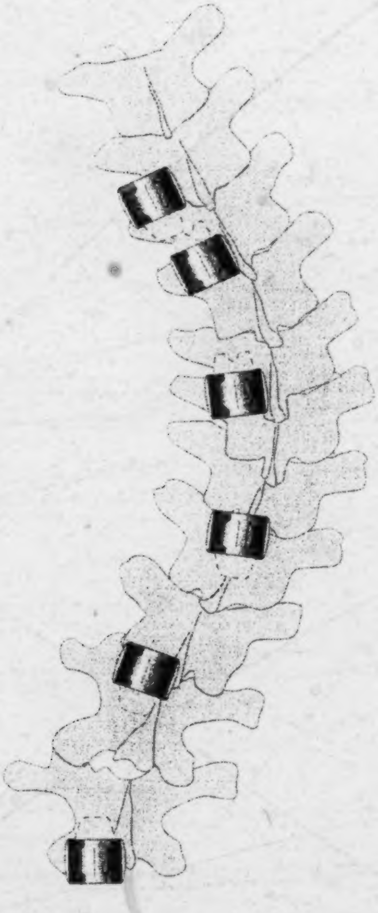

Figure 3.11: Posterior View of sample instrument placement for a scoliotic curve. Note that only hooks are used in this example. Modified from Zeller and Dubousset[39].

Chapter 4

Finite Element Analysis

This chapter will review the basics of the finite element method before explaining some advanced techniques required to create the real-time simulation of scoliosis surgery.

4.1 Overview of the Finite Element Method

The basic finite element method can be summarized as shown in Figure 4.1. First the problem data is input into the model. This can be done either by Direct Generation, where the user manually defines the coordinates for each node and the connectivity between them, or Solid Modeling, whereby the user specifies the geometric boundaries of the solids then a mesh is automatically generated to create the nodes and elements. The element stiffness matrix, $[k_e]$ is then formed for each element. The global stiffness matrix, $[k_G]$ is assembled using the individual element stiffness matrices. Loads and constraints are applied to the mathematical model by creating the force matrix, $\{f\}$ and modifying the global stiffness matrix respectively. Displacements, $\{q\}$ can then be solved for. Further postprocessing can be performed to obtain other results such as internal forces $\{f_e\}$, stresses and strains.

4.2 Derivation of the Finite Element Equations

In finite element analysis, it is assumed that a system will always deform to a configuration where the total system energy is a minimum. The total potential energy, Π,

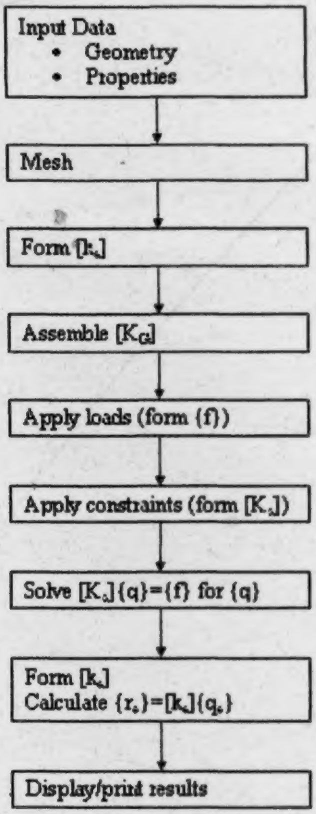
Input Data
• Geometry
• Properties
Mesh
Form [k_e]
Assemble [K_G]
Apply loads (form {f})
Apply constraints (form [K_s])
Solve [K_s]{q}={f} for {q}
Form [k_e]
Calculate {r_e}=[k_e]{q_e}
Display/print results

Figure 4.1: Flowchart of the basic steps involved in finite element analysis. Modified from Fyfe[11].

is comprised of the strain energy or internal work stored in the material, U, and the potential energy due to the applied loads, Ω where

$$\Pi = U + \Omega \tag{4.1}$$

For a linear elastic system, the strain energy can be written as:

$$U = \frac{1}{2}\{q\}^T [K_G] \{q\} \tag{4.2}$$

while the potential energy can be calculated from

$$\Omega = -\{q\}^T \{f\} \tag{4.3}$$

Therefore, the total potential energy in the system can be written as:

$$\Pi = \frac{1}{2}\{q\}^T[K_G]\{q\} - \{q\}^T\{f\} \tag{4.4}$$

As previously stated, the system is assumed to deform to a configuration where the total potential energy is a minimum. Therefore,

$$\begin{aligned} \frac{d\Pi}{dq} &= [K_G]\{q\} - \{f\} = 0 \\ \Longrightarrow & \quad [K_G]\{q\} = \{f\} \end{aligned} \tag{4.5}$$

4.3 Element Derivations

Four different element types will be used to create the two-dimensional model of the scoliotic spine; the elastic truss element, the nonlinear strain truss element, the Triangular Element and the Quadrilateral Element. The selection of these particular elements to model the spine will be described in detail in Chapter 6. Energy methods are used to outline the stiffness matrix derivations for these elements.

4.3.1 Elastic Truss Element

Assuming small deformations, the element stiffness matrix for the two-dimensional truss element shown in Figure 4.2 can be written[11]:

$$k = [R]^T\frac{AE}{\ell}\begin{bmatrix} 1 & -1 \\ -1 & 1 \end{bmatrix}[R] \tag{4.6}$$

where $[R]$ is the transformation matrix,

$$[R] = \begin{bmatrix} \cos\theta & \sin\theta & 0 & 0 \\ 0 & 0 & \cos\theta & \sin\theta \end{bmatrix} \tag{4.7}$$

4.3.2 Nonlinear Strain Truss Element

To account for large deflections, the nonlinear strain-displacement equation for a truss should be used:

$$\varepsilon_{xx} = \frac{\partial u}{\partial x} + \frac{1}{2}\left(\frac{\partial u}{\partial x}\right)^2 \tag{4.8}$$

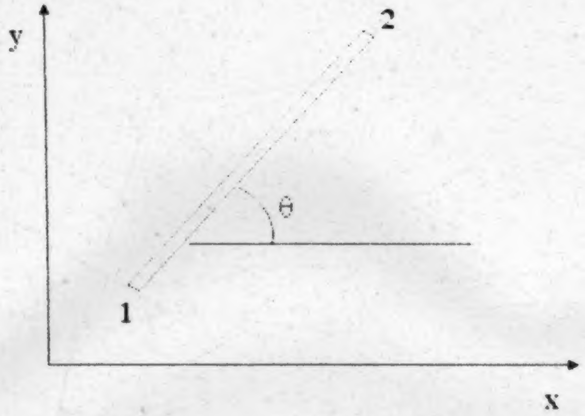

Figure 4.2: Illustration of a two-dimensional truss element.

The resulting stiffness matrix is [10]:

$$k = [R]^T \left[\frac{AE}{\ell} \begin{bmatrix} 1 & -1 \\ -1 & 1 \end{bmatrix} + \frac{2AE}{\ell^2} u_{21} \begin{bmatrix} 1 & -1 \\ -1 & 1 \end{bmatrix} + \frac{3AE}{2\ell^3} u_{21}^2 \begin{bmatrix} 1 & -1 \\ -1 & 1 \end{bmatrix} \right] [R] \tag{4.9}$$

where u_{21} is a shorthand notation for the element deflection, $u_2 - u_1$. A full derivation of the stiffness matrix is shown in Appendix A.

4.3.3 Triangular Element

Consider a triangular plane stress element with thickness t as shown in Figure 4.3. The element stiffness matrix, k, can be shown to be:

$$k = t\,[H]^T\,[G]^T\,[D]\,[G]\,[H]\,A \tag{4.10}$$

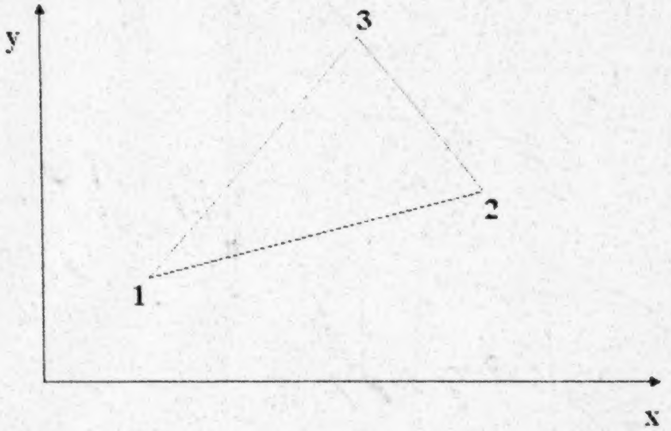

Figure 4.3: Illustration of a typical two-dimensional triangular element.

where:

$$[H] = \underbrace{\begin{bmatrix} 1 & x_1 & y_1 & 0 & 0 & 0 \\ 0 & 0 & 0 & 1 & x_1 & y_1 \\ 1 & x_2 & y_2 & 0 & 0 & 0 \\ 0 & 0 & 0 & 1 & x_2 & y_2 \\ 1 & x_3 & y_3 & 0 & 0 & 0 \\ 0 & 0 & 0 & 1 & x_3 & y_3 \end{bmatrix}}_{\textbf{the element coordinates}}$$

$$[G] = \underbrace{\begin{bmatrix} 0 & 1 & 0 & 0 & 0 & 0 \\ 0 & 0 & 0 & 0 & 0 & 1 \\ 0 & 0 & 1 & 0 & 1 & 0 \end{bmatrix}}_{\textbf{derivative of the displacement functions}}$$

$$[D] = \underbrace{\frac{E}{1-v^2}\begin{bmatrix} 1 & v & 0 \\ v & 1 & 0 \\ 0 & 0 & \frac{1-v}{2} \end{bmatrix}}_{\textbf{the elasticity matrix}}$$

and A is the area of the triangle[11].

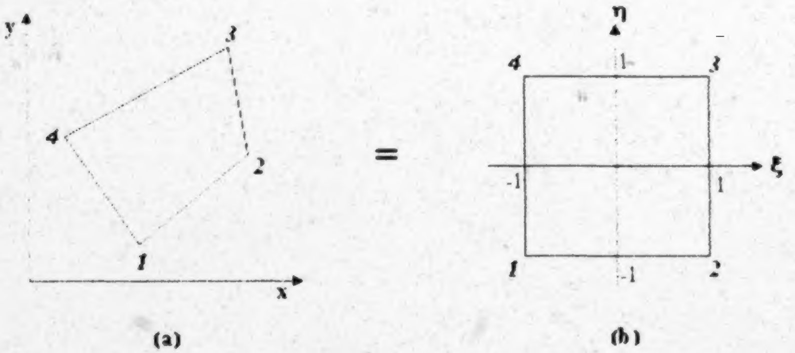

Figure 4.4: Transformation of a two-dimensional isoparametric element from the x-y plane into a unit element in the η-ξ plane.

4.3.4 Quadrilateral Element

Using isoparametric elements, the coordinates of a quadrilateral element in the x-y plane are transformed into a unit element in the η-ξ plane as shown in Figure 4.4. The derivation for this element, found in Chandrupatla[8], yields the following stiffness matrix:

$$k = t \int_{-1}^{1} \int_{-1}^{1} A\,[G]^T\,[D]\,[G]\,A \det(J)\, d\xi d\eta \tag{4.11}$$

4.4 Matrix Storage

In most finite element problems, the global stiffness matrix is sparsely populated, meaning that it contains a large number of zero-valued members. An illustration of such a matrix could appear as shown in Figure 4.5. For small finite element problems, full matrix storage is suitable. However, with large problems, the computational time and storage requirements can become onerous. By storing only the required matrix members, one can substantially decrease the required computational memory. In addition, one can reduce computational time by eliminating operations on zero members. Two methods that deal with this are sparse storage and banded storage. Using sparse matrix storage, only the non-zero values and their indices are stored.

Specialized solvers within Matlab® have been created to effectively manipulate sparse matrices. Banded storage can be used with matrices where all members outside of a band centered on the diagonal are nonzero. Since the efficiency of banded solvers decreases as the band width increases, it is preferred to create a narrow bandwidth. To minimize the bandwidth, it is necessary to keep the difference in node numbers of each element as small as possible. Due to the nature of this problem, specifically the modeling of the sternum, a tight bandwidth structure is not possible. Therefore, sparse matrix storage was selected.

Using the built in sparse matrix storage in Matlab®, a sparse matrix will require less computational memory as long as the density of the matrix is less than two-thirds[18]. However, one should also consider that operations on sparse matrices require more execution time per element compared to full matrices. The efficiency of the Matlab® sparse matrix capabilities will be tested for the current application.

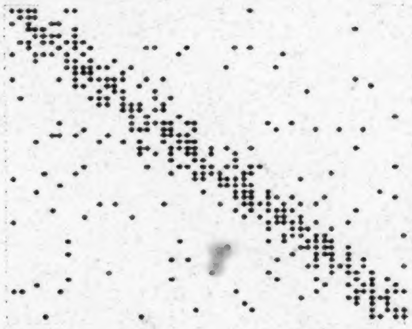

Figure 4.5: Representation of a typical global stiffness matrix. The markers represent the non-zero members.

4.5 Condensation

Condensation is a procedure that decreases the number of degrees of freedom (DOFs) in a system without compromising accuracy. An illustration of this is shown in Figure 4.6. This method is beneficial because reducing the number of DOFs decreases computational time. However, immediate access to the results from the eliminated degrees of freedom is not available.

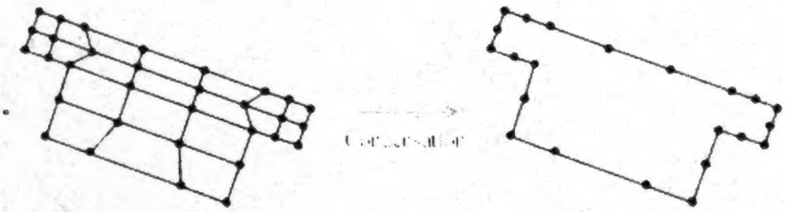

Figure 4.6: Illustraion of condensation, a procedure used to decrease the number of degrees of freedom in a system without compromising accuracy.

To perform condensation, the stiffness matrix must be manipulated to account for the new "super-element". The required modification is shown in the derivation below, modified from Fyfe [11].

Beginning with Equation 4.5, the matrices are rearranged as shown below.

$$\begin{bmatrix} [k_{rr}] & [k_{rc}] \\ [k_{cr}] & [k_{cc}] \end{bmatrix} \left\{ \begin{array}{c} \{q_r\} \\ \{q_c\} \end{array} \right\} = \left\{ \begin{array}{c} \{f_r\} \\ \{f_c\} \end{array} \right\} \tag{4.12}$$

where: $r =$ the DOF to be retained

$c =$ the DOF that are condensed out

Expanding out the sub-matrices,

$$[k_{rr}]\{q_r\} + [k_{rc}]\{q_c\} = \{f_r\} \tag{4.13}$$

$$[k_{cr}]\{q_r\} + [k_{cc}]\{q_c\} = \{f_c\} \tag{4.14}$$

Solving 4.14 for q_c,

$$q_c = [k_{cc}]^{-1}\{f_c\} - [k_{cc}]^{-1}[k_{cr}]\{q_r\} \tag{4.15}$$

then substituting back into 4.13 results in:

$$\underbrace{\left([k_{rr}] - [k_{rc}][k_{cc}]^{-1}[k_{cr}]\right)}_{[k^*]}\{q_r\} = \underbrace{\{f_r\} - [k_{rc}][k_{cc}]^{-1}\{f_c\}}_{\{f^*\}} \tag{4.16}$$

For our case, the nodes being eliminated will not have any loads applied to them, therefore

$$[k^*]\{q_r\} = \{f_r\}$$

$$\text{where: } [k^*] = [k_{rr}] - [k_{rc}]\,[k_{ee}]^{-1}\,[k_{cr}] \tag{4.17}$$

While this operation is time consuming, it will be evident from later sections that this method is good for nonlinear problems where the matrices do not need to be updated after every load step. Such is the case for the elements representing the vertebral bodies.

4.6 Constraint Application

There are many different ways to apply constraints in Finite Element Analysis. As each method has different strengths and weaknesses, three different methods will be employed in this model. Note that only rigid constraints will be addressed in this section as there is no use for prescribed boundary conditions in the model. For each of the methods, the following set of equations will be constrained:

$$\begin{bmatrix} k_{11} & k_{12} & k_{13} & k_{14} \\ k_{21} & k_{22} & k_{23} & k_{24} \\ k_{31} & k_{32} & k_{33} & k_{34} \\ k_{41} & k_{42} & k_{43} & k_{44} \end{bmatrix} \begin{Bmatrix} q_1 \\ q_2 \\ q_3 \\ q_4 \end{Bmatrix} = \begin{Bmatrix} P_1 \\ P_2 \\ P_3 \\ P_4 \end{Bmatrix} \tag{4.18}$$

4.6.1 Allaire's Method

Allaire's method to apply rigid constraints to the finite element model is fast and easy to program, with little need for additional bookkeeping[11]. To constrain q_3, simply make the equivalent row and column terms equal to zero except the diagonal term as shown below:

$$\begin{bmatrix} k_{11} & k_{12} & 0 & k_{14} \\ k_{21} & k_{22} & 0 & k_{24} \\ 0 & 0 & k_{33} & 0 \\ k_{41} & k_{42} & 0 & k_{44} \end{bmatrix} \begin{Bmatrix} q_1 \\ q_2 \\ q_3 \\ q_4 \end{Bmatrix} = \begin{Bmatrix} P_1 \\ P_2 \\ 0 \\ P_4 \end{Bmatrix} \tag{4.19}$$

4.6.2 Elimination Method

The elimination method simply involves removing the equivalent rows and columns as shown in the equations below. While more bookkeeping is required to keep track of the deleted degrees of freedom, the time savings may be worthwhile.

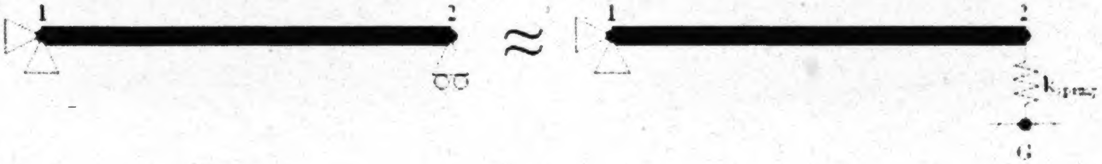

Figure 4.7: Depiction of the penalty approach applied to a beam element.

$$\begin{bmatrix} k_{11} & k_{12} & k_{14} \\ k_{21} & k_{22} & k_{24} \\ k_{41} & k_{42} & k_{44} \end{bmatrix} \begin{Bmatrix} q_1 \\ q_2 \\ q_4 \end{Bmatrix} = \begin{Bmatrix} P_1 \\ P_2 \\ P_4 \end{Bmatrix} \tag{4.20}$$

The elimination method and Allaire's method will be tested to determine which approach requires less computational time and memory. The selected method will then be used to apply all single degree of freedom constraints.

4.6.3 Penalty Approach

The penalty approach is an approximate method of applying boundary conditions to the model[8]. It is best explained using the example of a beam shown in Figure 4.7. Using Allaire's method, we would simply zero out the fourth column and row of the stiffness matrix and force vector. Instead, think of the roller support as a one dimensional spring. The modified total potential energy expression becomes:

$$\Pi = \frac{1}{2}\{q\}^T [k_e] \{q\} + \frac{1}{2} k_s {q_4}^2 - \{q\}^T \{f\} \tag{4.21}$$

The resulting set of equations are therefore:

$$\begin{bmatrix} k_{11} & k_{12} & k_{13} & k_{14} \\ k_{21} & k_{22} & k_{23} & k_{24} \\ k_{31} & k_{32} & k_{33} & k_{34} \\ k_{41} & k_{42} & k_{43} & k_{44} + k_s \end{bmatrix} \begin{Bmatrix} q_1 \\ q_2 \\ q_3 \\ q_4 \end{Bmatrix} = \begin{Bmatrix} P_1 \\ P_2 \\ P_3 \\ P_4 \end{Bmatrix} \tag{4.22}$$

Obviously the choice of k_s will affect the accuracy results If k_s is too small, the model will no longer approximate the original problem and if k_s is too large we may obtain an ill conditioned matrix. As shown by Chandrupatla[8] the following equation can serve as a guideline:

$$k_s = \max|K_{ij}| * 10^4 \text{ for } 1 \leqslant i \leqslant N,\ 1 \leqslant j \leqslant N \tag{4.23}$$

While this method will not be used by itself (since the elimination method is much quicker and easier to program), it is the basis for constraint equations.

4.6.4 Constraint Equations

Sometimes it is necessary to constrain one degree of freedom relative to another. An example of this would be modeling the deflection for an inclined roller as shown in Figure 4.8. In this example the deflection in the y direction would be dependent on the deflection in the x direction. A modified penalty method is necessary in situations such as these to avoid an iterative solution.

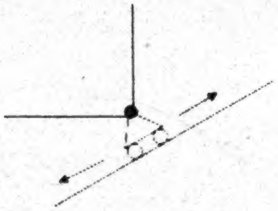

Figure 4.8: Illustration of an angled roller constraint. A constraint equation can be used to constrain the x and y deflection.

Consider the following boundary condition:

$$\beta_1 q_1 + \beta_2 q_2 = \beta_0 \tag{4.24}$$

where $\beta_0, \beta_1, \beta_2$ are constants.

Now, consider the modified total potential energy expression:

$$\Pi = \frac{1}{2}\{q\}^T[k_e]\{q\} + \frac{1}{2}k_s(\beta_1 q_1 + \beta_2 q_2 - \beta_0)^2 - \{q\}^T\{f\} \tag{4.25}$$

This translates into:

$$\begin{bmatrix} k_{11}+k_s\beta_1^2 & k_{12}+k_s\beta_1\beta_2 & k_{13} & k_{14} \\ k_{21}+k_s\beta_2\beta_1 & k_{22}+k_s\beta_2^2 & k_{23} & k_{24} \\ k_{31} & k_{32} & k_{33} & k_{34} \\ k_{41} & k_{42} & k_{43} & k_{44} \end{bmatrix} \begin{Bmatrix} q_1 \\ q_2 \\ q_3 \\ q_4 \end{Bmatrix} = \begin{Bmatrix} P_1 + k_s\beta_0\beta_1 \\ P_2 + k_s\beta_0\beta_2 \\ P_3 \\ P_4 \end{Bmatrix} \tag{4.26}$$

For an inclined roller connection, we can say that $\beta_1 q_1 - \beta_2 q_2 = 0$ where β_1 and β_2 are dependant on the angle of the incline. For example, at a 45° angle, $\beta_1 = \beta_2$. One could also relate two degrees of freedom from different nodes, a method that is useful in modeling the sternum.

Sometimes, a relation exists between more than two degrees of freedom. The above equations can simply be expanded. For example, consider the relation:

$$\beta_1 q_1 + \beta_2 q_2 = \beta_3 q_3 + \beta_4 q_4 \tag{4.27}$$

This translates into:

$$\begin{bmatrix} k_{11}+k_s\beta_1^2 & k_{12}+k_s\beta_1\beta_2 & k_{13}-k_s\beta_1\beta_3 & k_{14}-k_s\beta_1\beta_4 \\ k_{21}+k_s\beta_2\beta_1 & k_{22}+k_s\beta_2^2 & k_{23}-k_s\beta_3\beta_3 & k_{24}-k_s\beta_2\beta_4 \\ k_{31}+k_s\beta_3\beta_1 & k_{32}+k_s\beta_3\beta_2 & k_{33}+k_s\beta_3^2 & k_{34}-k_s\beta_2\beta_4 \\ k_{41}+k_s\beta_4\beta_1 & k_{42}+k_s\beta_4\beta_2 & k_{43}-k_s\beta_4\beta_3 & k_{44}+k_s\beta_4^2 \end{bmatrix} \begin{Bmatrix} q_1 \\ q_2 \\ q_3 \\ q_4 \end{Bmatrix} = \begin{Bmatrix} P_1 \\ P_2 \\ P_3 \\ P_4 \end{Bmatrix} \tag{4.28}$$

This type of constraint equation becomes necessary for modeling contact between a point and a surface where the surface is inclined. For example, assume the surface is inclined by θ and that q_1 and q_2 are the x and y degrees of freedom respectively for the point, and q_3 and q_4 are the x and y degrees of freedom respectively for a node on the surface. The equation would then be written:

$$-q_1\sin\theta + q_2\cos\theta = -q_3\sin\theta + q_4\cos\theta \tag{4.29}$$

As with the penalty approach, an appropriate value of k_s must be used to obtain accurate results and avoid an ill-conditioned matrix.

4.7 Nonlinearities

Nonlinearities arise in structural problems when the stiffness matrix and/or the force vector become dependent on the displacement. As such, the load must be applied incrementally and the stiffness matrix and/or the force vector updated before the load is incremented. Examples of structural nonlinearities can typically be classified into material nonlinearities, geometric nonlinearities, and contact problems. These classes will be described in more detail in the section that follows. Implementing nonlinear code into FEA is very straight forward and follows the same general procedure regardless of the class of nonlinearity present. The following procedure is a modification of that found in Bathe[3].

The load is first broken up and applied incrementally, with each increment defined as a time step. Note that since we are dealing with a static analysis, time is only used as a convenient variable to denote the load level. The load at time, $t + \Delta t$, can then be written as:

$$ {}^{t+\Delta t}\{f\} = {}^{t}\{f\} + \{\Delta f\} \tag{4.30} $$

where: $\{\Delta f\}$ is the incremental force vector and ${}^{t}\{f\}$ is the external force vector for the previous step.

Assuming equilibrium, the applied load should be equivalent to the internal force vector, $\{R\}$, after each load step, i.e. ${}^{t}\{f\} - {}^{t}\{R\} = 0$. Therefore, from Equation 4.30:

$$ {}^{t+\Delta t}\{f\} - {}^{t}\{R\} = \{\Delta f\} \tag{4.31} $$

The general FEA Equation, 4.5, when changed to an incremental loading situation becomes ${}^{t}[k]\{\Delta q\} = \{\Delta f\}$, where $\{\Delta q\}$ is the incremental displacement for the current load. This can now be written as:

$$ {}^{t}[k]\{\Delta q\} = {}^{t+\Delta t}\{f\} - {}^{t}\{R\} \tag{4.32} $$

and the total deflection can be determined from:

$$ {}^{t+\Delta t}\{q\} = {}^{t}\{q\} + \{\Delta q\} \tag{4.33} $$

The change in deflections, stresses, strains and contact status may require the recalculation of the stiffness matrix prior to applying the next load step. The procedure is repeated until the full load is applied.

Note that because the stiffness matrix used is a tangential matrix used from the previous loading condition, that the resulting solution is only an approximation. This may result in a significant error in the final solution as shown in Figure 4.9A. Therefore, we must use an iterative technique to obtain sufficient accuracy. Figure 4.9B illustrates the use of the Newton-Raphson iterative technique to achieve convergence.

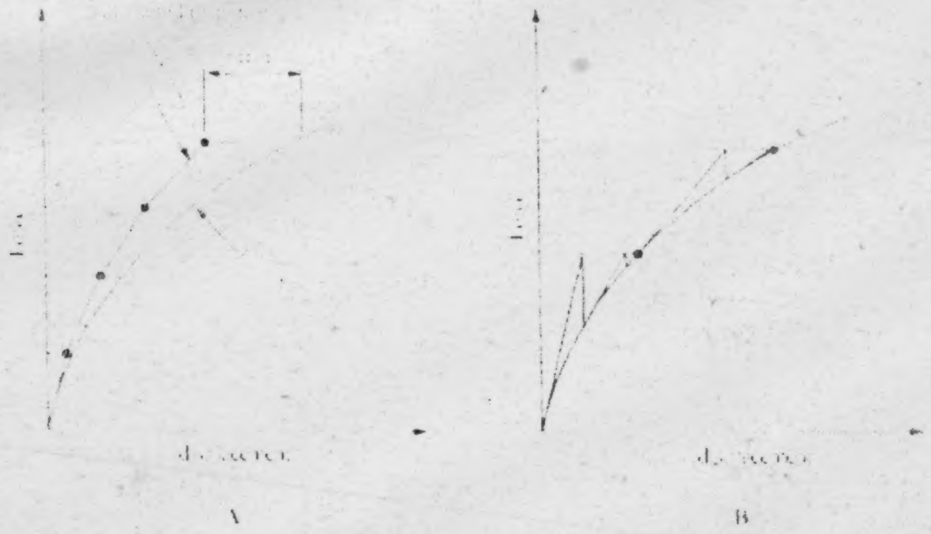

Figure 4.9: Illustration of a nonlinear solution not using iterations (A) and using the Newton-Raphson iterative technique (B). Modified from ANSYS[1].

Using this method, Equations 4.32 and 4.33 become:

$$
\begin{aligned}
{}^{t+\Delta t}[k]^{(i-1)}\{\Delta q\}^{(i)} &= {}^{t+\Delta t}\{f\} - {}^{t+\Delta t}\{R\}^{(i-1)} && (4.34)\\
{}^{t+\Delta t}\{q\}^{(i)} &= {}^{t+\Delta t}\{q\}^{(i-1)} + \{\Delta q\}^{(i)} && (4.35)
\end{aligned}
$$

where the initial conditions are ${}^{t+\Delta t}\{q\}^{(0)} = {}^{t}\{q\}$, ${}^{t+\Delta t}[k]^{(0)} = {}^{t}[k]$, ${}^{t+\Delta t}\{f\}^{(0)} = {}^{t}\{f\}$. Note that a modified Newton-Raphson technique could also be applied in which the stiffness matrix is not updated after each iteration. This generally results in decreased computational time, however, it can be less stable.

As stated previously, there are three common classes arising in structural problems; material nonlinearities, geometric nonlinearities, and contact. All three of which must be accounted for when modeling the spine for scoliosis surgery. These classes will now be discussed in detail.

4.7.1 Material Nonlinearities

Material nonlinearities arise when the stress-strain relationship is nonlinear, a condition exhibited in both spinal ligaments and intervertebral discs (see Figure 2.14). As shown in Figure 4.10, the typical sigmoid shape of the stress-strain curve for a ligament placed in tension can be represented as a multilinear model. To account for material nonlinearities, the element strain must be determined following each load step. The stress-strain graph is then used to determine the appropriate Young's Modulus. The stiffness matrix is then updated to reflect any changes in material properties. Figure 4.10 displays a typical finite element run for a single spinal ligament. In addition, we want to account for the inability of ligaments to act in compression. Therefore, a negative strain would result in no stress on the ligament. In addition, most ligaments begin in a state of prestress, therefore we must also be able to account for this.

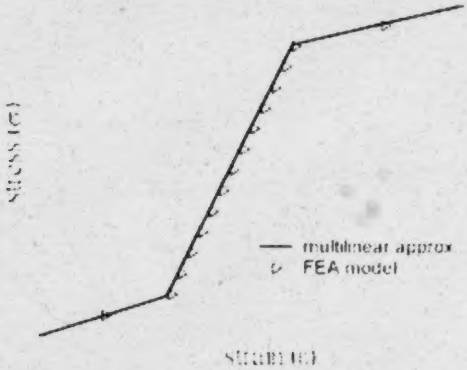

Figure 4.10: Modeling of a ligament placed in tension. For clarity, Newton Raphson iterative steps were not displayed in this figure.

4.7.2 Geometric Nonlinearities

There are several situations, including the spine during scoliosis surgery, where the geometry of a structure is significantly altered by the loads applied to it. When this is the case, the element stiffness matrices cannot be assumed to remain constant as is done in linear finite element analysis. Instead, the stiffness matrices are assumed to be a function of the deflections, thereby making the problem nonlinear. These nonlinearities, known as geometric nonlinearities, can be further classified into two categories: (i) large displacement, large rotations, but small strains and (ii) large displacements, large rotations, and large strains[3]. For the model of the scoliotic spine, both types of geometric nonlinearities are present. For example, the vertebral bodies will undergo large displacement and large rotations, however, the strains within the vertebrae will be small. In contrast, the intervertebral discs will deform significantly, thereby falling into the latter category.

To illustrate geometric nonlinearities, consider a beam fixed at one end with a moment applied to the free end (as shown in Figure.4.11). In the linear range,

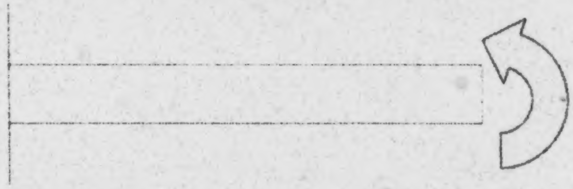

Figure 4.11: Sample loading of a beam used to illustrate geometric nonlinearities.

the deflection of the free end of the beam increases linearly with increased loading according to Equation 4.36[4].

$$y = \frac{ML^2}{2EI} \tag{4.36}$$

However, the true deflection of the free end of the beam follows Equation 4.37[9]. Note that for small deflections these equations are in agreement with each other.

$$y = \frac{EI}{M}\left(1 - \cos\frac{ML}{EI}\right) \tag{4.37}$$

In this case, the geometric nonlinearity is caused by large deflection and large strain. The large deflection is accounted for by updating the stiffness matrix with the new geometry. However, the large strain indicates that the strain equations based on small-displacement theory should not be used[6]:

$$\left\{ \begin{array}{c} \varepsilon_{xx} \\ \varepsilon_{xy} \\ \gamma_{xy} \end{array} \right\} = \left\{ \begin{array}{c} \frac{\partial u}{\partial x} \\ \frac{\partial v}{\partial y} \\ \frac{\partial u}{\partial y} + \frac{\partial v}{\partial v} \end{array} \right\} \tag{4.38}$$

Instead, one of the strain measures used in large deformation analysis should be used. Green strain should be used for problems such as this, involving large displacements, large rotations and large strain[3]. The equations for Green strain can be written as[6], [10]:

$$\left\{ \begin{array}{c} \varepsilon_{xx} \\ \varepsilon_{xy} \\ \gamma_{xy} \end{array} \right\} = \left\{ \begin{array}{c} \frac{\partial u}{\partial x} \\ \frac{\partial v}{\partial y} \\ \frac{\partial u}{\partial y} + \frac{\partial v}{\partial v} \end{array} \right\} + \left\{ \begin{array}{c} \frac{1}{2}\left[\left(\frac{\partial u}{\partial x}\right)^2 + \left(\frac{\partial v}{\partial x}\right)^2\right] \\ \frac{1}{2}\left[\left(\frac{\partial u}{\partial y}\right)^2 + \left(\frac{\partial v}{\partial y}\right)^2\right] \\ \left(\frac{\partial u}{\partial x}\right)\left(\frac{\partial u}{\partial y}\right) + \left(\frac{\partial v}{\partial x}\right)\left(\frac{\partial v}{\partial y}\right) \end{array} \right\} \tag{4.39}$$

Since the derivation of the stiffness matrix for the beam is based on the small strain equations, the original derivation should be modified. Adding in the additional strain equation terms, the stiffness matrix becomes (See Appendix A for the full derivation):

$$\begin{aligned} [k] &= \underbrace{\frac{EA}{\ell^3} \begin{bmatrix} \ell^2 & 0 & 0 & -\ell^2 & 0 & 0 \\ 0 & 12 & 6\ell & 0 & -12 & 6\ell \\ 0 & 6\ell & 4\ell^2 & 0 & -6\ell & 2\ell^2 \\ -\ell^2 & 0 & 0 & \ell^2 & 0 & 0 \\ 0 & -12 & -6\ell & 0 & 12 & -6\ell \\ 0 & 6\ell & 2\ell^2 & 0 & -6\ell & 4\ell^2 \end{bmatrix}}_{\text{linear stiffness matrix}} \\ &+ \underbrace{\frac{EA}{30\ell^2} u_{21} \begin{bmatrix} 0 & 0 & 0 & 0 & 0 & 0 \\ 0 & 36 & 3\ell & 0 & -36 & 3\ell \\ 0 & 3\ell & 4\ell^2 & 0 & -3\ell & -\ell^2 \\ 0 & 0 & 0 & 0 & 0 & 0 \\ 0 & -36 & -3\ell & 0 & 36 & -3\ell \\ 0 & 3\ell & -\ell^2 & 0 & -3\ell & 4\ell^2 \end{bmatrix}}_{\text{nonlinear component}} \end{aligned} \tag{4.40}$$

As shown, the new stiffness matrix is a collection of the linear stiffness matrix and a nonlinear term which is dependent on the displacement in the beam. Now, the stiffness can be updated after each iteration. Assuming that the elements do not change significantly in size and shape, i.e. small strain, the nonlinear portion of the stiffness matrix will be small compared to the linear portion. As such, one can eliminate the nonlinear portion, thereby speeding up processing time and slightly decreasing the accuracy of the system. In doing so, the geometric nonlinearity of the beam is assumed to be one of large deflection, large rotation, and small strain.

For the current cantilever beam, consider the beam divided into 5 elements. The deflection of the free end of the beam was then compared against the linear and nonlinear deflection equations as shown in Figure 4.12. One can see that the theoretical solution for the deflection of the beam was followed relatively closely by the nonlinear solver. While a large number of load steps were required to obtain sufficient accuracy, it is estimated that a large number of load steps will be required for the spinal model to account for other nonlinearities such as contact between the articular facets (discussed in detail in the Section 4.7.3). Therefore, it was assumed that for the scoliotic spine, it is most likely unnecessary to add the nonlinear component of the stiffness matrix. The effect of this simplification will be determined in the final model.

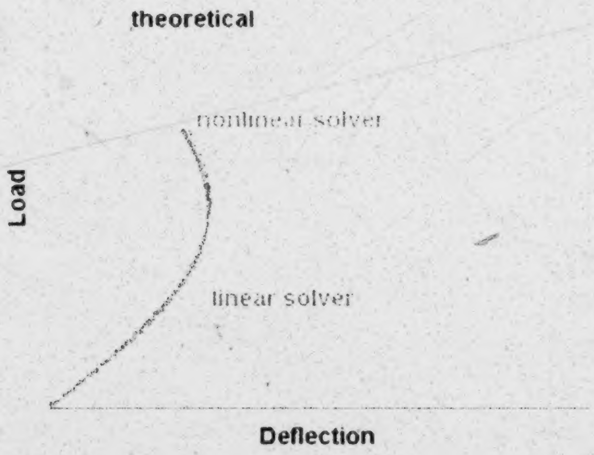

Figure 4.12: Nonlinear and linear deflection of the free end of a cantilever beam. Several load steps were required to obtain sufficient accuracy of the nonlinear solver.

In addition to accounting for large strains, large displacements and large rotations in the stiffness matrices, one must also consider the force vector. During surgery, the hooks inserted onto the transverse processes of the vertebrae are only able to apply a force perpendicular to the surface. Therefore, the direction of this force is dependent on the orientation of the surface of the transverse process, which can change during surgery. Therefore, after each load step, the direction of these surfaces must be determined and the force vector changed appropriately.

4.7.3 Contact Elements

Contact elements must be used when two bodies come into contact during the analysis. Since we cannot accurately predict which elements may come into contact and which may not during a set configuration, the ability to check for contact during the analysis must be included in the model. New constraints or for contact forces can then be applied once contact has occurred.

There are several types of contact that can be modeled using finite element analysis. Of these, the point to surface contact will be focused on, as it is the type of contact used to model the articular facets.

Several geometrical methods can be used to determine if contact has occurred. One common method is the Pinball algorithm, a common method used in ANSYS[1] to check for point to surface contact. This method, illustrated in Figure 4.13, involves the creation of a circle, or pinball, around the contact surface. Should the point (K) intersects with the area of the ball, then contact is considered. The Pseudo element algorithm is then used to determine if the point K has actually penetrated the surface. Several problems exist with this method. If the load step was so large that the point has contacted and gone through the surface then contact does not occur within the model. In addition, considering the geometry involved with the articular facets, these points would likely always be in the pinball region, therefore the time used to perform this algorithm for each contact location would be unnecessary. Furthermore, the Pseudo element algorithm and constraint application method are time consuming procedures which are more complex than desired for the current model.

Instead, a simple geometrical check will be used in the current model. Note that while this method cannot be applied to any problem, we are using this method

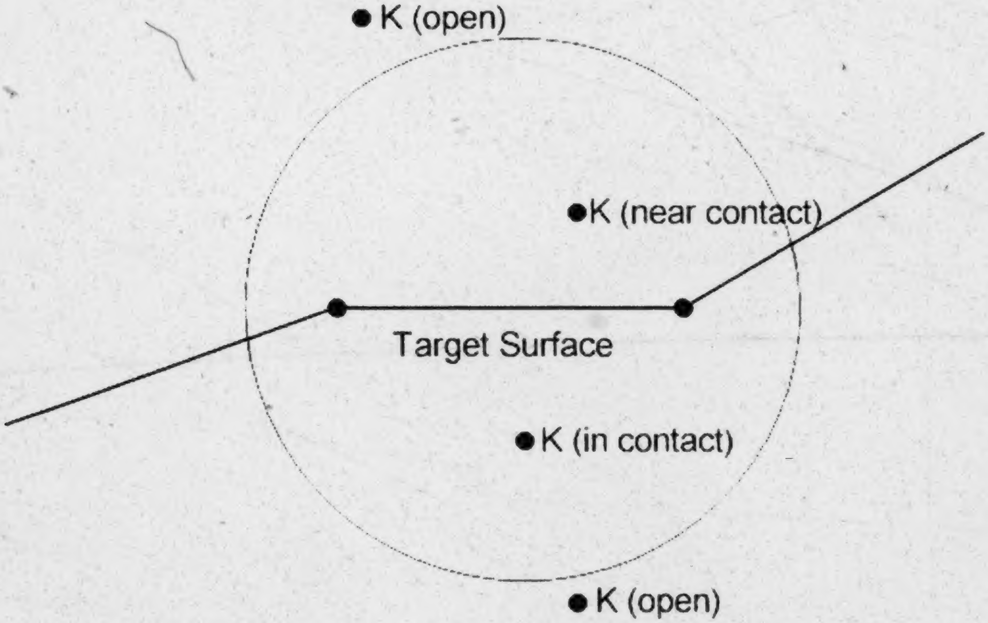

Figure 4.13: Illustration of the Pinball algorithm to check for contact. Modified from ANSYS[1].

for a known geometry and as such we can infer additional information. Using the geometrical check, a vector is created from the new location of the first surface node to the point K as shown in Figure 4.14. A cross product is then performed with the new vector and a vector parallel to the target surface. Should the resulting product be into the page, contact has not yet occurred. Otherwise, should the result be positive (out of the page), then contact has occurred. This method assumes that if the point is on the other side of the surface, then contact has occurred. This is a valid assumption for the articular facets.

Once contact has occurred, the model must be changed to account for this. This involves the application of new constraints. Of the constraint methods discussed, constraint equations using a relation between four degrees of freedom as discussed in Section 4.6.4, will be used to allow the point to slide along the surface but not pass

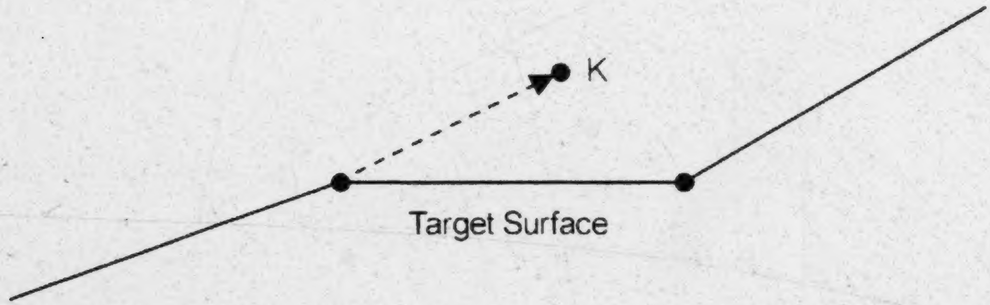

Figure 4.14: Illustration of vector used to check for contact between point K and the target surface.

through it. Note that there is no need to model frictional forces between the facets as the synovial fluid present within the articular capsules minimizes friction.

Chapter 5

Existing Finite Element Models of the Spine

Several finite element models of the spine have been created, however, limitations of these models do exist for the goal of a real time pre-surgical tool. Note that these models were created with different goals in mind, including improving bracing and detailed mechanical analyses of the spine. A brief overview of these models are discussed below.

5.1 A Mechanical Model of the Normal Human Spine

Tong[36] created a three-dimensional linear model of the normal thoracolumbar spine using the commercial finite element package ANSYS. Experimental data from published literature was used to define the geometry and material properties of the normal spine and components. Each of the 17 vertebrae were composed of 182 brick elements while the intervertebral discs were each composed of 49 spring elements. The spinal ligaments were also modeled using linearly elastic spring elements. The need to use contact elements to model the articulations between the facets was avoided through the creation of a "tree suspension" system. Using this system, Tong was able to simulate the gliding motion between the facet surfaces while preventing the surfaces to pass through each other. The model was validated in extension, flexion, lateral bending and axial rotation by using functional units and comparing the stiffnesses to those found in the literature. Most of the results were found to agree within an acceptable range.

This model was intended to set the groundwork for the creation of a scoliotic spine model. While several features of this model were well thought out, such as the use of the facet suspension system to avoid the use of contact elements, limitations do exist. Obvious limitations of the model are the inability to model scoliotic deformities and the exclusion of the thoracic cage. However, the more challenging limitations are the inability to account for nonlinearities and the ability of a surgeon to use the model.

As described in the previous chapter, several nonlinearities need to be accounted for to accurately model surgery on the scoliotic spine. While this model does account for contact between the articular facets, material and geometric nonlinearities are not accounted for. Since the model was only validated for normal physiological movements, this limitation would not have affected those results. However, nonlinearities must be accounted for to model the large deformations associated with scoliosis surgery.

The second limitation, the inability of the surgeon to use the computer model directly, extends from the model being created using a commercial package. ANSYS is a widely recognized commercial finite element package as it has extensive modeling abilities including, but not limited to structural, dynamics, fluids and electromagnetism. As such, the menu structures and command language are complicated, demanding a user who is not only familiar with the theoretical limitations to finite element analysis, but who is also familiar with using ANSYS. It is simply not feasible to have the surgeons commit to the required training.

5.2 A Finite Element Model of the Ribcage

A three-dimensional finite element model was created by Thompson[35] to explore the articulations between the ribs and the vertebral column in orthopedic bracing. The model was comprised of the vertebral segment from T5 to T7 including the intervertebral discs, ribs 6 and 7, the corresponding portion of the sternum and all associated ligaments. The ribs were modeled using beam elements while the ligaments and intervertebral discs were modeled using truss elements.

This model does appear to accurately account for the geometrical structure of the undeformed ribcage, however there are again several limitations restricting usage. First of all, this model only accounts for a small portion of the ribcage and needs to be expanded to account for the entire thorax. Similar to Tong's model, this model assumes normal geometry and does not account for scoliotic deformations, nor does it account for nonlinearities present in the model. Contact elements were not even considered as articulation of the ribs with the vertebrae and sternum were either modeled using a series of trusses or held fixed. To model the inability of ligaments to exert compressive forces, results were verified after each run and those ligaments found to be in compression were eliminated. This is not the optimal way to account for this, as throughout the loading an individual ligament may exert tension for a portion of the analysis and compression for the remaining portion.

Again, this model uses a commercial finite element package and therefore has the same limitations described above.

5.3 Simulation of Scoliosis Derotation Maneuver

Mack and Stokes[31] utilized ANSYS to create a model of the thoracic spine to simulate the rod rotation maneuver in scoliosis surgery. The model consisted of seven equally spaced vertebrae in an idealized planar geometry. The six motion segments were modeled as three-dimensional beam elements matched to experimentally determined normal thoracic spine stiffnesses. A feature of this model is that it simulates three stages of surgery: fitting the curved rod to the hooks, the rod rotation maneuver, and locking the hooks to the rod. However, this model also has several limitations. The model does not account for patient specific geometry or material properties, the ribcage and remaining spinal units, material nonlinearities, or contact between the articular facets. Furthermore, as previously discussed, several limitations exist on this model due to the use of a commercial finite element package.

5.4 Simulation of Scoliosis Surgery using FEM

Using ANSYS, Tamaki et al.[33],[34] developed a nonlinear three-dimensional model of the vertebral column, thorax, and pelvis. Similar to the model presented by Tong, solid brick elements were used to model the vertebra, but nonlinear spring elements were used to model the intervertebral discs and ligaments. The tension only capabilities of the ligaments were also accounted for in this model. Contact between the articular facets is modeled through the use of springs with the stiffness being proportional to the displacement of the facet. This eliminates the use of contact elements which can have convergence problems. While nonlinear material properties and contact has been addressed with this model, the author does not discuss the geometric nonlinearities within the model. Geometry was imported for each patient from CT images and loads were obtained from surgery. While a quantitative comparison of the results has not yet been completed, the resulting morphology of the model appears to correlate well with the final patient x-rays. Further studies are being performed to obtain more accurate geometrical representation and material properties.

The use of a commercial finite element tool, as stated previously has several limitations. In addition to those mentioned previously, the computational times are generally quite large. Using this model, anywhere from 5 to 30 minutes are required for each load case. This can be attributed to several factors including using an inefficient solver for the specific geometry and the high tolerances implemented in ANSYS. Data input into the model from the CT scans has a much lower precision than the results being obtained. While we can simply ignore the additional significant digits, perhaps there are some simplifications that can be made to the solver which would decrease the computational times involved in each run.

5.5 Modeling of the Spine and Thorax for the Analysis of Scoliotic Deformities Using FEM

Perhaps the most widely used and praised finite element model of the scoliotic spine and thorax is that developed in collaboration between researchers at L'Ecole Polytechnique in Montreal and L'Ecole Nationale Supérieure des Arts & Metiérs in France[2]. The main focus of the research was to create a personalized finite element model to study the biomechanical behavior of the spine and thorax including details such as the articular facets This model was developed using ANSYS and consists of 1356 nodes and 2807 elements and makes use of geometric, material and contact nonlinearities.

However, the authors have indicated that both constraint equations and geometric nonlinear properties are accounted for using ANSYS. ANSYS does not recommend the use of constraint equations with nonlinear geometry[1]. One should note however, that this model has been used primarily to study the use of bracing, which does not involve the same level of geometric nonlinearity, therefore the limitations of the constraint equations may not be as critical.

While this model does include an advanced geometrical representation of the scoliotic spine and thorax, it does utilize a commercial product which has several drawbacks, discussed previously. This model can also take up to 30 minutes to run depending on the complexity of the loading situation.

5.6 Virtual Reality Scoliosis Surgery Simulator

Plouznikoff et al.[27] have developed a virtual reality simulator of the spine to enable surgeons to practice a scoliosis instrumentation surgery. This simulator includes not only a geometric reconstruction of the spine but a full reconstruction of the operating room complete with the operating table, cupboards and lights to immerse the surgeon in a familiar location. The surgeon interacts with the finite element model which includes a rigid body model of the vertebrae and an elastic beam model of the intervertebral discs. All other structures have been neglected in order to allow for real time processing (0.6 seconds). Forces are applied to the model using a proportionality factor that translates the surgeons movements.

While this model should be useful in training new surgeons, it is not feasible for a surgeon wanting to try several different loading configurations for each patient. Each trial would involve starting from the beginning and repeating the surgery with minor adjustments to the applied forces and insertion locations. Repeatability error would play a role as the surgeon may not be able to replicate the exact motion between trials.

The model itself is also limited as the vertebrae are currently represented as rigid bodies. A study performed by Aubin et al[2] found that the Young's Modulus of the vertebrae is significant in scoliosis surgery. This may be because while the vertebral body is rigid in comparison with the other spinal components, the vertebral arch is more flexible. The model also neglects several key anatomical structures such as the ribcage and ligaments.

5.7 Conclusions

Based on the above literature survey, several limitations exist with the current models in terms of creating a real time scoliotic tool that surgeons can use. These limitations include, the inability to account for scoliotic deformations, the inability to model patient specific geometry and material properties, the inability to use constraint equations and geometric nonlinearities together, the large computational time requirements and the difficult menu structures and command languages used to manipulate the models. Therefore, a pre-surgical finite element model of the spine must incorporate the following abilities:

- Create a model that not only accounts for scoliotic deformities but is patient specific in terms of geometry and material properties.
- Incorporate material nonlinearities, geometric nonlinearities and contact elements.
- Allow for real time processing through the use of condensation, sparse element storage and other time saving simplifications.
- Include a user friendly interface that surgeons will use.

Chapter 6

The Scoliotic Spine Model

The ultimate goal of this work is to create a real-time three-dimensional finite element model of the scoliotic spine and ribcage to be used by the surgeon to test surgical procedures. To provide a foundation from which the final model will be created, a two-dimensional prototype of the computer model which incorporates all of the necessary features of the final model was first required. This is the basis for the current work.

The two-dimensional prototype model, known as femSpine, was created in Matlab® and includes the thoracic and lumbar vertebrae. The respective intervertebral discs and ligaments in addition to a simplified model of the ribcage is incorporated in this prototype. Details of this model are discussed further in this chapter.

6.1 Graphical User Interface

As shown in Figure 6.1, the graphical user interface, or GUI, is comprised of four main components; the Menu Bar, the Control Window, the Dialog Box and the Visual Display Window. The Menu Bar offers several additional program features which will be discussed further at the end of this chapter. The Control Window consists of a series of subwindows which guide the user through the creation and analysis of the scoliotic spine model. These steps consist of: creating the scoliotic geometry, adding constraints, defining loads, solving the test case, and viewing the results. Should the user decide to change a parameter in an earlier step, the program will automatically return to that step without having to start all over again. The Dialog Box is used to give instructions or prompt the user when required. Throughout the analysis, the model is illustrated in the Visual Display Window.

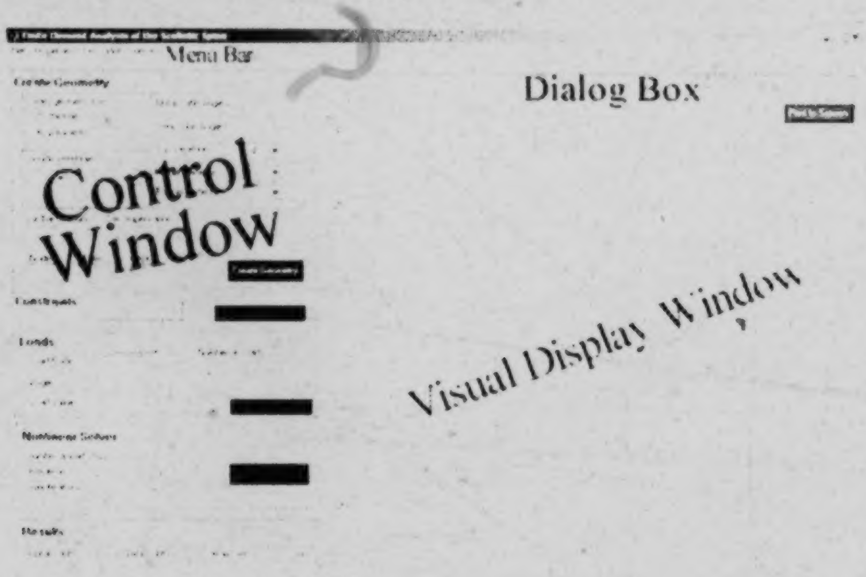

Figure 6.1: Graphical user interface of the current finite element model.

6.2 Creating the Geometry

6.2.1 Vertebrae and Intervertebral Discs

Personalized geometric data of the spine can be input into the model using data from x-rays or using scoliotic parameters defined earlier. Both methods are discussed in detail.

Scoliotic Parameters

Using the scoliotic parameters previously defined: α and β Cobb Angles, Decompensation and Lumbar Obliquity, a scoliotic curve can be approximated. As this code is only two-dimensional, axial rotation is not accounted for. Presently, the model only accounts for double curves - KING Types I, II, or V as these are most prevalent in adolescent idiopathic scoliosis. However, single curves can be input using the X-ray Data File method described in the following subsection.

The user is able to select a variable number of vertebrae from Thoracic 1 ($T1$) to Lumbar 5 ($L5$). This allows the user to minimize the complexity of the model by limiting it to the required spinal units. The user must then specify the α and β Cobb Angles in addition to the vertebrae span over which they occur. Note that a positive α angle indicates a right curve while a positive β angle depicts a left curve. Lumbar Obliquity must also be specified by the user, positive indicating a counterclockwise rotation. Note that all angles are measured in degrees.

Vertebral geometry is approximated using data from Panjabi et al.[23] and [25], shown in Figure 6.2. Note that these measurements were averaged from 60 subjects with an average age of 46 years. While this data set may not accurately represent the typical adolescent with scoliosis, it was deemed an adequate for initial testing.

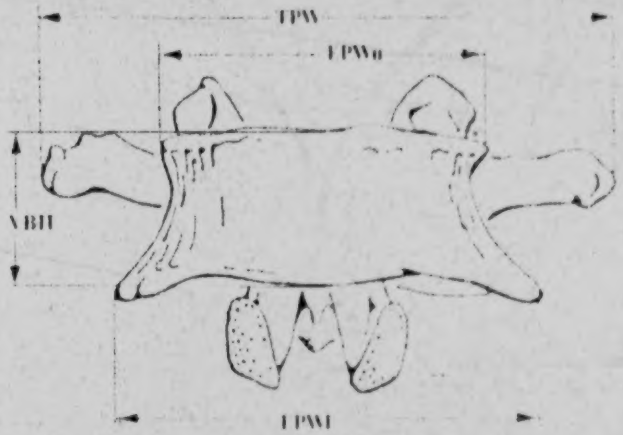

Figure 6.2: Anterior view of the vertebral body measurements obtained from Panjabi et al. Dimension notations shown in Table 6.1. Modified from Panjabi[24].

The average between the upper and lower end-plate is used to describe the width of each vertebra ($EPWavg$), while VBH is used to describe the height of each vertebra. The Transverse process width (TPW) was also obtained from Panjabi et al., while

Table 6.1: Vertebral Body Dimension Notations

Dimension	Description
EPWu	End-plate width (upper)
EPWl	End-plate width (lower)
TPW	Transverse process width
VBH	Vertebral body height

the Transverse process height (TPH) and the intervertebral disc height (IDH) was estimated from a spinal model.

For illustration purposes, the spinal geometry, shown in Figure 6.3, will be created for a fictional patient with an α Cobb Angle of 60° from $T4$ to $T9$, a β Cobb Angle of 50° from $T9$ to $L3$, and a Lumbar Obliquity of 10°.

The user first enters the scoliotic curve parameters using the graphical user interface (GUI) as shown in Figure 6.4. The user will then press the "Create Geometry" button to start the function. Note that the scoliotic curve cannot extend past L3 for the purpose of this model. This is due to the assumption that the sacrum is oriented horizontally.

Using $(0,0)$ as a starting location, the function first locates the bottom of $L5$, (b) using the height of the intervertebral disc, (IDH_{L5}), as shown in Figure 6.5. Note that the final geometry is shown for clarification purposes. The top of $L5$, (a), is then defined at an angle of LO° and the predefined height of VBH_{L5}. $L4$ is also assumed to be rotated by LO°, and IDH_{L4} is then used to determine the bottom of $L4$

The geometry is created in a similar fashion until the bottom of the Beta curve is reached. In this case, this is the top of $L4$. As shown in Figure 6.6, the bottom vertebra in the curve is then assumed to be rotated at a degree of ϕ_1,defined as:

$$\phi_1 = LO + \frac{\beta}{8} = 10^\circ + \frac{50^\circ}{8} = 16.3^\circ \tag{6.1}$$

This was determined to be a reasonable approximation after visual tests with several scoliotic x-rays. Note that this is only an approximation and does vary from patient to patient. Using IBH_{L3} and ϕ_1, the location of b_{L3} can be determined. The curve length, ℓ_{T9-L3}, is then calculated as the sum of the VBH and IDH for the vertebrae included in the curve. This is used to determine the origin of the circle, O_β:

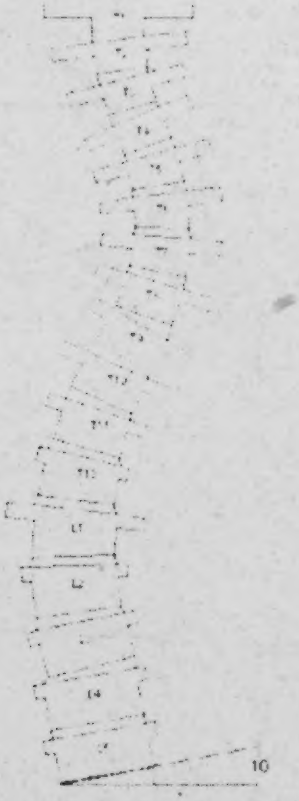

Figure 6.3: Posterior view of the Spinal Model for Cobb angles $\alpha = 60°$, $\beta = 50°$, and Lumbar Obliquity, $LO = 10°$.

$$O_\beta = b_{L3} + \frac{\ell_{T9-L3}}{\beta}\left\{ \cos\phi_1 \quad \sin\phi_1 \right\} \tag{6.2}$$

where b_{L3} is the point at the bottom of $L3$ and β is the Cobb angle measured in radians. The top and bottom points of the vertebrae on the curve are then located using the origin of the curve and summing the vertebral and intervertebral heights. Note that the top vertebra on the curve will now be rotated by ϕ_2 which is defined as:

$$\phi_2 = \phi_1 - \beta = 16.3° - 50° = -33.8° \tag{6.3}$$

Similarly, the α curve is created by first determining the origin of the circle from

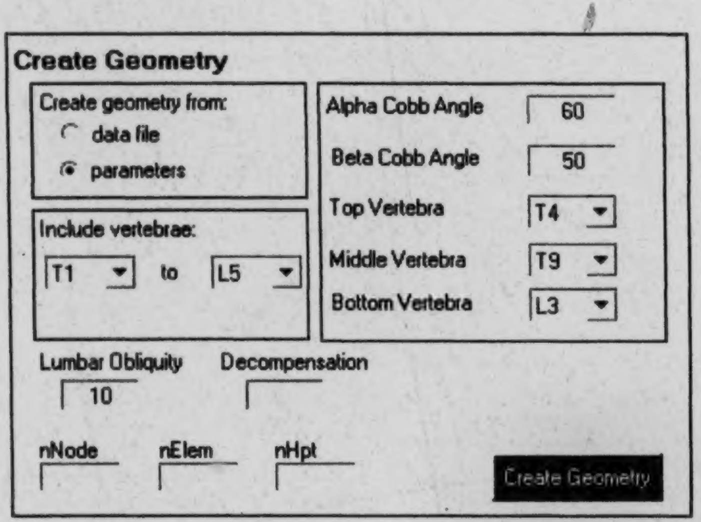

Create Geometry

Create geometry from:
○ data file
● parameters

Include vertebrae: T1 to L5

Alpha Cobb Angle: 60
Beta Cobb Angle: 50
Top Vertebra: T4
Middle Vertebra: T9
Bottom Vertebra: L3

Lumbar Obliquity: 10
Decompensation:

nNode:
nElem:
nHpt:

Figure 6.4: Graphical user interface of the 'Create Geometry' section of the Control Window. The entries for the test geometry are shown.

the sum of the respective intervertebral and vertebral heights and then locating the top and bottom vertebral points. The top vertebra on the α Cobb angle will be rotated by ϕ_3, where $\phi_3 = \phi_2 + \alpha$. In this case, $\phi_3 = 26.3\,°$.

The top vertebra is assumed to be oriented horizontally, therefore the rotation the remaining vertebrae are decreased by 50% from the rotation of the vertebra inferior to it. In this case, T3 is rotated by $\phi_3 * 50\% = 13.1$ degrees. while T2 is rotated by $(13.1) * 50\% = 6.6$ degrees.

Now that the vertebral points have been located as shown in Figure 6.9, the vertebrae and intervertebral discs can be created.

For clarification, this will be illustrated for the creation of Vertebra $L5$. First, a third point, c, is added to the vertebra, shown in Figure 6.10 This point defines the height of the transverse process and is thus located at a distance of TPH from point a. Then the outline of each vertebra is created using 10 keypoints, 1 - 10 as shown in Figure 6.10. Keypoints 1-2, 5-6, and 9-10 are located at a distance of $\frac{EPW_{avg}}{2}$ from points b, c, and a respectively. Keypoints 3-4 and 7-8 are defined at a distance of $\frac{TPW}{2}$ from points c and a respectively. The intervertebral discs are created from keypoints 9 to 10 from the inferior vertebra and keypoints 1 to 2 from the superior

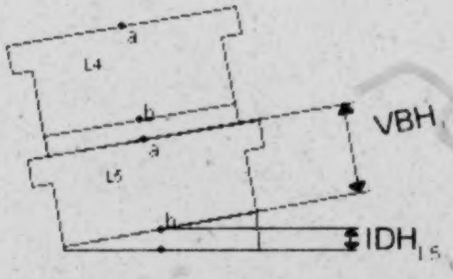
a
L4
b
a
L5
b
VBH_{L5}
IDH_{L5}

Figure 6.5: The top (a) and bottom (b) points are located for L4 and L5 using the geometric data from Panjabi et al. and the scoliotic parameters.

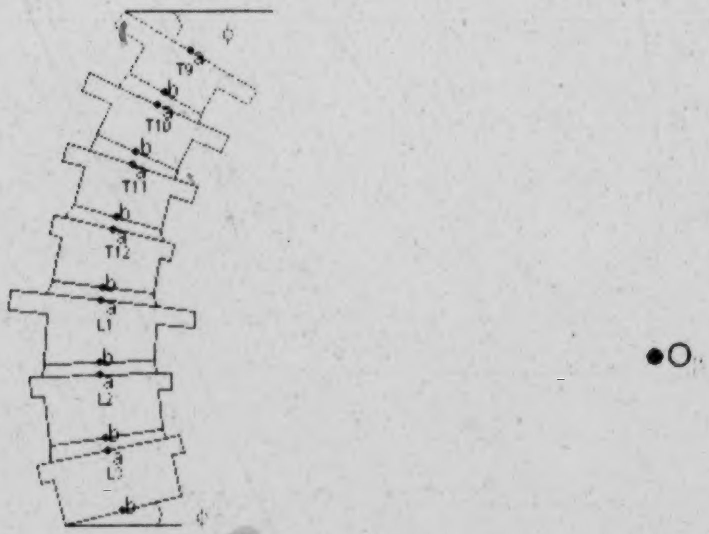
φ
a
T9
b
a
T10
b
a
T11
b
a
T12
b
a
L1
b
a
L2
b
a
L3
b
φ
O

Figure 6.6: The beta curve is created by locating a geometric center, determining the curve length and assuming a starting angle of rotation of $L3$.

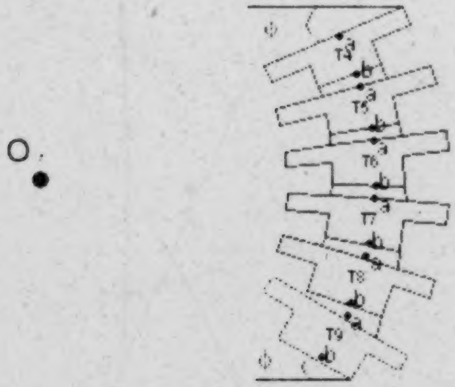

Figure 6.7: The alpha curve is created by locating the geometric center and determining the required curve length.

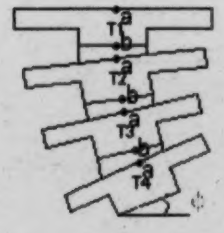

Figure 6.8: The remaining vertebral superior to the alpha curve are created by assuming the vertebral body rotation decreases by 50% compared to the vertebra inferior to it.

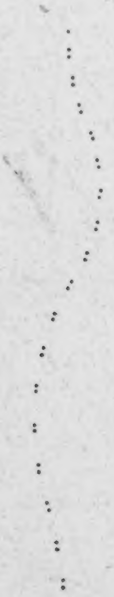

Figure 6.9: The vertebral points for the defined scoliotic curve.

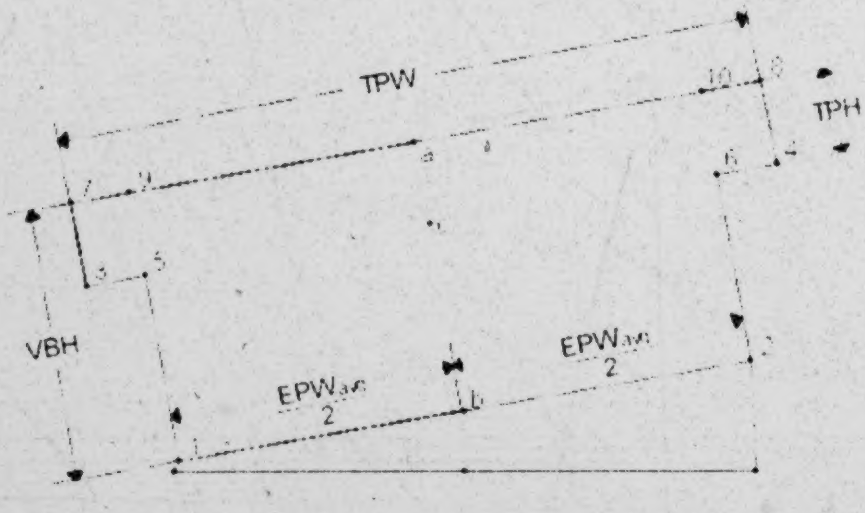

TPW
10
8
TPH
7
9
6
5
VBH
EPW
2
EPW
2

Figure 6.10: Location of the keypoints, numbered 1-10, from the data points previously described.

vertebra.

The model is also capable of accounting for the wedging previously described in Section 3.1.1 by using wedge ratios. The ratios are currently set to those described by Stokes et al.[31], but can easily be changed to accommodate other ratios. This is shown in Figure 6.11.

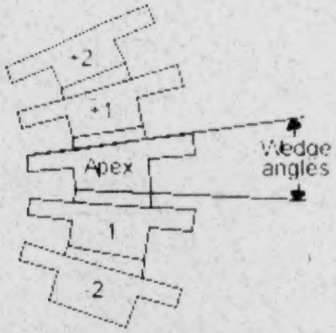

Figure 6.11: Vertebral body wedge angles described by Stokes et al.[31].

Obviously, there were several assumptions made to create the scoliotic curve above. Due to these large variations, patient specific geometry is important in the creation of the model. Therefore, the option to create the model based on x-ray data is also available.

X-ray Data File

It is anticipated that within the next year, digital x-rays will be taken for patients prior to surgery. This data will be transmitted into the model, and will thereby enable the creation of a geometry specific model. However, for this work, digitized x-ray data was obtained by manually selecting points from x-rays. This data can then be read in to the finite element model.

For the purpose of this model, only the four points per vertebra, illustrated in Figure 6.12, were recorded. The relative sizes of the vertebra were then estimated based on the geometrical data from Panjabi et al.[24][23],[25]. To create the remaining vertebral keypoints, shown in Figure 6.13, the Transverse Process Height (TPH)

was estimated from a spinal model and the Transverse Process Width (TPW) was obtained from Panjabi et al.

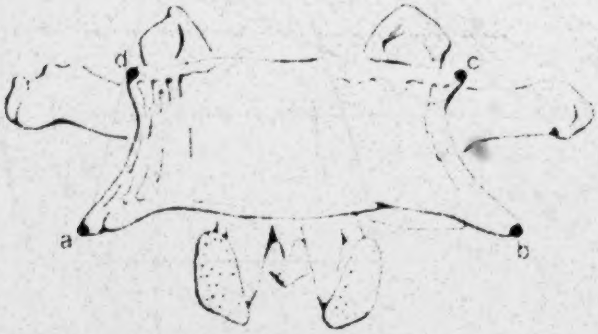

Figure 6.12: Anterior view of the four locations recorded to be read into the finite element model.

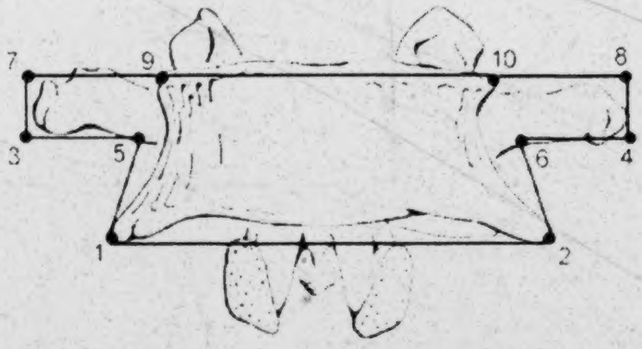

Figure 6.13: Creation of the vertebral body keypoints from the recorded x-ray data.

While this method allows for the creation of an improved geometric representation of the scoliotic curve, it is not feasible for widescale use due the large error in accurately manually locating each point and the time investment required for data collection. However, once digitized x-rays become available, this time consuming and error laden process will be eliminated.

Discretization

The vertebrae and intervertebral discs are then meshed using two-dimensional isoparametric elements. The four noded isoparametric element was chosen to simplify meshing of the asymmetrical scoliotic discs and vertebrae. While triangular elements could also be used to simplify meshing, the constant stress and strain of triangular elements was undesirable.

To start the meshing, the vertebral bodies are first segregated into the upper (a) and lower (b) segment as shown in Figure 6.14.

Figure 6.14: Segregation of the vertebral body into 2 mesh areas.

The discretization of part a can be modified by changing the number of nodes over the width (naw) and the number of nodes over the height (nah). Similarly, the discretization of part b is dictated by the number of nodes over the width (nbw) and the number of nodes over the height (nbh). A sample mesh is shown in Figure 6.15.

The intervertebral disc is meshed in a similar way, using the number of nodes over the disc height (ndh), and the number of nodes over the disc width (ndw). Note that for the nodes to match up at the disc-vertebra interface, ndw must be equal to nbw.

Hardpoints

When using finite elements, loads and constraints can only be applied directly to the nodes. It is therefore often necessary to relocate nodes to potential loading locations, often termed hardpoints. In this model, the hardpoints represent the locations the surgeons are likely to place screws and hooks during the surgery. Top hooks can be placed on the transverse processes of vertebrae $T1$ - $T3$, while vertebrae $T1$ - $T12$

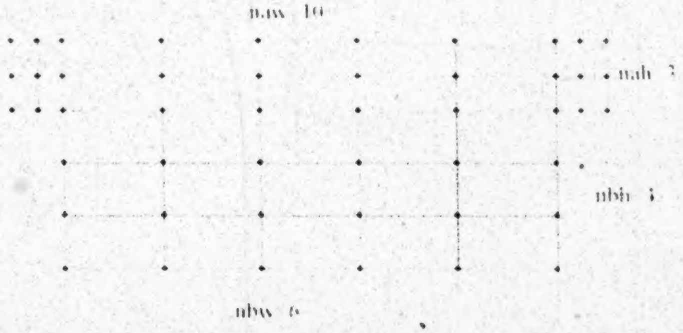

Figure 6.15: Sample discretization of the vertebral bodies.

can have lower hooks applied. The top hooks locations are centered along the upper edge of the transverse process as shown in Figure 6.16. The lower hooks positions are at one-quarter and three-quarters along the inferior edge of the vertebral body. Note that while the hook itself is applied to the transverse process, this is the best representation for the hook location with the two-dimensional model. Once the model is expanded to a three-dimensional model, the location of the lower hooks will be better represented. The screws can be applied to vertebrae $T10$ - $L5$, also shown in Figure 6.16. The screw locations are midway between the upper edge of the vertebra and the bottom edge of the transverse process in the transverse plane, and one-twelfth of the width of the vertebral body from either edge in the sagittal plane.

Once meshing is complete, the closest nodes are relocated to these hardpoints. The stiffness matrices are then assembled for each vertebrae.

Super-elements

The assembled stiffness matrices of each vertebra are then condensed to create super-elements. These super-elements only include the nodes along the upper and lower vertebral body edges, in addition to the hardpoints and the inferior corners of the transverse process. For example, vertebra $T11$ shown below in Figure 6.17 is condensed from 32 nodes down to 18 nodes. Note that the final number of nodes is

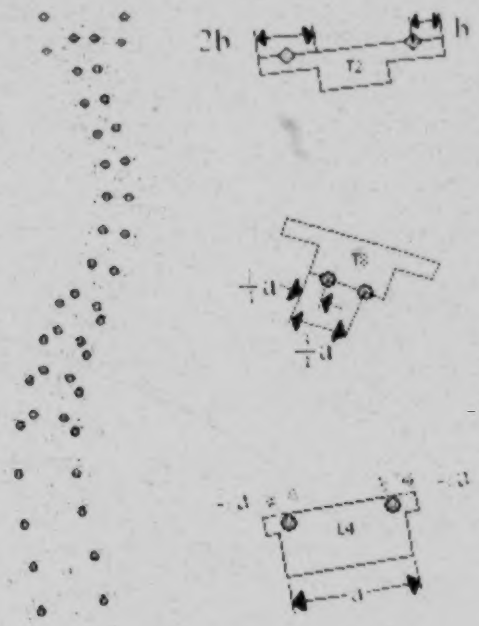

Figure 6.16: Location of the screw and hook hardpoints for the spinal model.

dependent on the mesh size chosen.

Using Equation 4.17, the stiffness matrix for each vertebra is modified. In this case, k_{T11} was a 64×64 matrix, becoming k^{*}_{T11}, a 36×36 matrix. This accounts for a storage reduction of 62% (8720 kilobytes) for the entire system. Recall however that this problem requires a nonlinear solver and as such, the stiffness matrix must be recalculated after each load step. However, if the vertebral body can be considered rigid compared to the remaining model, the stiffness will remain relatively constant. Therefore, only the rotation of the body will change the stiffness matrix. Therefore, the original stiffness matrix and the angle of each vertebra is calculated. Following each load step, a rotation matrix, $[R]$, is used to recalculate the vertebral body stiffness matrix as shown in equation 6.4.

$$[R]^T [k_e] [R] \{q\} = \{f\} \tag{6.4}$$

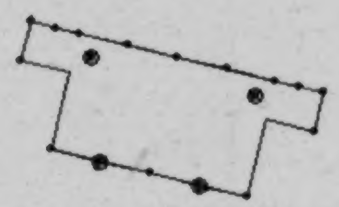

Figure 6.17: Condensation of a vertebral body from 32 nodes to 18 nodes.

Facets

Articular facet joints are added to the thoracic vertebrae using triangular elements as shown in Figure 6.18. Each facet is modeled as one single triangular element with nodes at the outer edge of the vertebral body, on the first interior node on the vertebral body and 3/4 of the way between the vertebrae, along the intervertebral disc edge. The model uses a node to surface contact with the latter node being the contact node the top of the inferior vertebral body being the target surface. This contact method, discussed in Section 4.7.3, assumes that if the node is on the other side of the surface, then contact has occurred.

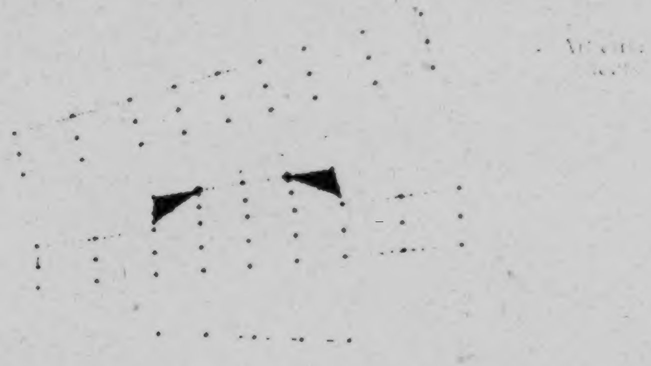

Figure 6.18: Articular facets are modeled as triangular elements on the superior vertebra which can contact the top of the inferior vertebra.

Due to the severity of many scoliotic curves, the space between vertebrae can be

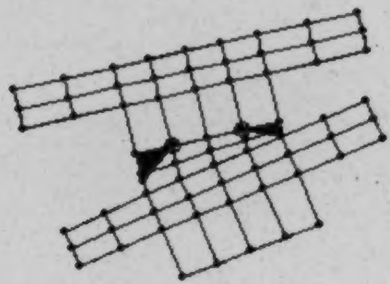

Figure 6.19: Facet height restrictions are placed on intervertebral spaces that are too large or too small as shown on the left side and right side of this model respectively.

quite large. Since this does not correlate with a larger facet joint, an upper limit of 5.0 cm is placed on the height of the triangular element. This is illustrated in Figure 6.19 where for the triangular element height on the left hand side is limited to 5.0 cm. Similarly, the intervertebral space can be quite small and therefore a lower limit of 3.0 cm exists. However, in severe cases as shown in Figure 6.19 where the intervertebral space on the right is less than 3.0 cm, the articular facet height is equivalent to the intervertebral space and it is assumed that contact has already occurred.

Currently, constraint equations are written to stop the articular facet point from going through the surface of the inferior vertebrae, while allowing the facet point to slide along the surface. The resulting equation can be written as:

$$-q_1 \sin\theta + q_2 \cos\theta = -q_3 \sin\theta + q_4 \cos\theta \tag{6.5}$$

where θ is the incline of the inferior vertebral surface, q_1 and q_2 are the x and y degrees of freedom respectively for the facet point and q_3 and q_4 are the x and y degrees of freedom respectively for a node on the vertebral surface. Following each load step, the geometrical check discussed in Section 4.7.3 is used to determine if contact has occurred for any facet joints that are not already in contact. If so, additional constraint equations are added. Internal forces are checked after each load step to ensure that facet joints that are in contact should remain in contact. The constraint equations are eliminated should they no longer be required. This process will be discussed further in the Solver Section below.

Material Properties

At this time, the vertebral body is not segmented into cortical bone and cancellous bone. Assigning appropriate material properties to the vertebral body elements is therefore somewhat difficult. However, because the vertebral body is much stiffer than the intervertebral discs, it is hypothesized that the discs will incur most of the deflection. Testing will be performed to verify this using a range of stiffnesses between 100 and 12000 MPa. A Poisson's ratio of 0.3 and a thickness of 30 mm was used for the vertebral bodies. The material properties used for the intervertebral discs were: Modulus of Elasticity of 2.0 MPa, Poisson's Ratio of 0.47, and a thickness of 30 mm.

6.2.2 Ligaments

Currently, only the intertransverse ligaments are included in this model as they are the only ligaments which contribute significantly to spinal stiffness in the frontal plane. These ligaments are modeled as nonlinear two-dimensional truss elements connecting the transverse processes of adjacent vertebra as shown in Figure 6.20.

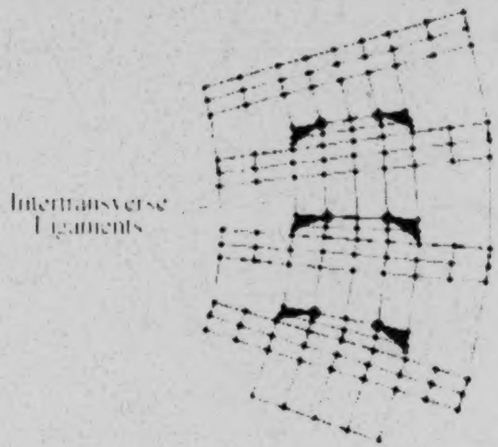

Figure 6.20: Intertransverse ligaments are modeled as nonlinear two-dimensional cable elements connecting the transverse processes of adjacent vertebrae.

Again, material properties are highly variable and studies have shown a large range of values. Currently, the stress-strain curve used for the intertransverse ligaments is a multilinear curve shown in Figure 6.21. The cross sectional area each ligament is assumed to be 2 mm^2.

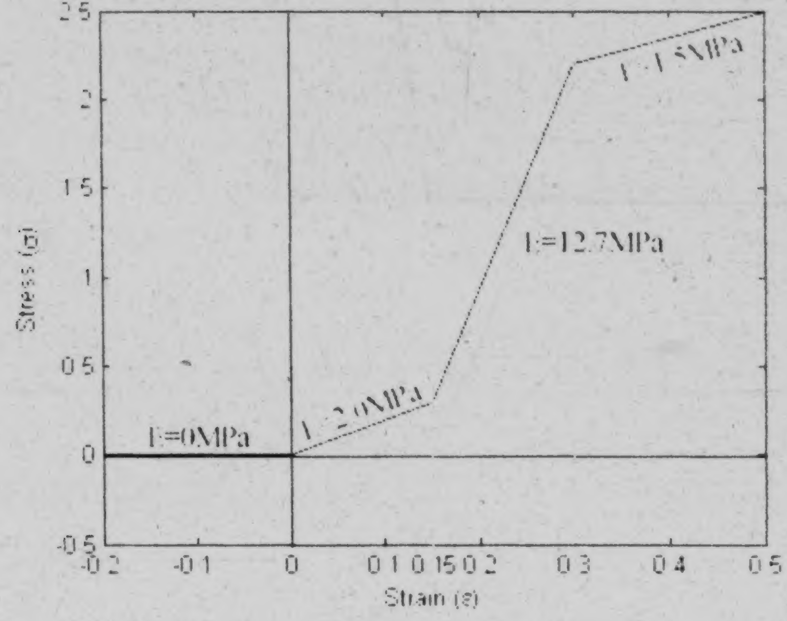

Figure 6.21: Mulitlinear material properties used for the intertransverse ligaments.

As stated previously, many ligaments start out in a state of prestress. Currently, all of the intervertebral ligaments are prestressed to 0.2 MPa. However, this is only an estimate based on the normal spine and does not account for scoliotic deformities. Ultimately, this value will differ for each ligament dependent on the patient geometry and ligament strength.

6.2.3 Thoracic Cage

Currently, a simplified representation of the ribcage is included in the model to increase the lateral stiffness of the thoracic spine. As depicted in Figure 6.22, this model is comprised of 10 rib pairs and sternum. Each rib is modeled as a two-dimensional truss element pinned to the superior point of the respective transverse process. The truss element was selected due to the simplicity of this element. Ribs 1 through 7 attach to separate points on the sternum, at vertical locations equivalent to the average height of the left and right transverse process nodes. Ribs 8 through 10 are attached to the same node as Rib 7 to represent the corresponding anatomical attachment. The false ribs, attached to Thoracic vertebrae 11 and 12 are not included as they do not provide stiffness to the spine. Note that the sternum was modeled using one-dimensional truss elements and therefore only add y-directional stiffnesses to the problem. This accounts for the vertical orientation of the sternum.

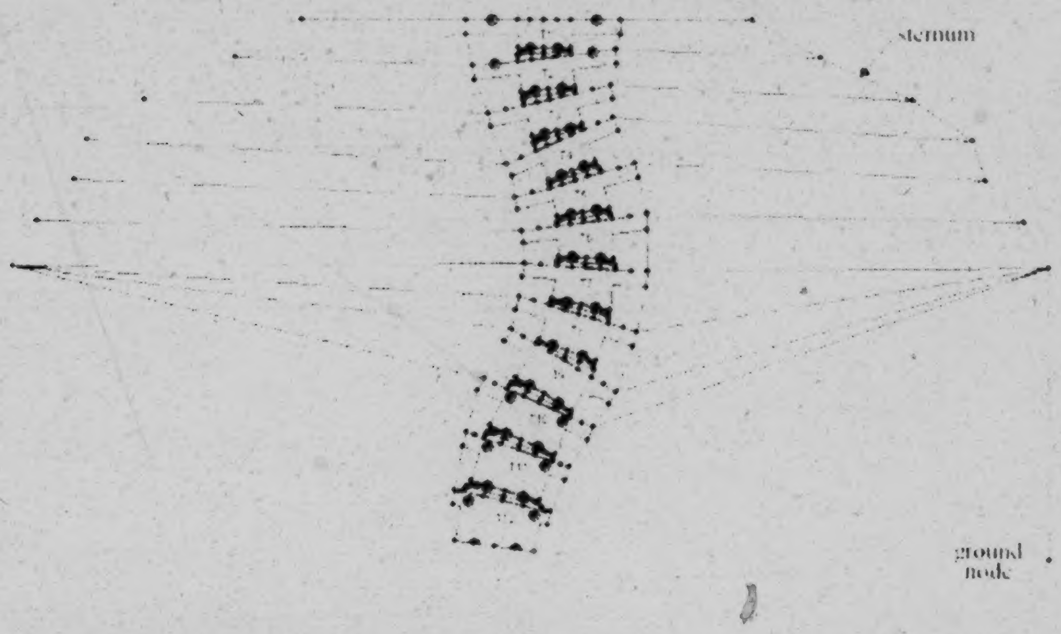

Figure 6.22: Thoracic model of the scoliotic spine. The thoracic cage is shown here comprised of 10 rib pairs and a sternum.

The length of the ribs were obtained using crude measurements from a normal thoracic model as measured from the midline. Note that the rib lengths are therefore shorter on the convex side of the curve to represent the rib hump present in most patients. The sternum was modeled using truss elements pinned to adjacent ribs. While these elements appear to be two-dimensional, only the y directional stiffness is accounted for as the sternum should not provide stiffness in the x direction.

Constraints, shown here as triangles, were placed on the sternum in the x-direction at each rib intersection, while constraint equations, not shown, were used to pin the end points of each rib pair together in the y-direction. Note that similar constraint equations could have been used for the x-direction, however, applying constraints is faster and more stable. The sternum was then constrained to a ground node via a two-dimensional truss element. This element represents other objects which would restrict the sternum from displacing vertically.

Again, patient specific material properties are not available, therefore, testing will be carried out to determine acceptable material property values.

6.3 Applying Boundary Conditions

Once the geometry has been created, the constraint application section is enabled as shown in Figure 6.23.

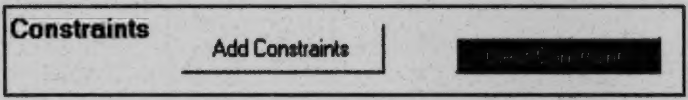

Figure 6.23: Constraint section of the graphical user interface.

As further testing is still required to determine the ideal boundary conditions, the user is prompted to select constraints for each spinal model. The options currently available to the user are constraining the top and/or bottom vertebra in the x and/or y direction or in rotation. The latter constraint is achieved through the use of constraint equations, specifically by setting the displacement in the x direction of the right hand node to be equal to the displacement in the x direction of left hand node.

For illustration purposes, constraints will be added to the previously created spinal geometry. First, click "Add Constraints" button. Pink lines will appear on the inferior surface of the bottom vertebra, and the superior surface of the top vertebra. The user is prompted, via the dialog box, to select one of the lines to apply constraints to. In this example, the bottom vertebra will be fixed in both the y direction. When the user clicks on the bottom pink line, a dialog box, shown in Figure 6.24 will appear.

The user must then select between UX, UY or RZ to apply x and y constraints or a rotation constraint, respectively. Once the user selects UY and clicks 'OK', the constraints will be added as shown in Figure 6.25. Additional boundary conditions can be added to the system by following the same steps.

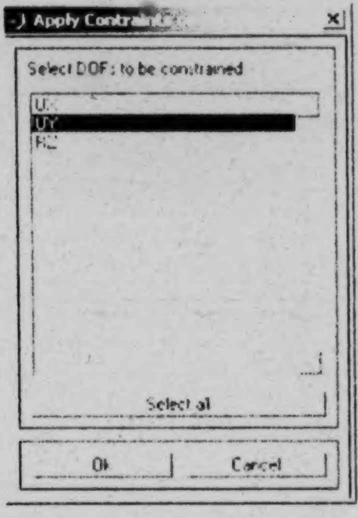

Figure 6.24: Dialog box prompting the user to select the degree of freedom to be constrained.

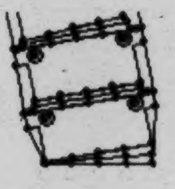

Figure 6.25: Depiction of y-direction constraints applied to the bottom vertebra.

If desired, the user can clear constraints using "Clear Constraints" button. A dialog box will appear to double check that you do want to clear all constraints.

6.4 Creating Loads

After the user has defined constraints, the load application section in the GUI will be enabled. Ultimately, this section will allow the surgeon to select the rod parameters in addition to which hook and screw locations to use and the chosen order of attachment. However, this section is currently limited to creating each load separately at the desired hook or screw location.

To illustrate this feature, the steps will be shown to add a load of 200 N to the left screw location on vertebra $L1$ at an angle of 45 degrees. The user will first press 'Create Load' Button. He will then be prompted to create load by clicking on one of the predefined hardpoints and, without releasing the mouse button, dragging the mouse in the direction of the desired load. Note that the program will automatically locate the nearest hardpoint to the location selected by the user. A pink line depicting the load will appear as the user drags the mouse. Once the user releases the mouse button, the pink line will remain and the load values will appear in the "Loads" window as shown in Figure 6.26.

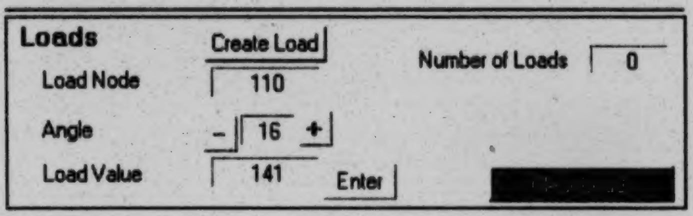
Loads
Load Node 110
Angle 16
Load Value 141
Number of Loads 0

Figure 6.26: Load application section withing the Control Window of the GUI. Loads must be applied one at a time.

The load parameters can then be edited to define the desired load. By changing the angle to 45 and the Load Value to 200, the pink line will change to display the new parameters. Once the user clicks 'Enter', the load will be created as shown in Figure 6.27 by a thicker pink line with an arrow and a force written in pink beside the line. The load parameters will then default back to allow the user to enter more loads if desired.

Due to the nature of the hook attachment on the transverse process, loads can only be applied in a perpendicular direction. Therefore, loads placed on hooks are

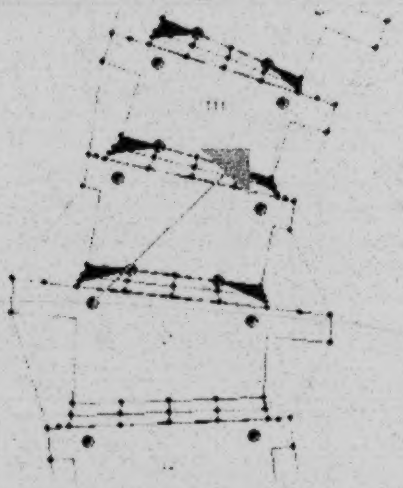

Figure 6.27: Graphical depiction of a 200 N load applied to the left screw of $L1$.

automatically re-orientated to reflect this. The angle text box is also made inactive so that this orientation can not be changed.

Should the user wish to change previously defined loads, the 'Clear Loads' button can be used to clear all loads.

6.5 Nonlinear Solver

Once loads have been added to the system, the Nonlinear Solver section is enabled. As stated previously, due to the many nonlinearities present in modeling scoliosis surgery, a nonlinear solver must be used. Currently, the user is able to define the number of load steps in addition to the maximum error and maximum number of iterations as shown in Figure 6.28. However, this is option should not be available once enough testing is performed to determine appropriate values for most cases.

The flowchart shown in Figure 6.29 outlines the basic procedure of the modified Newton-Raphson nonlinear solver.

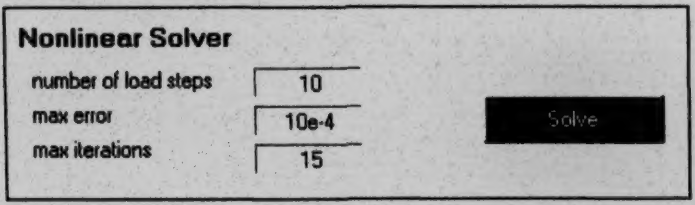

Nonlinear Solver

number of load steps 10

max error 10e-4

max iterations 15

Figure 6.28: Control section for the nonlinear solver. The user can change the default number of load steps, the maximum allowable error, and the maximum number of iterations.

6.6 Results

Once a solution is determined, the corrected spinal geometry is illustrated in the visual display window as shown in Figure 6.30.

The maximum displacement and corrected Cobb Angles are calculated and shown in the results section of the Control Window illustrated in Figure 6.31.

Other results are available and will be discussed in the following section.

6.7 Additional Features

Several additional features are available to aid in viewing the scoliotic geometry and evaluating the model. These features are described below.

6.7.1 Create ANSYS file

To facilitate validation tests with ANSYS, a function has been created to write ANSYS code for any test case. After defining the test run, select Menu Bar > File > Create ANSYS File as shown in Figure 6.32. A file, 'ANSYS.dat' is then created representing the current spinal model in the graphical user interface. Note that this file creates the nodes, elements, boundary conditions, and loading conditions, but does not account for condensation or any nonlinearities present in the model. The file will automatically open once it has been written.

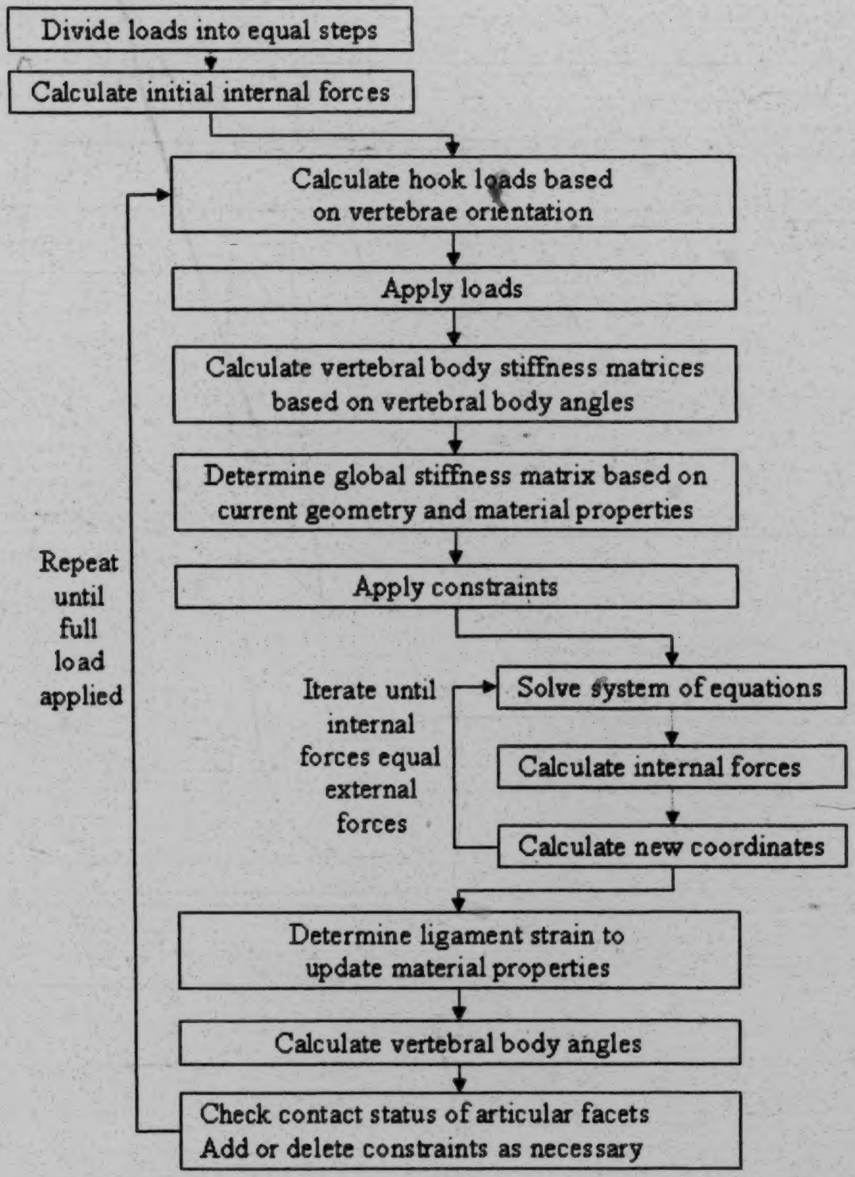
Divide loads into equal steps
Calculate initial internal forces
Calculate hook loads based on vertebrae orientation
Apply loads
Calculate vertebral body stiffness matrices based on vertebral body angles
Determine global stiffness matrix based on current geometry and material properties
Apply constraints
Repeat until full load applied
Iterate until internal forces equal external forces
Solve system of equations
Calculate internal forces
Calculate new coordinates
Determine ligament strain to update material properties
Calculate vertebral body angles
Check contact status of articular facets
Add or delete constraints as necessary

Figure 6.29: Flowchart illustrating the procedure for the nonlinear solver. Note that the dark grey boxes are part of the Newton-Raphson iteration, while the lighter grey boxes are indicate the steps within each load step.

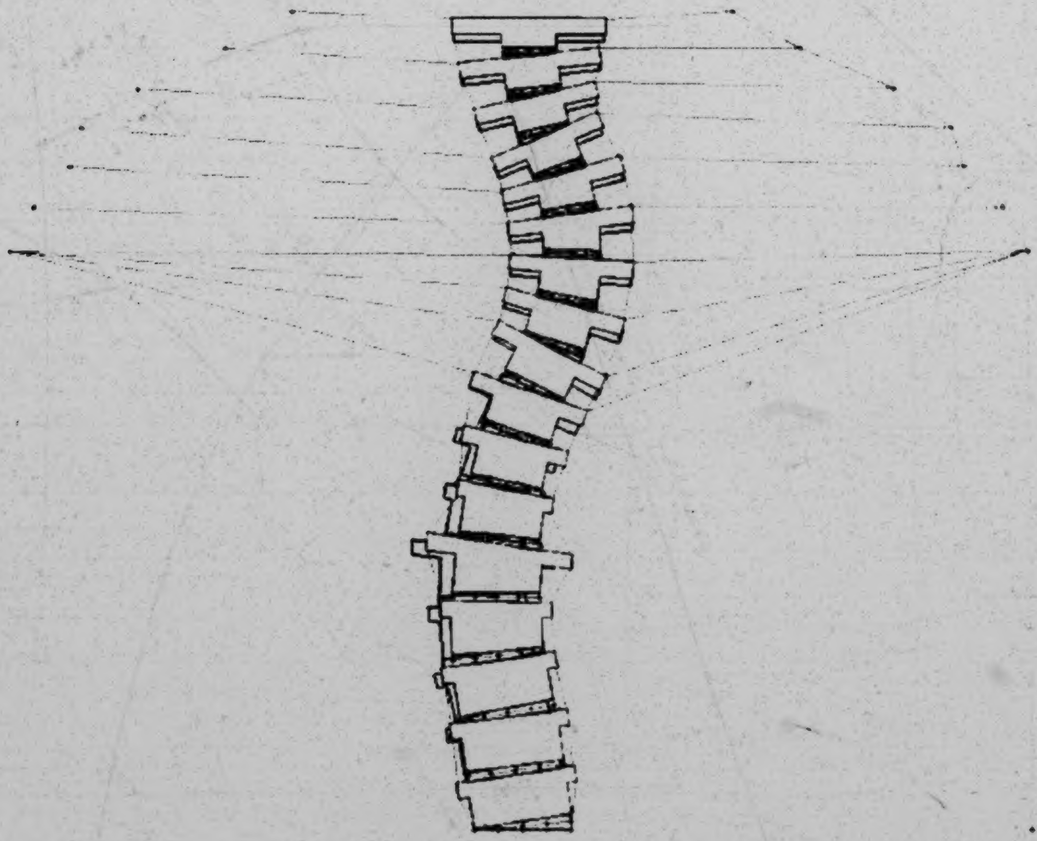

Figure 6.30: Visual display of the corrected scoliotic geometry. The dark grey vertebral bodies show the initial geometry.

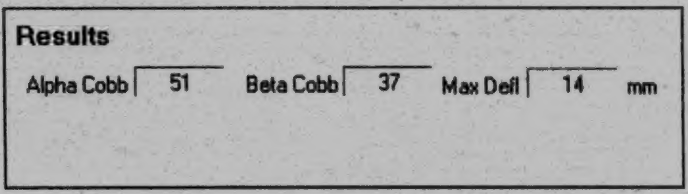

Results

Alpha Cobb 51 Beta Cobb 37 Max Defl 14 mm

Figure 6.31: Results section of the graphical user interface.

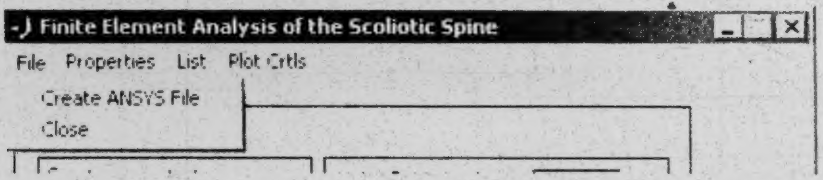
Finite Element Analysis of the Scoliotic Spine
File
Properties
List
Plot Crtls
Create ANSYS File
Close

Figure 6.32: File menu options available.

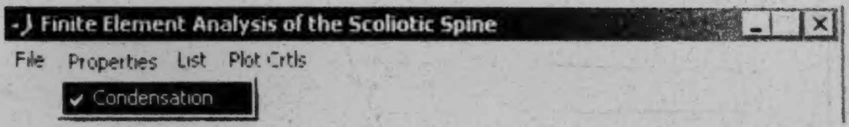
Finite Element Analysis of the Scoliotic Spine
File
Properties
List
Plot Crtls
✓ Condensation

Figure 6.33: Drop down menu selection to toggle condensation on and off.

6.7.2 Condensation Optional

The user is currently able to disable condensation of the vertebral body elements. This function is to enable testing to determine the computation times with and without condensation. Once the three-dimensional model has been created and tested, this option should be omitted. The user can turn this function on and off through the following menu options shown in Figure 6.33: Menu Bar > Properties > Condensation (checked = on).

Note that if condensation is on, each vertebral body will then be shown as one super-element as illustrated in Figure 6.34. Note that the hardpoints are not condensed as to permit loads to be applied.

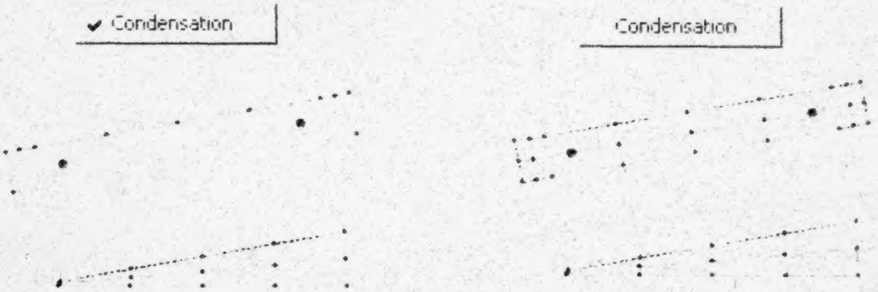

Figure 6.34: Illustration of the model with and without condensation used.

6.7.3 List Options

Several parameters of the model can be displayed in a file format through the List Menu as shown in Figure 6.35.

Loads

The loading conditions can be displayed as shown in Figure 6.36. The load number, node number to which the load is applied, value of the load, angle of rotation measured counterclockwise from horizontal and type of instrument bearing the load is shown. Note that for loads placed on hooks, the angle of rotation is the initial loading angle.

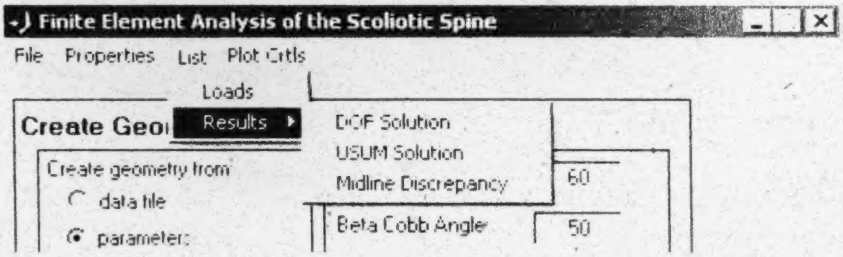
Finite Element Analysis of the Scoliotic Spine
File
Properties
List
Plot Crtls
Loads
Results
DOF Solution
USUM Solution
Midline Discrepancy
Create Geo
Create geometry from
data file
parameters
Beta Cobb Angle
60
50

Figure 6.35: List menu options.

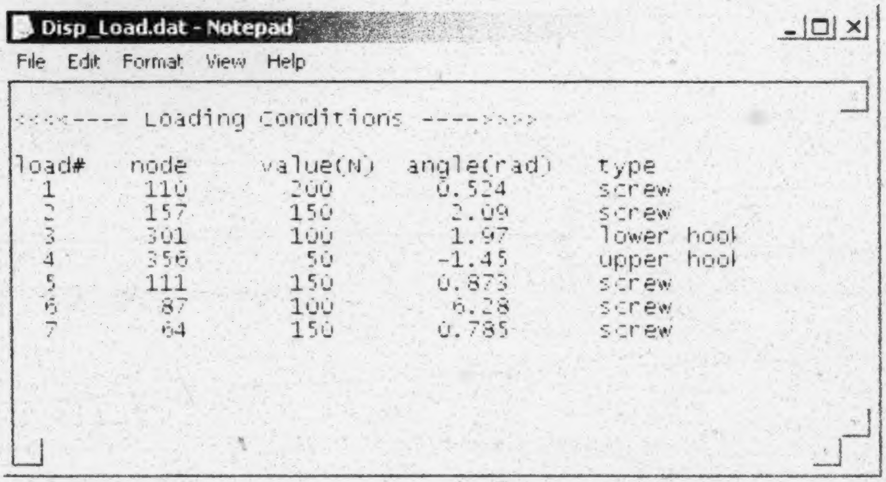
Disp_Load.dat - Notepad
File
Edit
Format
View
Help

```
<<<<---- Loading Conditions ---->>>>

load#   node      value(N)  angle(rad)    type
  1      110        200       0.524       screw
  2      157        150        2.09       screw
  3      301        100        1.97       lower hook
  4      356         50       -1.45       upper hook
  5      111        150       0.873       screw
  6       87        100        6.28       screw
  7       64        150       0.785       screw
```

Figure 6.36: Sample list of loading conditions.

Results

Various results can be listed to aid in clarifying the solution. These include the displacement at each degree of freedom (DOF) solution and the nodal sum (USUM) solution. The DOF solution is arranged in increasing nodal value, in the x direction, and y direction. For example, DOF solution 3 and 4 would be the x and y displacement respectively, for node 2. The USUM solution is arranged in ascending nodal value.

As shown in Figure 6.37, the midline discrepancy lists the x offset for each vertebra from the midline ($x = 0$). The offset is determined at the top and bottom of the vertebra, value for each vertebral body. Note that a positive value indicates an offset in the positive x direction.

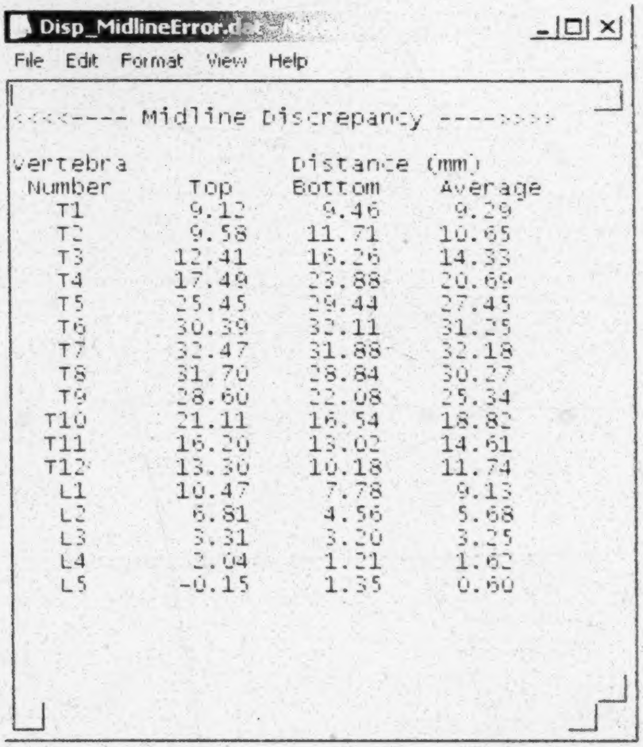

```
<<<<---- Midline Discrepancy ---->>>>

vertebra              Distance (mm)
 Number      Top      Bottom     Average
   T1        9.12       9.46       9.29
   T2        9.58      11.71      10.65
   T3       12.41      16.26      14.33
   T4       17.49      23.88      20.69
   T5       25.45      29.44      27.45
   T6       30.39      32.11      31.25
   T7       32.47      31.88      32.18
   T8       31.70      28.84      30.27
   T9       28.60      22.08      25.34
  T10       21.11      16.54      18.82
  T11       16.20      13.02      14.61
  T12       13.30      10.18      11.74
   L1       10.47       7.78       9.13
   L2        6.81       4.56       5.68
   L3        3.31       3.20       3.25
   L4        2.04       1.21       1.62
   L5       -0.15       1.35       0.60
```

Figure 6.37: Sample midline discrepancy results for a test run.

6.7.4 Display Options

Several display options are available to enhance clarity of the scoliotic geometry. These options are available by selecting Menu Bar > Plot Controls as shown in Figure 6.38, or alternatively by right clicking the mouse in the display menu. These options are discussed further below.

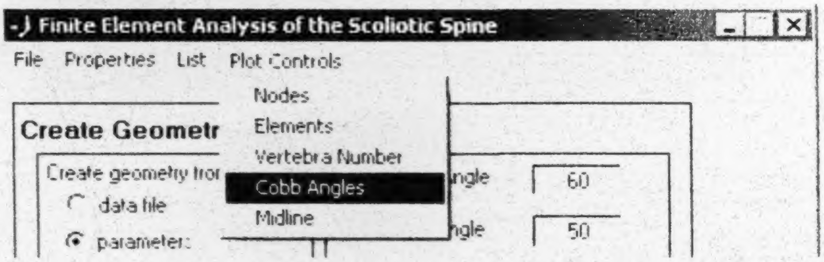
Finite Element Analysis of the Scoliotic Spine
File
Properties
List
Plot Controls
Nodes
Elements
Vertebra Number
Cobb Angles
Midline
Create Geometr
Create geometry fror
○ data file
● parameter:
ngle
60
ngle
50

Figure 6.38: Plot control options available. These options can also be accessed in the visual display window.

Node Numbers

The user can select to display the node numbers. This could be used to ensure that loads are being applied to the correct node for different trial runs. Note that, as shown in Figure 6.39, when condensation is used, the numbering reflects only the remaining nodes.

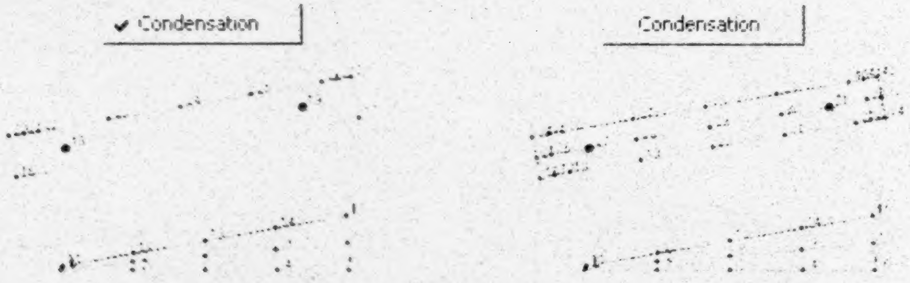
✔ Condensation
Condensation

Figure 6.39: Discretization of vertebral bodies with and without condensation.

Elements Numbers

Element numbers can also be displayed within the vertebral bodies and intervertebral discs as illustrated in Figure 6.40. Note that for visual clarity, the element numbers are not shown for other element types.

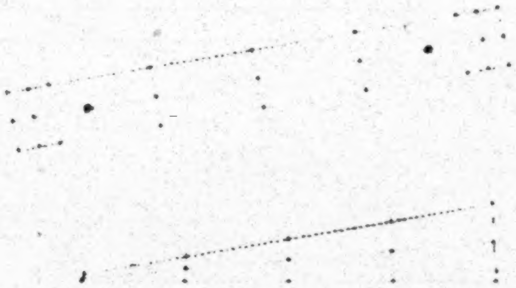

Figure 6.40: Display of element numbers for vertebrae and intervertebral disc elements.

Vertebrae numbers

The user may select to display vertebral body names to ensure proper load placement or enhance understanding of the geometry as shown in Figure 6.41.

Figure 6.41: Plotting control option to display the vertebra names.

Display Cobb Angles

The Cobb Angles can also be shown for geometry input using the scoliotic parameters as shown in Figure.6.42

Figure 6.42: Option to display α and β Cobb angles.

Midline

The midline ($x = 0$) can be displayed at any point in the analysis to enhance visualization of the scoliotic deformity, or the corrected spine. This is shown in Figure 6.43.

6.7.5 Print to Screen

The user can select to print the current geometry to an independent screen to save or print the model for comparison purposes. This also allows the user to use the

Figure 6.43: Display of the geometric midline ($x = 0$) to enhance visualization of the geometric deformity.

editing features to change figure properties, such as zoom. The user simply needs to press the Print to Screen button on the upper right corner of the visual display in the graphical user interface. Note that this feature can be used at anytime throughout the analysis.

Chapter 7

Results

Prior to developing a three-dimensional model, the two-dimensional model must first be verified. Analytical comparisons were performed to validate the program. A sensitivity analysis was then performed to determine the impact of Young's Modulus on several anatomical features in addition to the effect of contact elements. The real time capabilities of this model were assessed.

7.1 Linear Validation of the Model

To perform an initial verification of the model, a single motion unit without the intertransverse ligaments was analyzed. These tests were performed using vertebra $L5$, fixed at the base of the intervertebral disc with a lateral load of 100 N applied to the "screw" fixation point as shown in Figure 7.1.

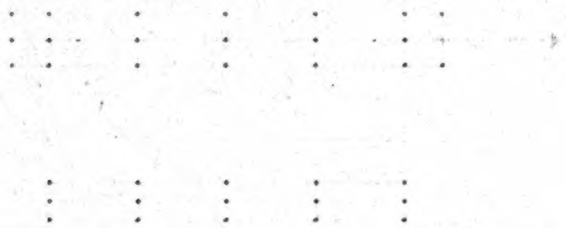

Figure 7.1: Validation test case on a single vertebral motion unit.

7.1.1 Hand Calculation

The single spinal unit was first compared to a cantilever beam with uniform material properties. However, due to the large depth to width ratio of this "beam", the transverse shear is large and the deflection due to shear could not be considered negligible. Therefore, the following equation for beams of relatively great depth[38] was used.

$$y = F\frac{P\ell}{AG} \tag{7.1}$$

where $F = \frac{6}{5}$ for a rectangular cross section and G is the modulus of rigidity. This equation assumes a homogeneous modulus of rigidity therefore, a constant modulus of elasticity, $E = 5.0\,\mathrm{MPa}$ was used for the entire motion unit. Using Equation 7.1 a theoretical deflection of 0.524 mm was calculated. The resulting deflection using femSpine and ANSYS was 0.544 mm, an error of only 4% from the theoretical value. This error was deemed acceptable.

7.1.2 ANSYS

The single motion unit model was then verified with ANSYS using the non-uniform vertebrae and intervertebral disc material properties. The resulting deflection, $y = 0.849\,\mathrm{mm}$, was found using both ANSYS and femSpine.

7.2 Nonlinear Validation of the Model

7.2.1 Test Case

A test case, shown in Figure 7.2, was created using the same geometry used to illustrate the model in previous chapter. This model shows an α Cobb Angle of $60\,^{\circ}$ from $T4$ to $T9$, a β Cobb Angle of $50\,^{\circ}$ from $T9$ to $L3$, a Lumbar Obliquity of $10\,^{\circ}$ and x and y constraints at $L5$.

Forces were then applied along the left side of the model to replicate the insertion of the correction rod during surgery. Peak forces measured in surgery are typically 145 N for the x directional screw (caudal-cranial direction, along the rod) and 195 N in the y direction[20]. Therefore, a load of 250 N, 40° counterclockwise from the horizontal, was applied to the screw hardpoint on the apex vertebra ($L1$) of the

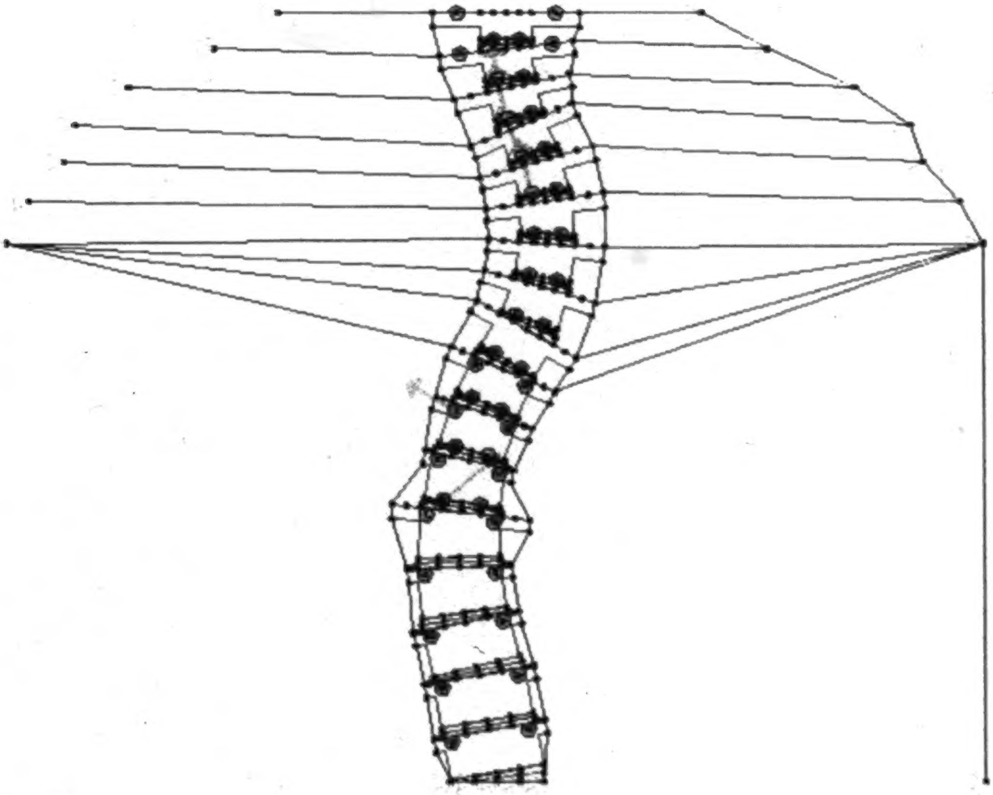

Figure 7.2: Illustration of the test case used for the sensitivity analysis.

lumbar curve. Several additional forces were applied along the left side of the model to optimize correction of the spine. The load values were varied in an attempt to obtain an overall spinal length correction of approximately 25 mm to reproduce results obtained by Papin, Labelle, Delorme, Aubin, deGuise and Dansereau[26]. In this study, the spinal height of 30 AIS patients was measured three days pre-operative and again two months post operative and an average increase in height of 25 mm was measured.

The chosen loading case for the test run is listed in Table 7.1. Six loads were applied to the left side of the spine, with two of those loads applied to screws and the remaining four loads applied to hooks. Recall that the loads applied to hooks are applied perpendicular to the surface of the vertebral body, therefore the angle shown in the table is the initial angle. After each load step, the angle is recalculated.

Table 7.1: Loading conditions for the sensitivity analysis

load #	**node #**	**condensed node #**	**value** (N)	**angle** (*rads*)	**type**
1	175	110	250	0.698	screw
2	249	179	150	2.618	screw
3	567	364	100	1.693	lower hook
4	530	343	150	1.798	lower hook
5	493	322	150	1.972	lower hook
6	456	301	150	1.798	lower hook

The resulting correction, shown in Figure 7.3, was measured as an α Cobb Angle correction of 16°, a β Cobb Angle correction of 17°, and an increase in spinal height of 26.4 mm. To further illustrate the resulting displacement of the spine, the deflection all of the center nodes of the vertebral body and intervertebral discs from $L5$ through $T1$ were plotted as shown in Figure 7.4. As expected, the x deflection of the lumbar spine is much greater than the x deflection of the thoracic spine. This is due to the added stiffness of the ribcage. The y deflection increases somewhat linearly from $L5$ to $L1$ with the majority of the deflection occurring within the intervertebral discs.

Note the highlighted nodes: 182, 412, and 634 in Figure 7.5. These nodes will be used to examine correction of the spine for differing material properties as they are located at peak displacement values.

7.2.2 Convergence Testing

As the finite element method is merely a numerical approximation, convergence testing must be carried out to ensure that the solution is valid. Due to the relatively low stiffness of the intervertebral discs, mesh refinement was primarily limited to the discs. For illustration purposes, the x and y deflections at nodes 182 and 634 respectively were noted for the differing mesh sizes of the test case as shown in Figure 7.6. As shown, the solution does converge by increasing the discretization of the model.

Due to the objectives of this project: to obtain a real time pre-surgical tool, the solver time and accuracy were both considered in selecting an appropriate mesh size.

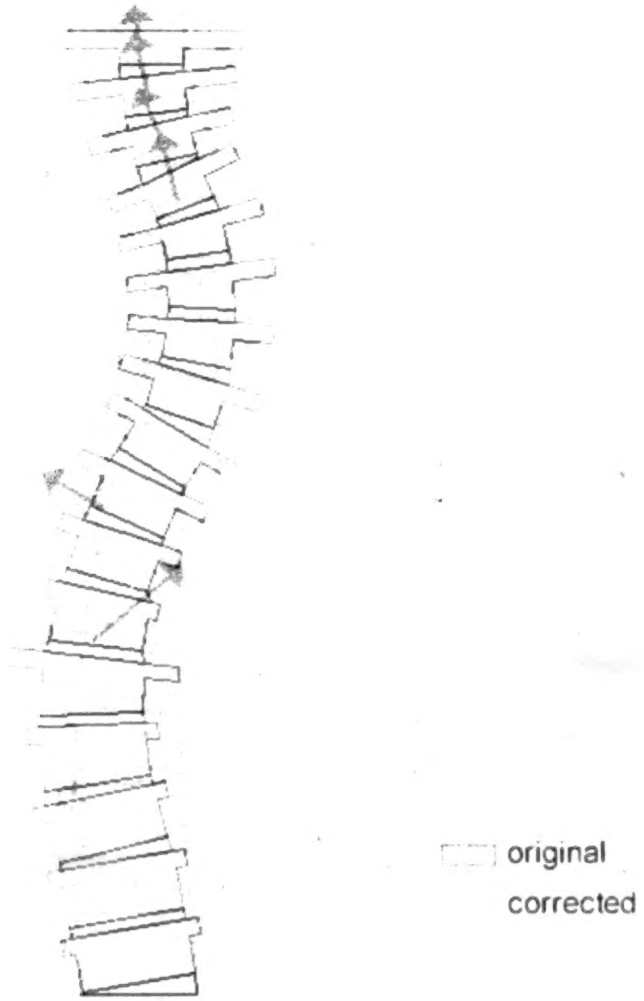
original
corrected

Figure 7.3: Resulting correction of the test case scoliotic spine. Note the original geometry in the background.

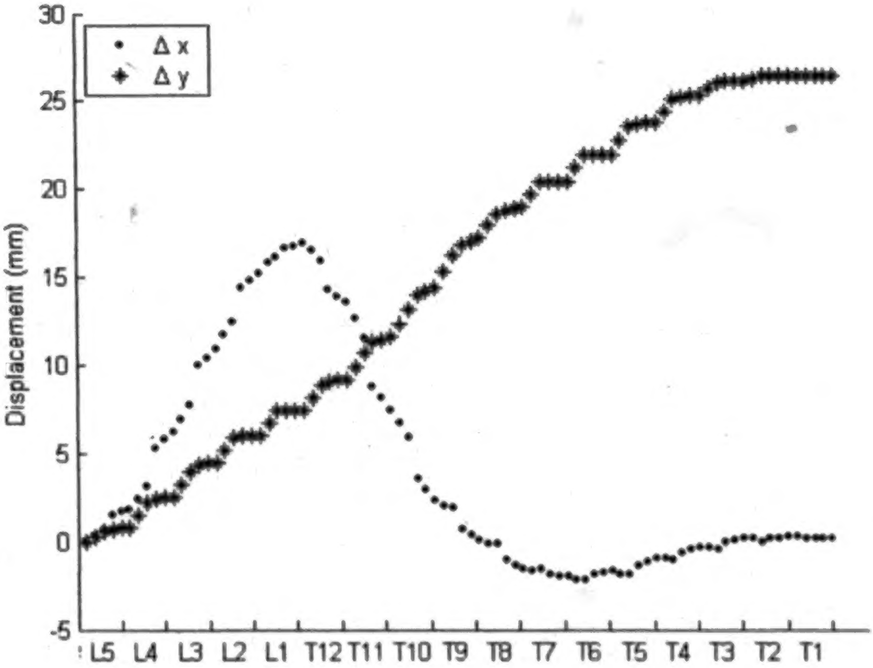

Figure 7.4: Displacement of the center nodes of the vertebral bodies and intervertebral discs using the original material properties.

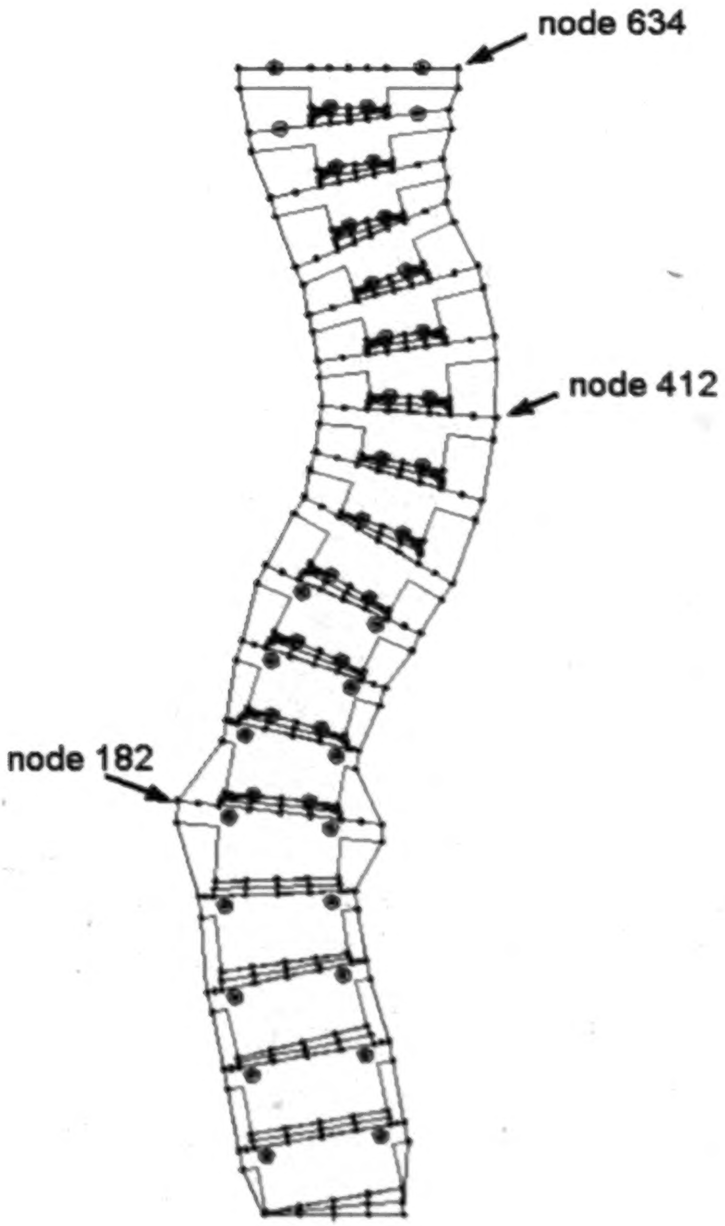
node 634
node 412
node 182

Figure 7.5: Locations of nodes 182, 412, and 634. The displacements of these nodes will be used to examine the effects of different parameters.

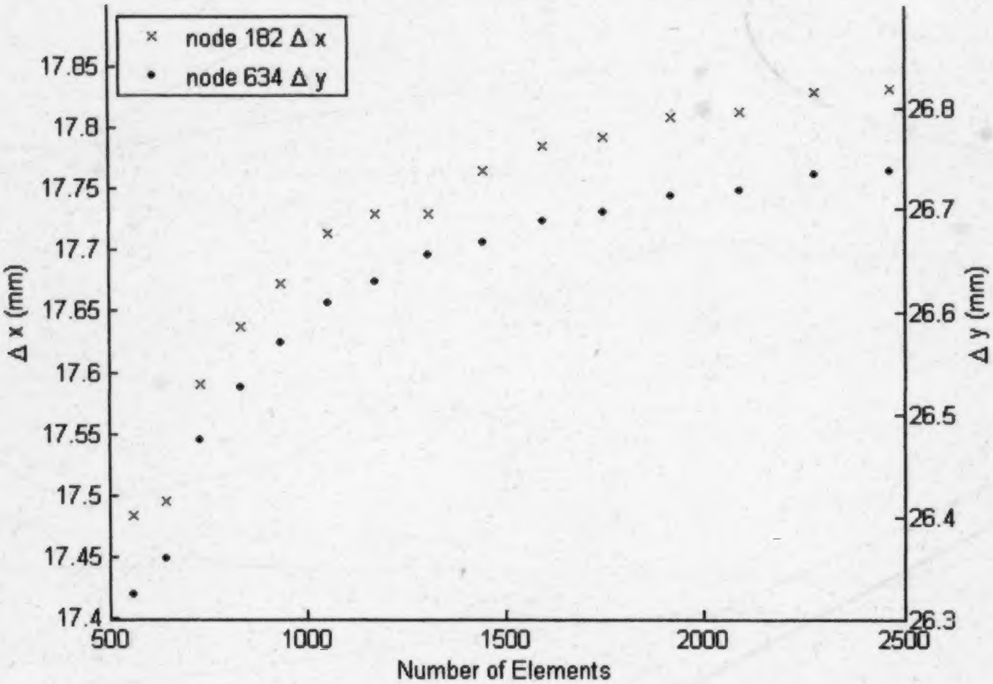

Figure 7.6: Convergence testing of the test model.

From the graph, the accuracy of the system is compromised only slightly, roughly 0.4 mm over the full range of the number of elements, while the time savings were significant, ranging from 10 seconds to 5 minutes. Therefore, a mesh size of 673 elements was selected to obtain a fast and sufficiently accurate solver.

7.2.3 Nonlinear Verification

A full nonlinear numerical validation of the model was desired, however, due to large differences between this femSpine and ANSYS, this was not feasible. These differences include:

- the inability to model ligaments with both nonlinear material properties and tension only elements in ANSYS.
- the inability to model contact elements in conjunction with nonlinear geometry using ANSYS.
- the inability to control the number of load steps using ANSYS. Note that ANSYS uses a more accurate approach, whereby the load steps are dynamically sized depending on the rate of change to the resulting solution.

However, the components were tested separately as discussed in the sections that follow.

Nonlinear Geometry

To test the large deflection capabilities of the femSpine solver, the solution from a modified version of the test case was compared with the results from ANSYS. The vertebrae that articulate with the ribcage ($T1$ through $T10$) were omitted from the modified test case to increase overall deflection of the model. The remaining nonlinear effects of the model were held constant: contact elements were eliminated and the modulus of elasticity of intertransverse ligaments was held constant at $E = 2.0$ MPa. The solution from both femSpine and ANSYS are illustrated in Figure 7.7. As shown, the solutions are similar, however the deflection of the intervertebral discs is larger in ANSYS. The maximum error was 6.9 mm or 17%, located near the applied load and the median error was 4.8 mm or 10%. The majority of this error is attributed assuming a linear strain-deflection relationship in the isoparametric elements used to model the intervertebral discs in femSpine, while ANSYS uses a nonlinear relationship. Additional error may also exist due to the different solvers used and different convergence tolerances.

For the purpose of this model, the error is deemed acceptable as the intervertebral discs will typically be exposed to somewhat smaller stresses compared to those present for this test case. This is due to the stiffness of the ribcage and the nonlinear stress-strain behavior of the ligaments not accounted for here.

For interest, the linear solution (from both ANSYS and femSpine) is illustrated in Figure 7.7 to stress the importance of using nonlinear geometry for the current application. Note that the volumes of vertebrae and intervertebral discs appear to increase using the linear solver. While the reason for this is unknown, this solution is not valid because the strains are too large, $\varepsilon > 0.04$, to be considered linear[3].

Nonlinear Material Properties

The nonlinear material properties were validated by following intertransverse ligaments #21, shown in Figure 7.8, and #11, shown in Figure 7.9, throughout the analysis.

Intertransverse ligament #21, was selected as it undergoes the largest strain throughout the test case. A plot of the strain, length and modulus of elasticity of this ligament is shown for each load step in Figure 7.10. The ligament begins in a state of prestress, with a strain of 10% and a length of 10.1 mm. In accordance with the stress-strain relationship shown in Figure 6.21, the modulus of elasticity is initially 2.0 MPa. After the second load step, the strain reaches 16%, and, as expected from the stress-strain relationship, the modulus of elasticity changes to $E = 12.7\,\text{MPa}$. Due to this increase in stiffness, the strain and change in length curves begin to flatten out. After the eighth load step, the strain crosses 30% and therefore the modulus of elasticity drops to $E = 1.5\,\text{MPa}$. Note that the strain curve does not appear to increase significantly with this change in stiffness. This is because the length of the ligament has been increasing, thus decreasing the overall stiffness of the element. In addition, the strain calculation is also using this new element length, again causing a reduction in the % strain.

Intertransverse ligament #11 was also selected for observation as it is subjected

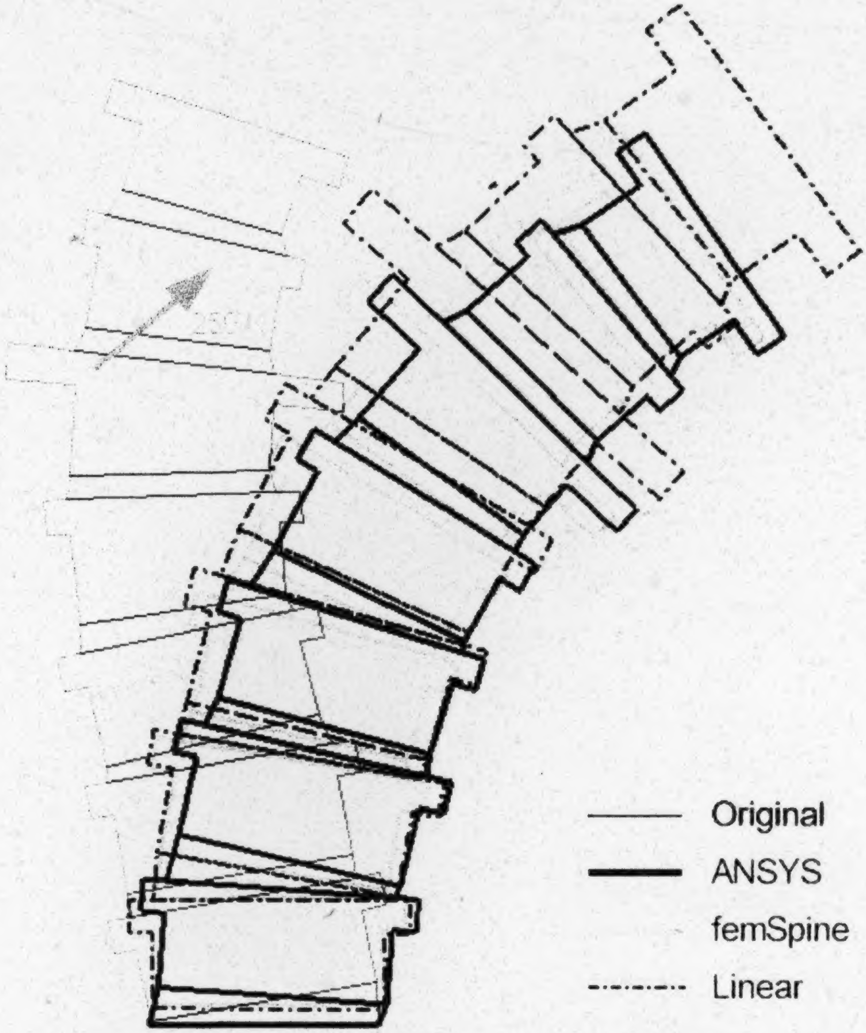
Original
ANSYS
femSpine
Linear

Figure 7.7: Verification testing comparing the results from ANSYS and femSpine. Note that the intertransverse ligaments were omitted from the figure for clarity.

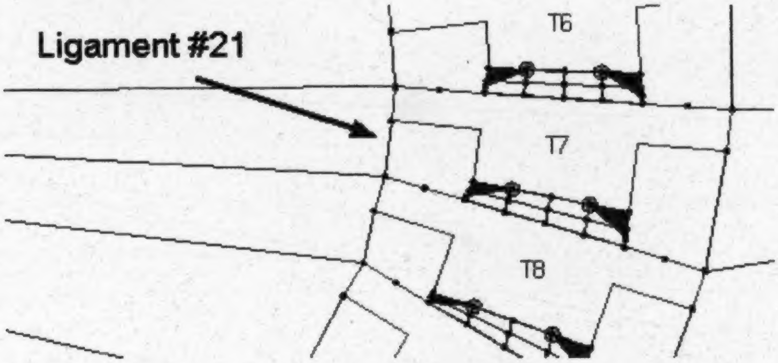
Ligament #21
T6
T7
T8

Figure 7.8: Location of intertransverse ligament #21. This ligament is subjected to the largest strain compared to the remaining 33 ligaments following the test run.

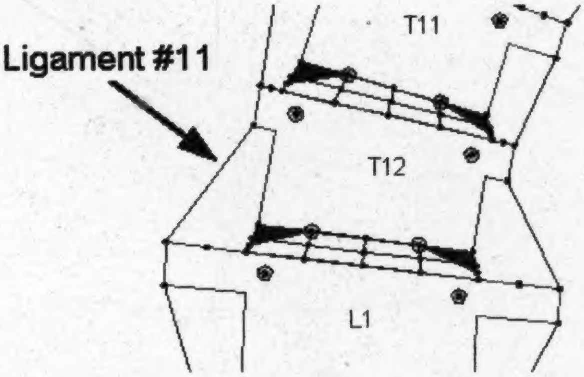
Ligament #11
T11
T12
L1

Figure 7.9: Location of intertransverse ligament #11. This ligament is subjected to the smallest strain compared to the remaining 33 ligaments following the test run.

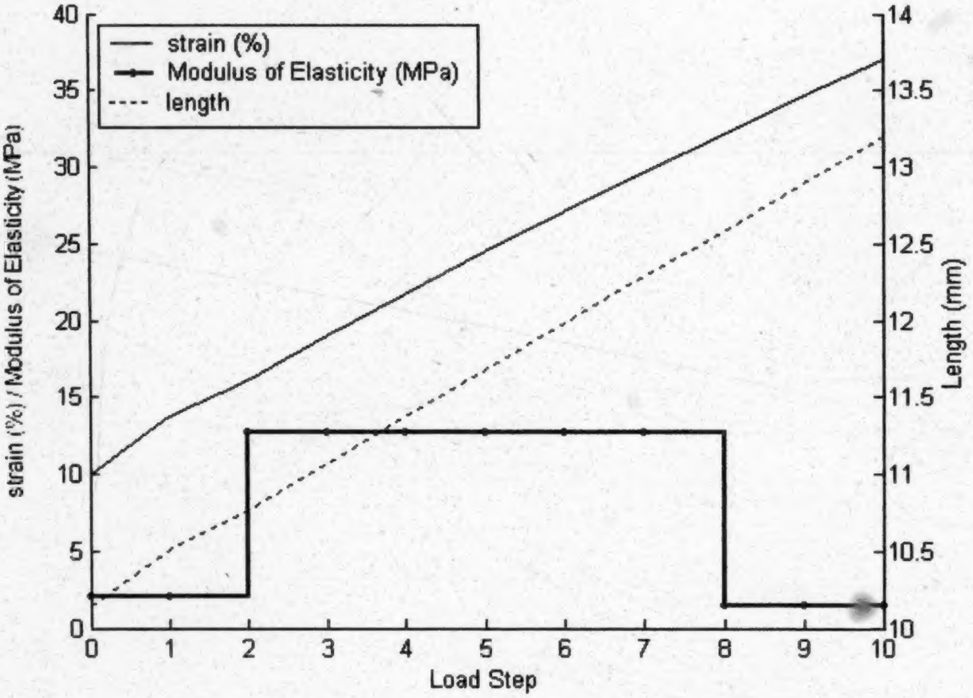

Figure 7.10: Change in strain, modulus of elasticity, and length of intertransverse ligament #21 following each load step of the test run.

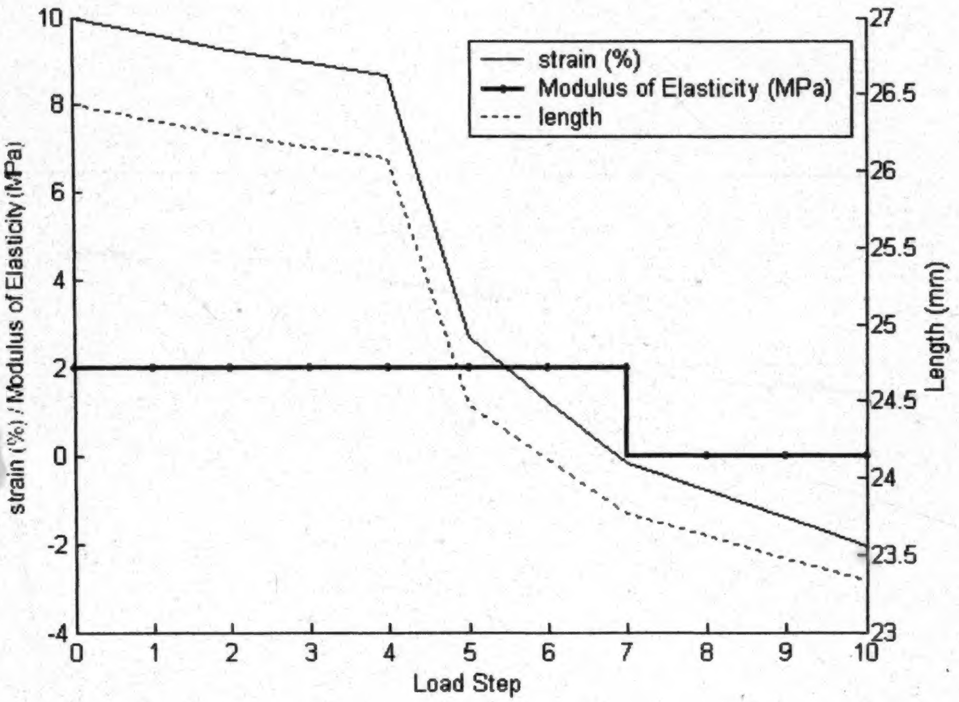

Figure 7.11: Change in strain, modulus of elasticity, and length of intertransverse ligament #11 following each load step of the test run.

to compressive loading throughout the test case. A plot of the strain, length and modulus of elasticity of this ligament is shown for each load step in Figure 7.11. Ligament #11 begins in a state of prestress, with a strain of 10% and an initial length of 26.4 mm. Again, due to the prestress, the modulus of elasticity is initially 2.0 MPa. After the seventh load step, the strain reaches −0.2%, and is therefore into the next stress-strain range. The modulus of elasticity changes accordingly to $E = 0\,\text{MPa}$. Due to this decrease in stiffness, the strain and length curves flatten out for the remaining load steps. Note that the discontinuities in strain and length over load steps five and six are attributed to other nonlinear influences.

From these example ligaments, one can conclude that the material nonlinearity of the ligaments is accounted for in the model.

Contact Elements

The contact between the articular facets was validated by examining the contact status of the three articular facet joints where contact occurs during the test case. Initially, the facet joints between vertebrae $T3$ - $T4$ and vertebrae $T8$ - $T9$ show in in Figure 7.12 are in contact.

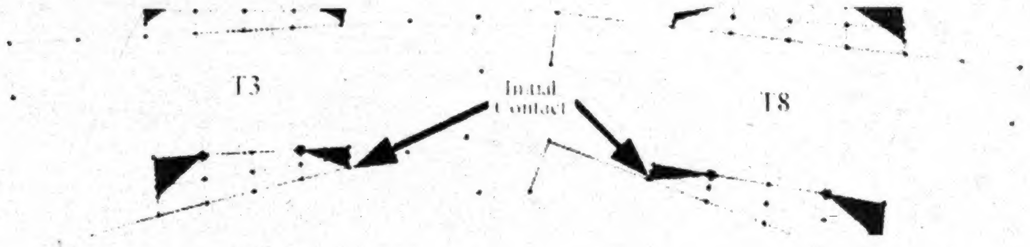

Figure 7.12: Initial articular facet contact locations. Note that the contact status of these locations changed after the first load step as the resulting internal forces were pulling the joint apart.

The internal forces acting on the facet joints are shown in Figure 7.13. As shown, after the first load step, a small force on the facet joint between vertebrae $T3$ - $T4$ indicates that the contact surface and node should remain in contact. The force vector was verified to ensure that it was perpendicular to the surface of vertebrae $T4$, to verify the constraint equations. The force gradually increases after the second

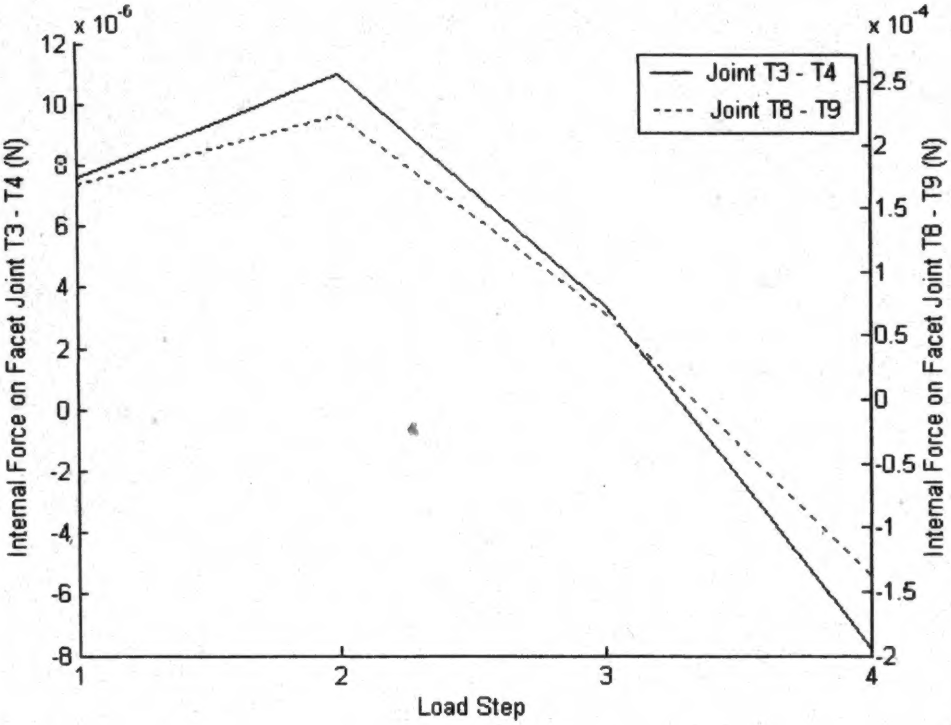

Figure 7.13: Internal forces on the articular facet joints between vertebrae $T3$ - $T4$ and vertebrae $T8$ - $T9$.

load step, but then decreases during the third load step until after load step four the interior force indicates the joint is pulling apart. The contact status report indicates that, as expected, the respective constraint equations were not applied for the remaining six load steps. Similarly, a small force on the facet joint between vertebrae $T8$ - $T9$ after the first load step dictates that the joint should remain in contact. The force increases to $7*10^{-4}$ N after the second load step but then decreases after the third load step. After the fourth load step the contact status was changed because the internal forces indicated that the joints were being pulled apart. As such, the respective constraint equations were not applied for load steps five through ten.

The third joint where articular facet contact occurs, is the left articular facet

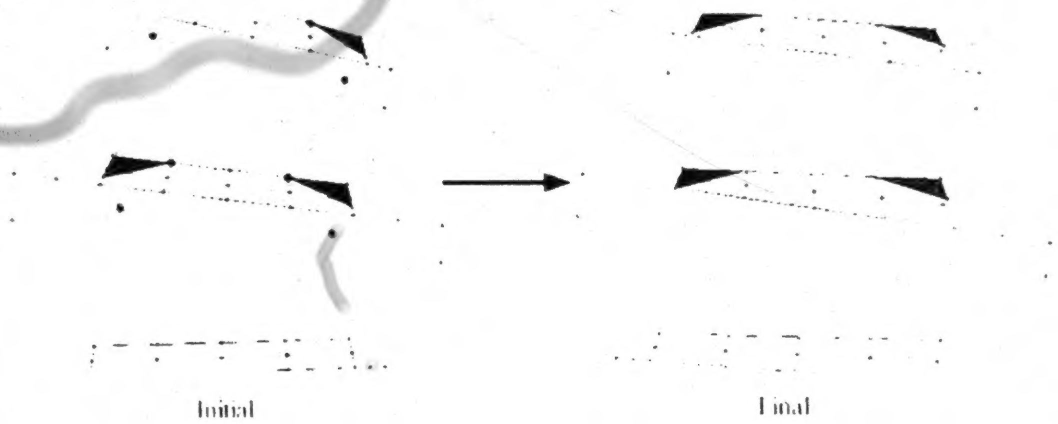

Figure 7.14: Illustration of the initial geometry and the final geometry of the articular facets between $T12$ and $L1$. Contact occurs following load step #7.

between vertebrae $T12$ and $L1$, illustrated in Figure 7.14.

The geometry of the joint was plotted after each load step, and contact was first observed following load step seven. Accordingly, the contact status of this joint was turned on at the same time. The constraints equations are applied in load step eight, and the resulting internal forces are plotted in Figure 7.15. The internal force vectors were, as expected, found to be oriented perpendicularly to the surface of vertebrae $L1$.

In agreement with the contact status report, contact was not observed at the remaining facet joints initially or following the analysis.

In conclusion, the code used to detect contact, to apply the constraint equations, and to remove contact, are all functioning properly.

7.3 Sensitivity Analysis

A comprehensive sensitivity analysis was performed to understand the effect of altering various properties including the material properties, contact elements, and the number of load steps.

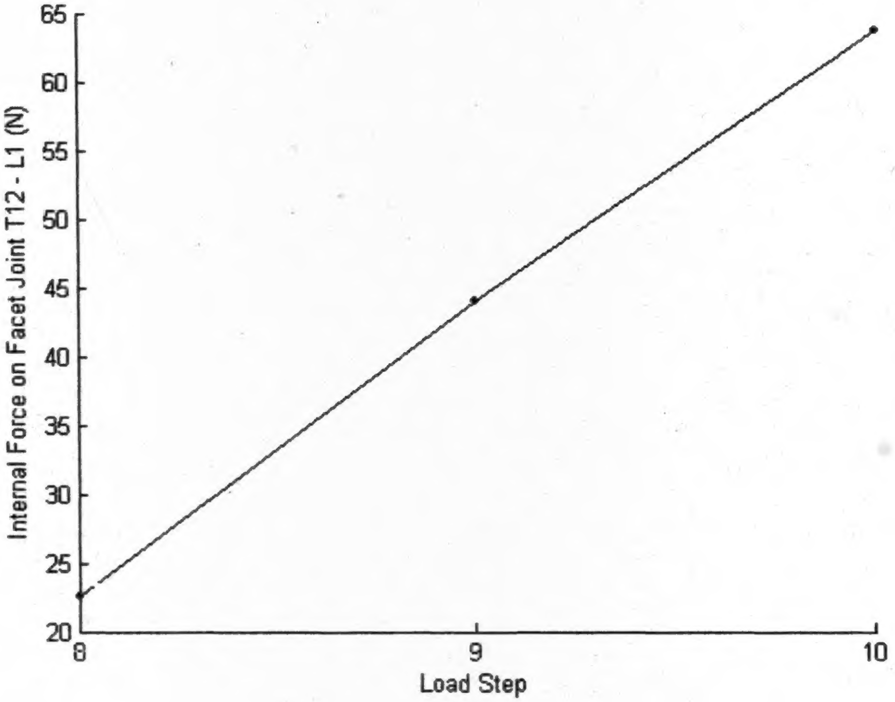

Figure 7.15: Internal force acting on the left articular facet joint between vertebrae $T12$ - $L1$ due to contact.

7.3.1 Material Properties

The starting material properties are shown in Table 7.2. These properties were primarily obtained from Skalli[29], but can be easily changed to accommodate other values.

Table 7.2: Original Material Properties

Vertebra	$E = 12000\,\text{MPa}$ $\nu = 0.3$ $t = 30\,\text{mm}$
Intervertebral Discs	$E = 2.0\,\text{MPa}$ $\nu = 0.41$ $t = 30\,\text{mm}$
Intertransverse ligaments	nonlinear, prestress = 10%
Sternum	$E = 12000\,\text{MPa}$ $A = 100\,\text{m}\,\text{m}^2$
sternum to ground	$E = 2.0\,\text{MPa}$ $A = 1.0\,\text{m}\,\text{m}^2$
Ribs (accounts for costal cartilage)	$E = 100\,\text{MPa}$ $A = 60\,\text{m}\,\text{m}^2$

Vertebrae

As discussed in Chapter 2, the interior of the vertebral bodies are made up of cancellous bone, while the exterior shell is made up of the harder cortical bone. The modulus of elasticity found in the literature is typically 100 MPa for cancellous bone and 12000 MPa for cortical bone. While these values differ tremendously, they are both much greater than the stiffnesses of the remaining components in the model. As an extreme test, these two stiffnesses were used to test the sensitivity of the system. As shown in Figure 7.16, the overall correction of the spine is similar, with only a small increase in correction of the spine using the smaller stiffness value.

To further illustrate the effect of changing the modulus of elasticity, E, of the vertebral bodies, the y displacement for node 634, and the x displacement for node 182, were plotted for values of E ranging from 50 MPa to 15000 MPa. As shown in Figure 7.17, the the change in correction is negligible for values of E above 1000 MPa. For vertebral body stiffnesses as low as $E = 100\,\text{MPa}$, the y displacement only increases by 4.1 mm (or 15%) while the x deflection increases by just 2.1 mm (or 12%) compared to the deflections at $E = 12000\,\text{MPa}$.

Overall, the modulus of elasticity of the vertebrae for this two-dimensional model was observed to be insignificant to the overall deflection. However, it has been suggested in a previous study that the vertebral stiffness is significant[2]. This may be because while the vertebral body is rigid in comparison with the other spinal

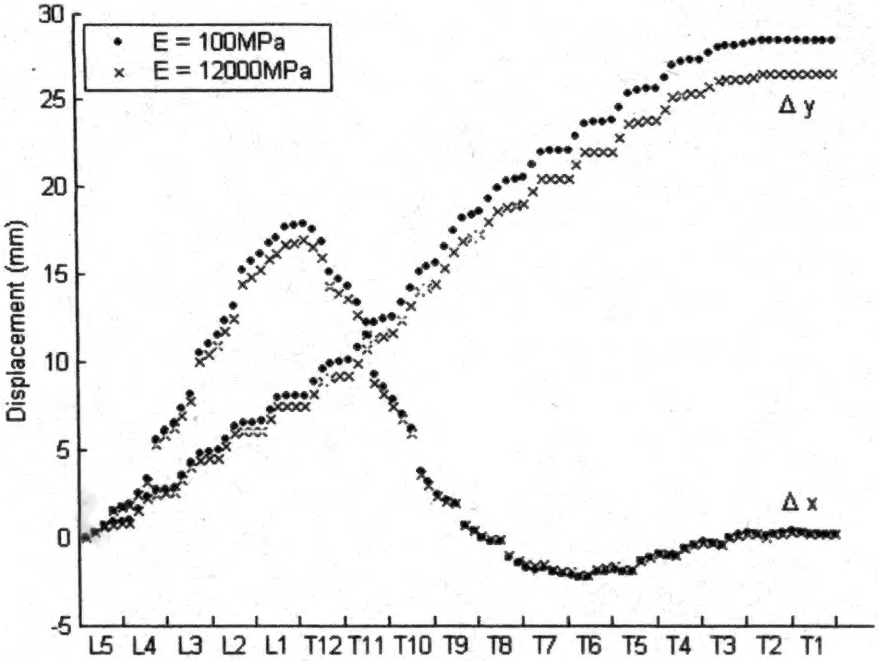

Figure 7.16: Resulting displacement of the spine using $E = 100\,\mathrm{MPa}$ and $E = 12000\,\mathrm{MPa}$ for the vertebral bodies.

components, the vertebral arch is more flexible. Since the vertebral arch is omitted from this two-dimensional model, the influence of the modulus of elasticity is unseen. Therefore, the significance should be verified again once the three-dimensional model is constructed.

Intervertebral Discs

To visualize the effect of changing the modulus of elasticity of the intervertebral discs, the x and y displacements of the centerline nodes from $L5$ to $T1$ are shown in Figures 7.18 and 7.19, respectively, for $E = 1$, 2, and $10\,\mathrm{MPa}$. As the disc becomes stiffer, the correction decreases significantly to $E = 10\,\mathrm{MPa}$ where the correction is almost negligible. Values in the literature are typically around the 2.0 MPa - 2.5 MPa range, however, Sundaram & Feng[32] reported a value of 10.3 MPa. From this two-

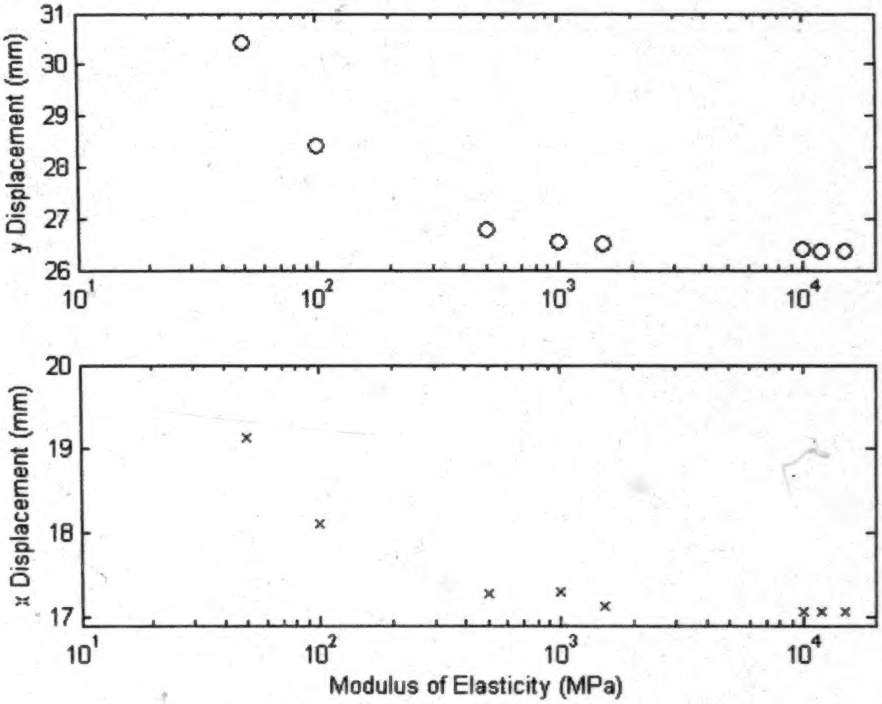

Figure 7.17: Deflection of nodes 634 (top graph) and 182 (bottom graph) using vertebral body stiffnesses ranging from $E = 50\,\text{MPa}$ to $E = 15000\,\text{MPa}$.

dimensional model, this value does not seem plausible given the force data obtained in surgery and the typical surgical correction.

To further understand the significance of the modulus of elasticity of the intervertebral discs, the y deflection of node 634 and the x deflection of node 182 was plotted for values of E ranging from 1 MPa to 10 MPa. As shown in Figure 7.20 for larger values of Young's Modulus (i.e. $E > 4\,\text{MPa}$) the model was only marginally sensitive, however, at lower values of E the spinal correction was observed to be highly sensitive Clearly, it is crucial that the stiffness properties of the intervertebral discs be known for each patient for pre-operative testing to be viable.

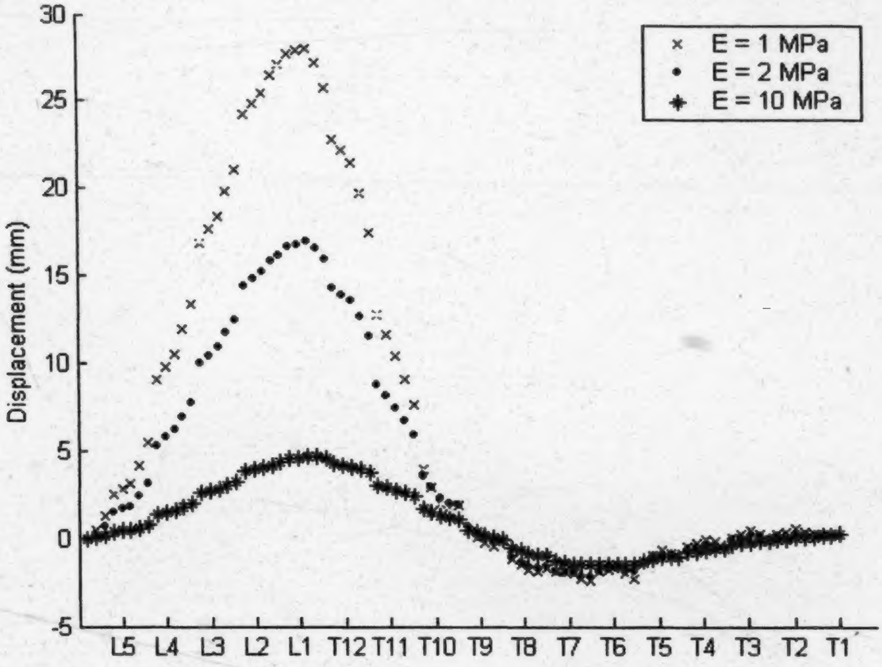

Figure 7.18: x deflection of the centerline nodes of the spine using a varying modulus of elasticity for the intervertebral discs.

Intertransverse Ligaments

Due to the nonlinear nature of the intertransverse ligaments, several tests were required to determine necessity of the nonlinear assumptions in addition to the sensitivity of the chosen material properties.

The first question regarding the intertransverse ligaments was whether the deflection was large enough to necessitate the use of the nonlinear strain equation. Typically, for changes in strain above 10%, the nonlinear element should be used. A histogram depicting the change in strain for the 34 intertransverse ligaments was created as shown in Figure 7.21. Nine of the ligaments are into the nonlinear strain range, therefore, the nonlinear strain should be accounted for.

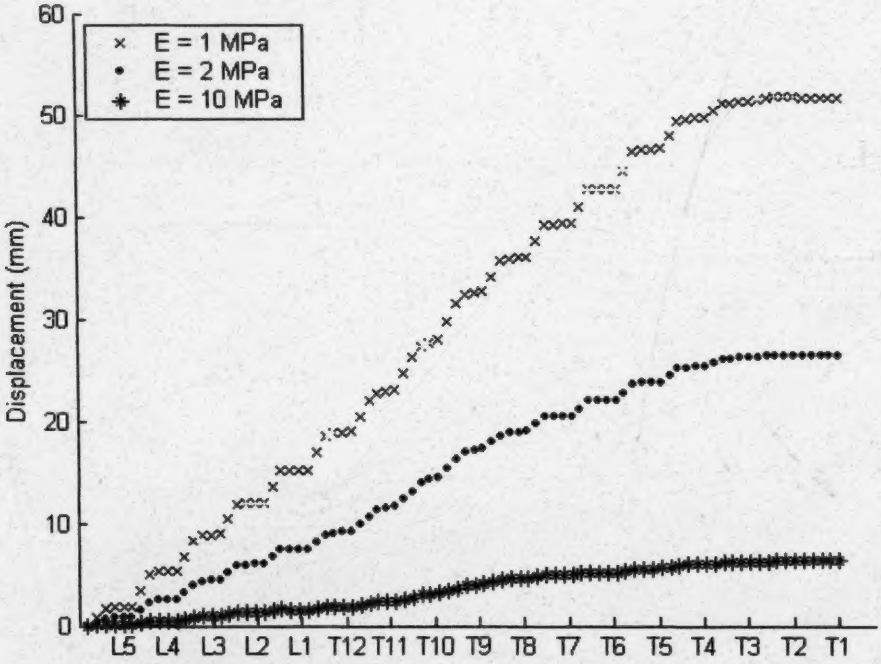

Figure 7.19: y deflection of the centerline nodes of the spine using a varying modulus of elasticity for the intervertebral discs.

Comparing the results for the nonlinear strain/nonlinear material property truss element and the elastic nonlinear material property truss element, the change in deflection of the spine was minimal as shown in Figure 7.22. The maximum change in element strain was a 4% increase with a median change of 0.2% and a mean change of 0.8%. While this is considered a negligible change, the computational time was unchanged. Therefore, the ligaments are currently modeled using the nonlinear strain/nonlinear material property truss element. Note that, as expected, the peak changes occur near the ligaments which undergo the largest strain during the correction.

Going back to Figure 7.21, eight of the 34 ligaments are in the negative strain region, meaning that the modulus of elasticity for these ligaments is 0 MPa. It is

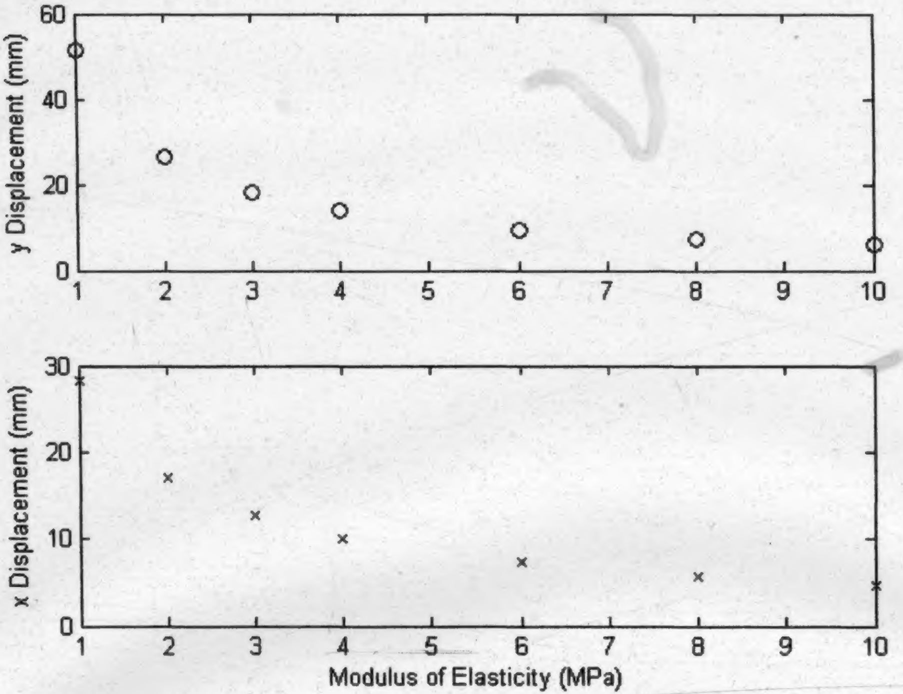

Figure 7.20: Deflection of nodes 634 (top graph) and 182 (bottom graph) using intervertebral disc stiffnesses ranging from $E = 1\,\text{MPa}$ to $E = 10\,\text{MPa}$.

therefore also important that we include the negative strain material properties for ligaments.

To understand the importance of the multilinear material properties, the test case was run again where the modulus of elasticity for ligament #21, shown in Figure 7.8 was maintained at $E = 2.0\,\text{MPa}$. A negligible change in the spinal geometry was observed, with only a 0.1 mm increase in the final length of the ligament. It can therefore be concluded that the effect of the material nonlinearities for the ligaments are negligible. However, further testing should be executed for all of the spinal ligaments once the three-dimensional model is constructed.

The next step in the analysis of the intertransverse ligaments was to examine the effect of using an initial prestress. As shown in Figure 7.23, the difference between

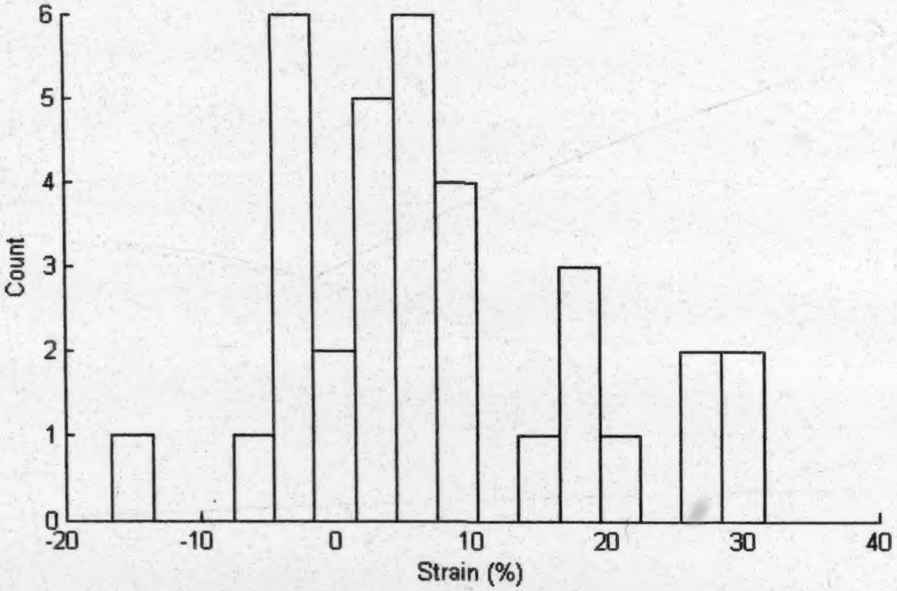

Figure 7.21: Histogram illustrating the final change in strain of the intertransverse ligaments using the test run.

a prestress of 10% and no prestress, is not large, with a maximum increase in spinal displacement of 0.11 mm for the test case without prestress.

Finally, the effect of the stiffness of the intertransverse ligaments should be examined. The literature contains a large range of material property values for ligaments, it is therefore difficult to determine a suitable range over which to vary the stiffness. Therefore, as shown in Figure 7.24, test cases were performed for $E = 10E_{orig}$ and $E = \frac{E_{orig}}{10}$. Note that the shape of the stress-strain graph was kept constant. As expected, the overall shape of the spinal correction remains the same with an increase in spinal flexibility as the stiffness of the intertransverse ligaments is reduced.

The effect of the ligament stiffness was also observed for a range of ligament stiffnesses, from $\frac{E}{10}$ to $10E$ as shown in Figure 7.25. The y displacement remains about the same for smaller stiffnesses, but drops off relatively quickly for larger ligament stiffnesses. Note that the overall change in displacement is small, resulting in less than a 1% change in deflection in either x or y, with a tenfold increase or decrease in

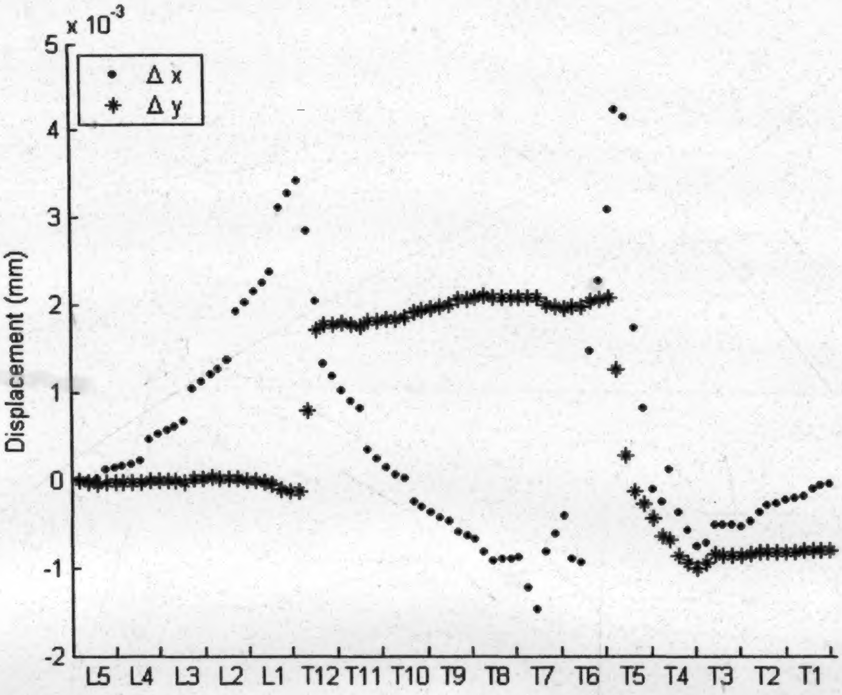

Figure 7.22: Change in displacement of the centerline nodes of the spine due to using the nonlinear strain-displacement truss element to model the intertransverse ligaments instead of the linear strain-displacement truss element.

ligament stiffness.

In conclusion, the intertransverse ligaments do not have a significant effect on the spinal correction. However, it is anticipated that other spinal ligaments which cannot be included in this two-dimensional model will have greater effects.

Thoracic Cage

A sensitivity analysis was then completed for the simplified thoracic cage. The sensitivity of the ribs and the sternum were examined separately.

Since the ribs are primarily composed of cortical bone, the upper testing range

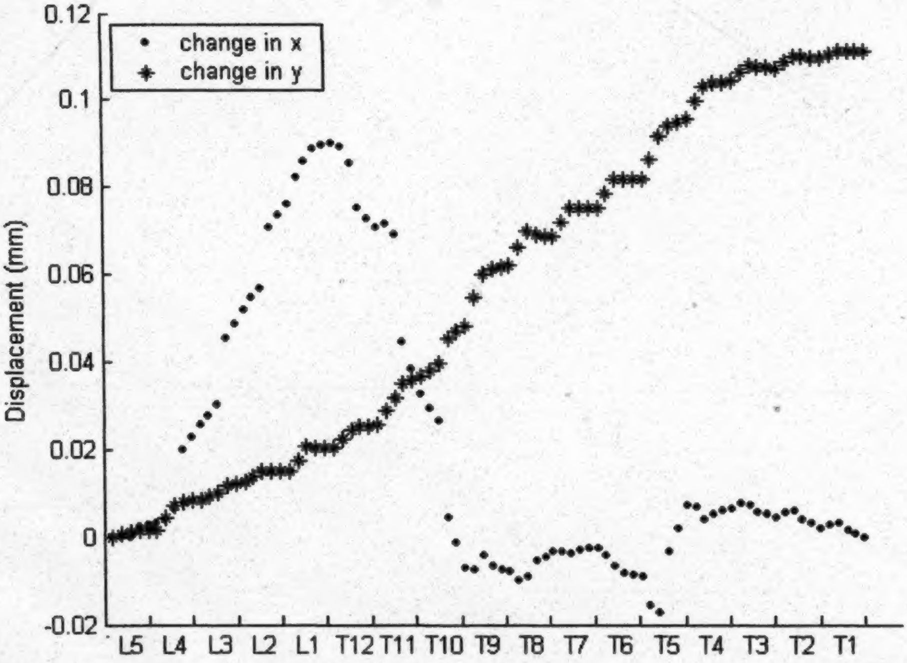

Figure 7.23: Effect of prestress on the spinal deflection. Note that a positive change in displacement indicates a larger deflection for the test case without prestress.

was set at $E = 12000$ MPa. However, since the ribs attach to the sternum with costal cartilage, for which a value of $E = 275$ MPa[35] has been previously used, the overall stiffness should be somewhere between the two values. However, because this model does not account for the three-dimensional geometry of the ribcage, an even lower modulus of elasticity was used, with the original value set at $E = 100$ MPa. Figure 7.26 illustrates the effect of the ribs on the spinal correction. As would be expected, as the stiffness of the ribcage is increased, the spinal correction decreases. Even for values as low as $E = 100$ MPa, the correction of the thoracic spine is relatively small. The correction of the lumbar spine also decreases as the stiffness of the thoracic cage increases. This is because the top two vertebrae making up the beta curve are $T9$ and $T10$, which articulate with the thoracic cage. As expected, the y deflection

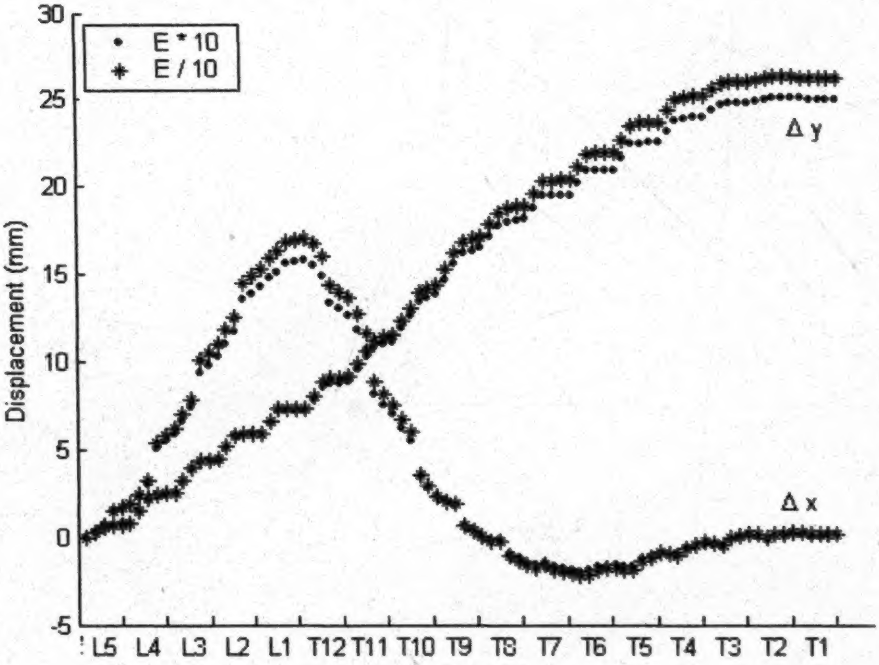

Figure 7.24: Resulting displacement of the spine for different values of the modulus of elasticity for the intertransverse ligaments.

decreases as a result of the increased stiffness in the x direction.

A closer look at the resulting y deflection of node 634, and the resulting x deflections of nodes 182 and 412 is shown in Figure 7.27. The y displacement decreases logarithmically as the stiffness increases except for modulus of elasticity values below 25 MPa. Below this value, the applied forces are causing the spine to overcorrect, resulting in a decrease in the maximum y displacement. As mentioned in the previous paragraph, the x directional correction of the lumbar curve decreases with increased stiffness of the ribs. This change is quite large, a 7 mm change over the full range of stiffness values. The x directional correction of the thoracic curve is directly compromised by an increase in rib stiffness, though the range is much less sensitive above $E = 100\,\mathrm{MPa}$.

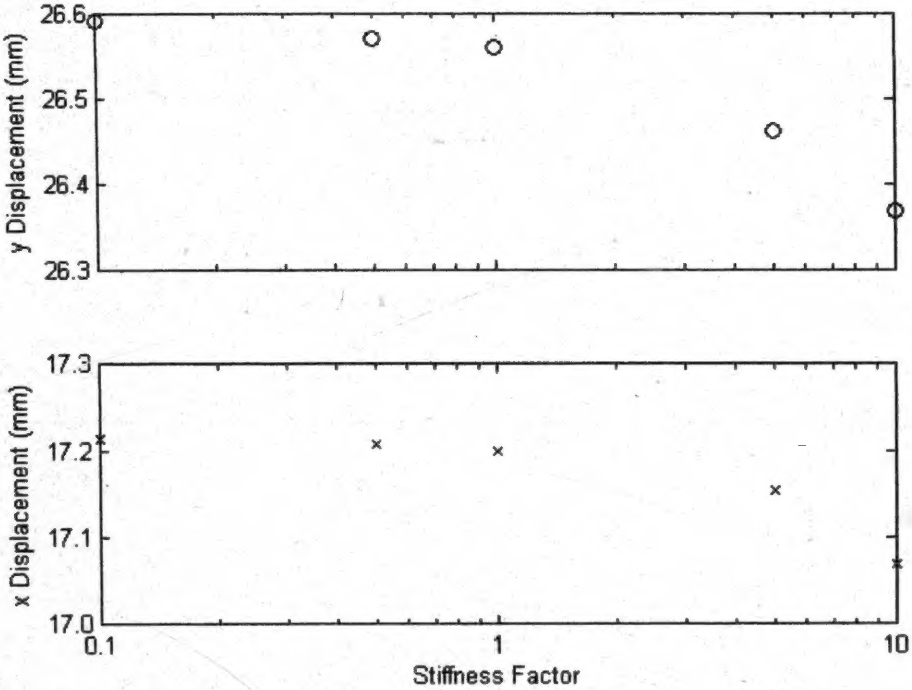

Figure 7.25: Deflection of nodes 634 (top graph) and 182 (bottom graph) with varying stiffnesses of the intertransverse ligaments.

Clearly, the stiffness of the ribs does play a role in the spinal correction. However, the three-dimensional model will allow the costal cartilage to be modeled separately, and the true rib shape to be modeled. This may decrease the sensitivity of the deflection on the rib stiffness.

The effect of altering the stiffness of the sternum was then considered. However, because the ribs are modeled as truss elements, perpendicular forces do not pass through them. Therefore, due to the orientation of the rib elements, minimal y directional forces are placed on the sternum. As a result there is minimal change to the solution due to variations in the stiffness of the sternum. Ideally, the ribs should be modeled as beam elements since they are able to resist bending moments in addition to axial and shear forces. As such, they would transfer bending and shear loads to the sternum. However, the articulations between the ribs and vertebrae

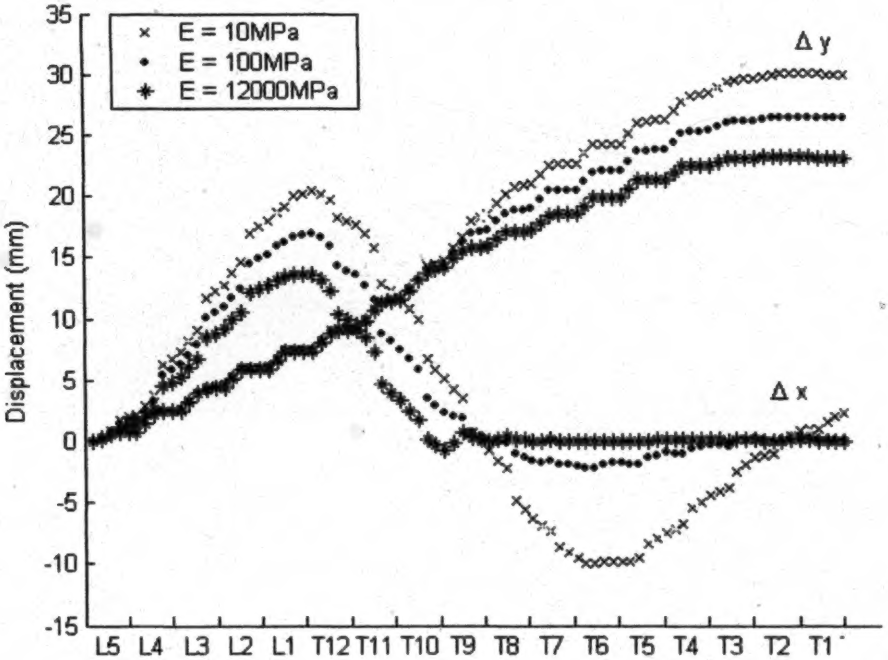

Figure 7.26: Resulting displacement of the spine using $E = 10\,\text{MPa}$, $E = 100\,\text{MPa}$, and $E = 12000\,\text{MPa}$ for the ribs.

are such that minimal bending and shear loads would transfer into the sternum. Therefore, the stiffness of the sternum should not have a substantial effect on the spinal correction.

Sternum to "Ground" Stiffness

The effect of changing the stiffness of the element attaching the sternum to a grounding point was also examined. This element takes into account the stiffness added to the model from all remaining components such as the muscle and skin. Note that the stiffness value is purely experimental and as such a wide variety of values were tested. As shown in Figure 7.28, the shape of the spinal correction is similar regardless of the stiffness of the ground element.

As shown in Figure 7.29, a minimal change for both the x and y deflection was noted using modulus of elasticity values less than 100 MPa. Even for values over 100 MPa the change in displacement is minimal. Therefore, it can be concluded that the value of this experimental stiffness is not significant to the resulting correction of the spine.

7.3.2 Facet Contact Elements

The overall effect of the articular facets was examined by comparing the displacements of the centerline nodes for the test case with and without contact elements as shown in Figure 7.30. The largest change occurs at the $L1$ to $T12$ junction, with an decrease in y of 0.05 mm and a peak change in x of 0.49 mm without contact. From the contact element validation discussed in Section 7.2.3, the contact status for this joint indicates that the left side, shown in Figure 7.14, came into contact after the seventh load step and remained in contact throughout the remaining three load steps. The internal force due to the constraint application after the last load step was 63 N, $\measuredangle 82°$.

Recall that the contact status report also indicated that the facet joints between Vertebrae $T3$ - $T4$ and vertebrae $T8$ - $T9$ shown in Figure 7.12 started in contact. As the internal forces were very small, no noticeable effect of this was noted in Figure 7.30.

After reviewing these results, the impact of the contact elements are minimal. However, using patient specific geometry in addition to the full three-dimensional model which will account for additional contact locations in the lumbar spine, may increase the influence of the facets on the spinal correction.

7.3.3 Load steps

For nonlinear models, the more load steps used in the analysis, the higher the accuracy of the system. However, the cost of obtaining a high accuracy comes with increased computational time requirements. A sensitivity analysis was performed to determine the number of load steps required to achieve a satisfactory accuracy level. Figure 7.31 illustrates the displacement of the spine for 1 load step, which is essentially linear, and 100 load steps. As expected, a large discrepancy between the two test runs exists. The linear model omits all of the nonlinear components: contact elements, the

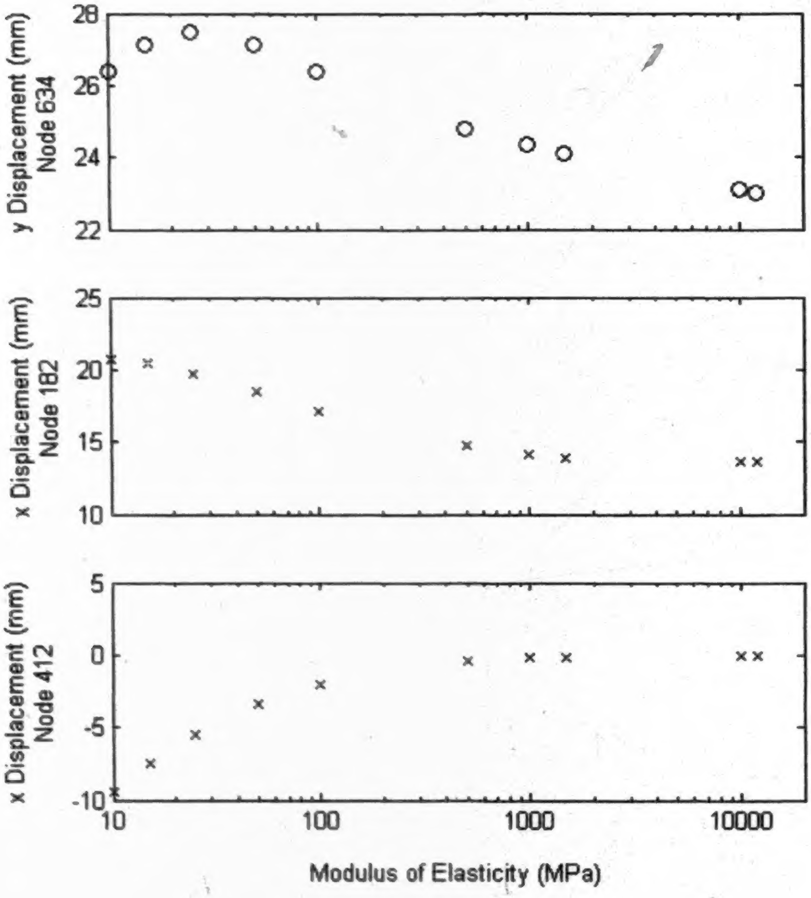

Figure 7.27: Deflection of nodes 634 (top graph), 412 (middle graph) and 182 (bottom graph) using rib stiffnesses ranging from $E = 10\,\text{MPa}$ to $E = 12000\,\text{MPa}$.

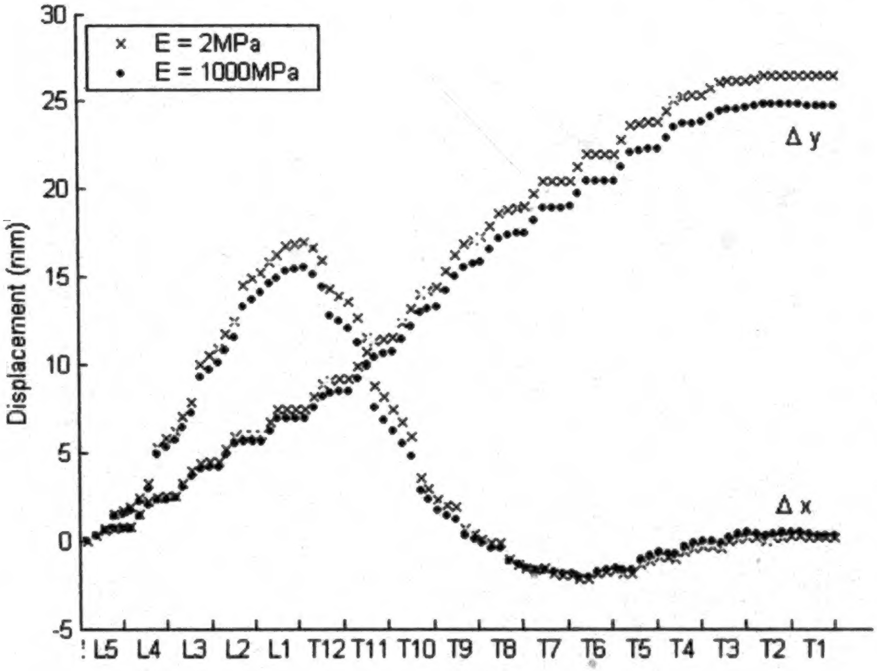

Figure 7.28: Resulting displacement of the spine using $E = 2\,\text{MPa}$ and $E = 1000\,\text{MPa}$ for the sternum to ground truss element.

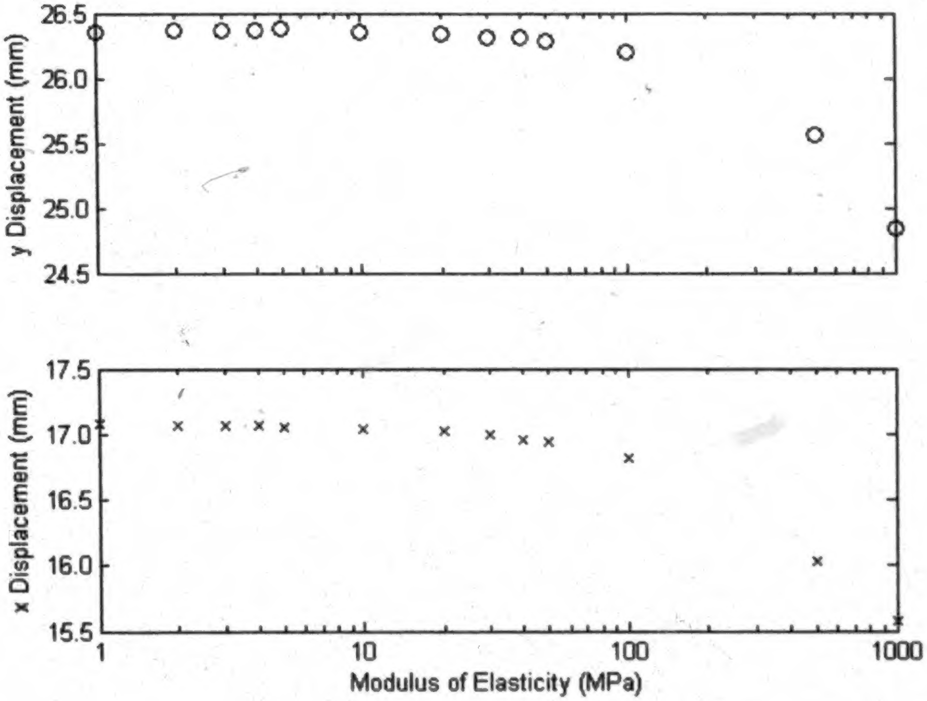

Figure 7.29: Deflection of nodes 634 (top graph) and 182 (bottom graph) using sternum to ground stiffnesses ranging from $E = 1\,\mathrm{MPa}$ to $E = 1000\,\mathrm{MPa}$.

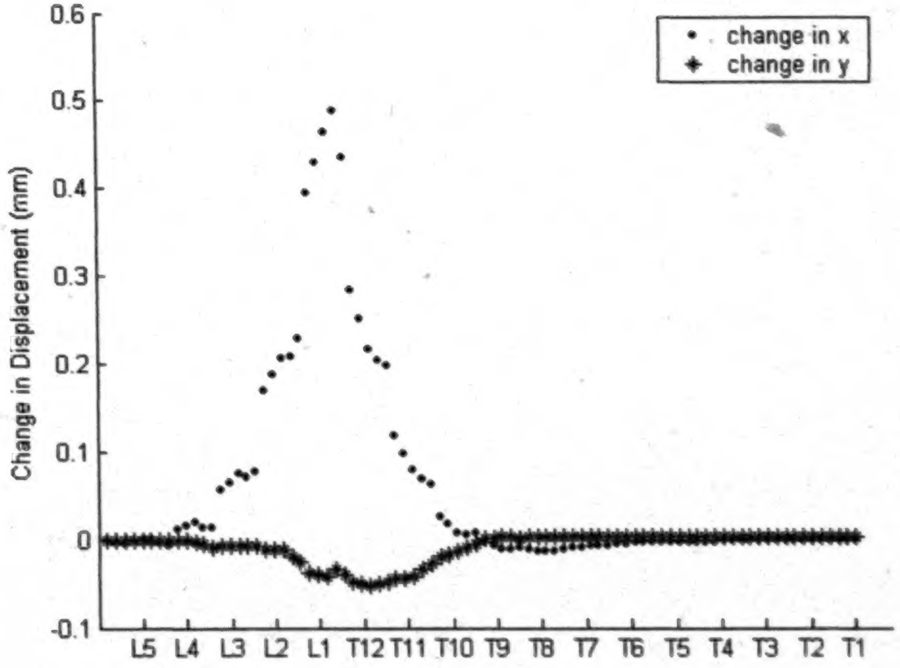

Figure 7.30: Change in deflection of the spine with and without contact elements (No Contact−Contact).

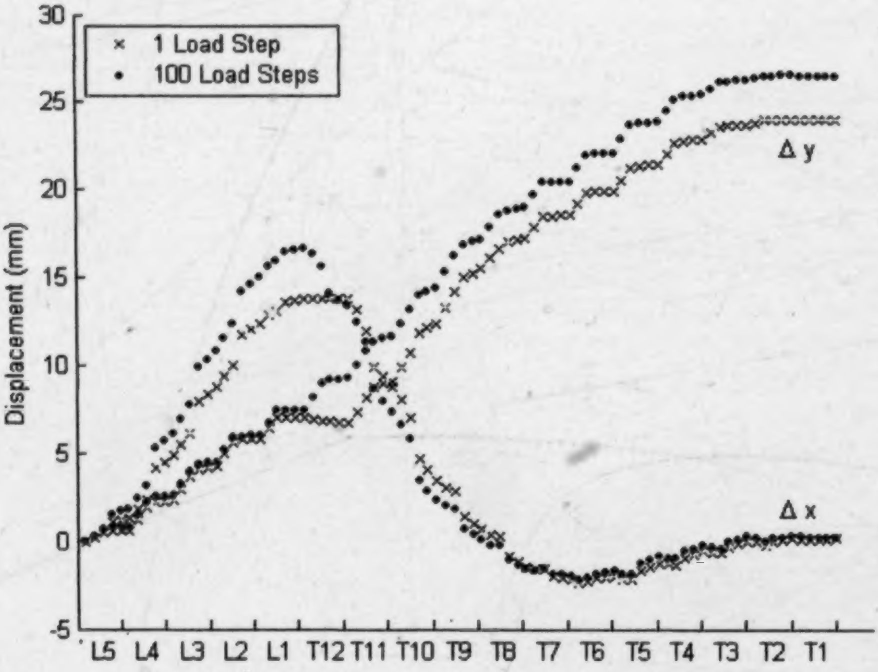

Figure 7.31: Centerline node deflections of the spine for 1 load step and 10 load steps.

nonlinear material properties of the ligaments, large deflection, and nonlinear force application.

In order to find an acceptable medium between the two values, the x and y displacements at nodes 182 and 634, respectively, were compared for differing numbers of load steps. The results are shown in Figure 7.32. Close inspection of both graphs revealed that little change in x or y occurred for a number of load steps greater than 10. Therefore, 10 load steps was deemed appropriate for this two-dimensional model.

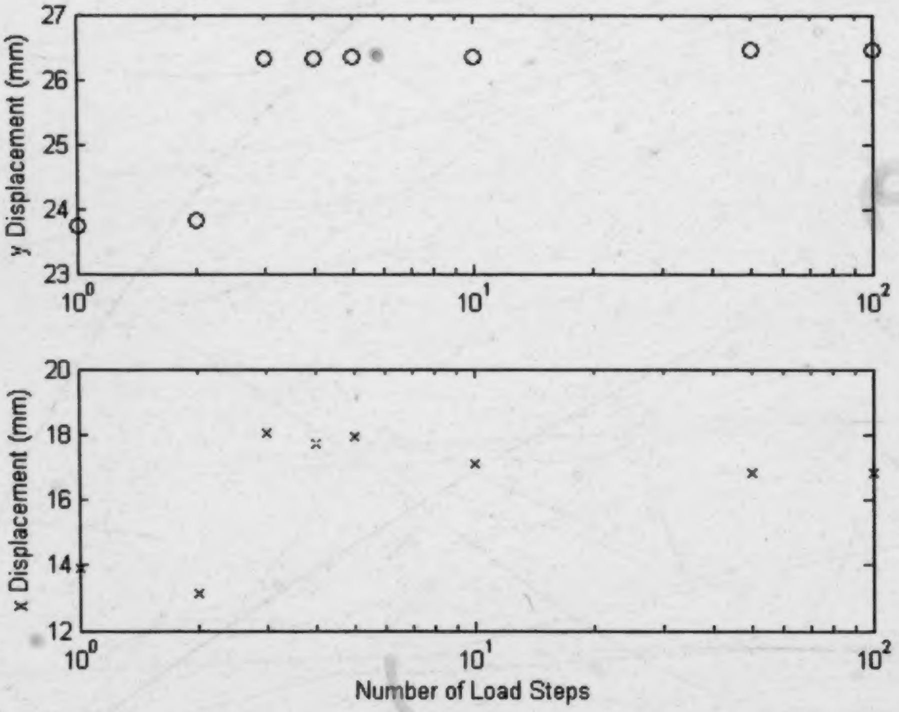

Figure 7.32: Calculated displacement of node 634 and 182 in the y and x directions respectively for a varying number of load steps.

7.4 Real Time Capabilities

Several methods, including condensation, sparse matrix storage, and boundary condition application were tested to try to decrease the computational requirements of the system. For these tests, the full model ($T1$ -$L5$) was used, with boundary constraints applied in x and y at the bottom of $L5$ for a total of 26 constraints. A single load of 200 N was applied to the left screw position on $L1$ over 10 load steps. The results of these tests are discussed below.

7.4.1 Condensation

While condensation itself does not affect the accuracy of a linear system, using condensation in conjunction with a nonlinear solver can. Using a Newton-Raphson solver, the element stiffness matrices are recalculated and reassembled following each load step. Due to time constraints, it would not make sense to recalculate the vertebrae stiffness matrices, then recondense them before assembling the global stiffness matrix and solving the model. However, because the vertebrae are relatively stiff compared to the remaining components of the spine, it was suggested that rotation matrices be used to update the super-element stiffness matrices following each load step. Contrary to using constraint equations to model the vertebral bodies (which would use this same assumption), this method does allow deflection of the vertebral bodies to be accounted for. The advantage of using this method is that the global stiffness matrix for the vertebrae do not need to be re-assembled after each load step. When used in conjunction with condensation, the time savings are significant.

Solving the test case, the femSpine solver time decreased by 57%, from 26.3 s to 11.3 s when condensation was used. The difference in displacement is illustrated in Figure 7.33. This error was found to be a maximum of 0.9 mm, or 5% located near the load application site and a median error of 0.06 mm. Note that while some of the error was a direct result of the error involved with updating the stiffness matrices, some secondary error occurred due to other nonlinear components, for instance, contact did not occur until after load step 9 using condensation as opposed to load step 7 without condensation.

The resulting condensation error is deemed acceptable for the resulting time savings, however, this test should be performed using the three-dimensional model to

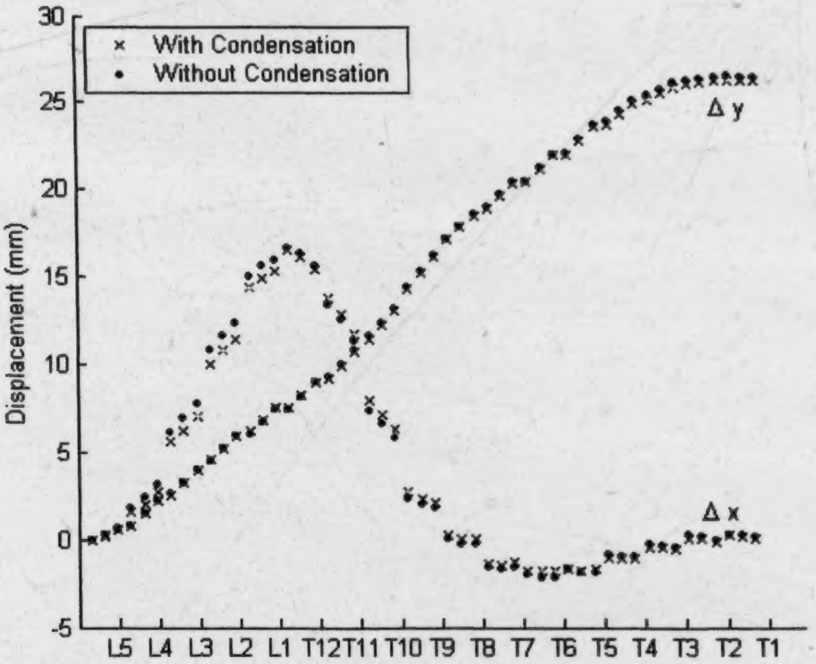

Figure 7.33: Plot of the spinal displacement with and without using condensed vertebrae stiffness matrices.

ensure the error is within an acceptable range. Note that condensation should only be used on the vertebral body and not the arch as studies have shown that the arch is not rigid in comparison to the remaining components of the spine.

7.4.2 Sparse Matrix Storage

Recall from Chapter 4 that a matrix stored using the built-in sparse matrix capabilities in Matlab will require less computational memory as long as the density of the matrix is less than two-thirds. Also recall that operations on sparse matrices require more computational time per element than full matrices. The unconstrained global stiffness matrix for the test run appears as shown in Figure 7.34. Note that the 17 black squares represent the condensed stiffness matrices for the vertebrae, the arrow head shaped nonzero elements at the bottom right represent the triangular articular facets and the ribcage, the bottom right diagonal elements represent the sternum, while the remaining elements joining the vertebra represent the intervertebral discs and intertransverse ligaments. The density of the 834 row by 834 column global stiffness matrix is 0.0361, which is well below the upper storage limit of two-thirds. Therefore, it is not surprising that the storage space for this sparse matrix is a mere 6% of the 5.3 megabytes of the storage space required for the full matrix. It also comes as no surprise that the computational requirements to solve the model decrease by almost 50% (from 21.8 s to 11.4 s) when using the sparse matrix storage for the global stiffness matrix. The final solution was verified to ensure that no error was added into the system using this storage method.

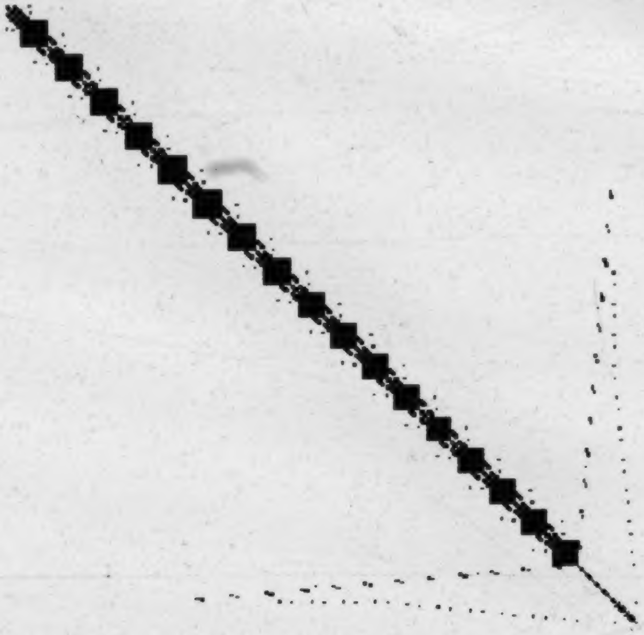

Figure 7.34: Illustration of the unconstrained global stiffness matrix for the test case.

On an interesting note, if the condensed vertebrae stiffness matrices are stored as sparse matrices (which, with a density of 1.0, they should not be), the total solution time increases by almost 40%. While an increase in operation time is expected due to the inefficiency of the sparse matrix operations in dealing with high density matrices, it was alarming at just how much extra time was required. This illustrates how important it is to ensure that the sparse matrix functions are only used where appropriate.

7.4.3 Application of Boundary Conditions

Upon observation of the femSpine solver report shown in Figure 7.35, it was observed that a relatively large amount of time was spend using Allaire's Method, discussed in Section 4.6.1, to apply the constraints to the model. Note that constraints are applied once for each load step, in addition to once for each Newton-Raphson iteration within each load step to clear the internal force vector at the boundary locations. This resulted in 780 calls (30 rounds of 26 constraints) to the constraints function, for a total time of 5.112 s, or 31% of the total solver time for the test case.

In an attempt to decrease the solver time, the test run was performed using the elimination method of applying constraints. The advantage of using this method is that it can be vectorized so that one command can eliminate all of the necessary rows or columns from the global stiffness matrix and then another line to eliminate the rows in the force vector. In addition, this method doesn't add any additional error into the system. Using the elimination method, the total time for constraint application decreased from 5.112 s to 0.1 s, resulting in a new solver time of 11.61 s, a 30% time savings! Note that the time to solve the global stiffness matrix did not change considerably by eliminating the 26 rows and columns (from 834 DOF to 808 DOF) so the time savings within the solve_equations function was negligible (0.65 s to 0.60 s).

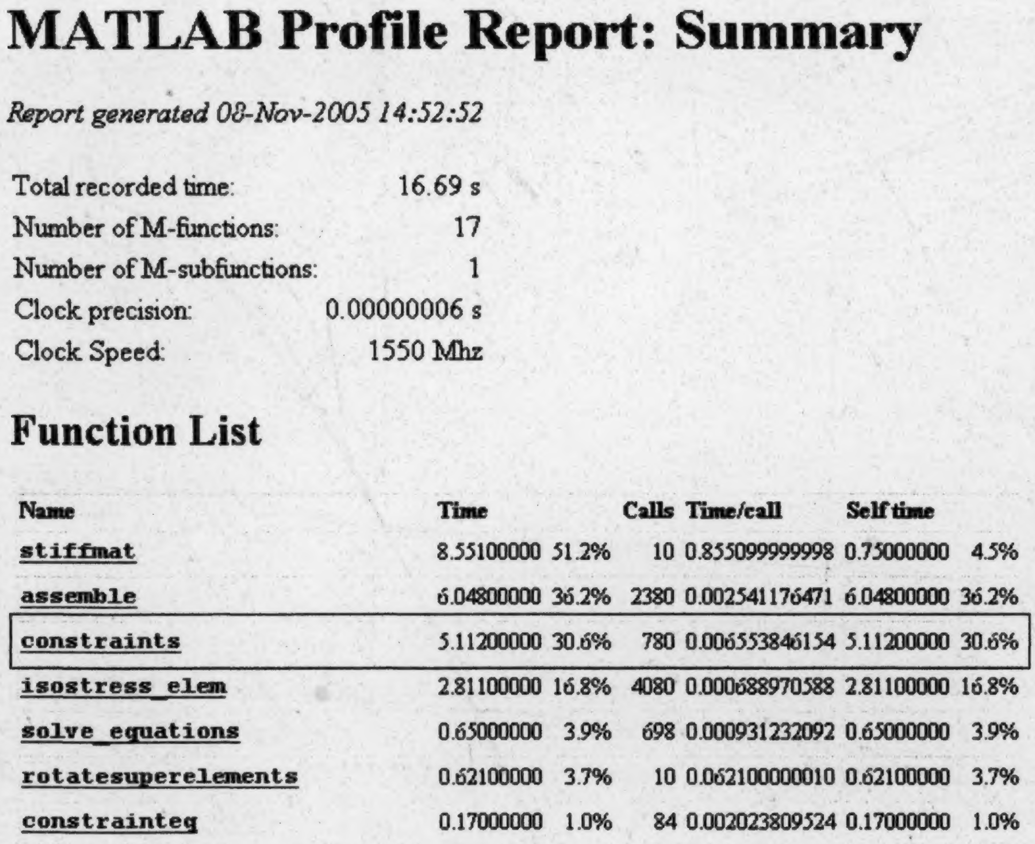

MATLAB Profile Report: Summary

Report generated 08-Nov-2005 14:52:52

Total recorded time:	16.69 s
Number of M-functions:	17
Number of M-subfunctions:	1
Clock precision:	0.00000006 s
Clock Speed:	1550 Mhz

Function List

Name	Time		Calls	Time/call	Self time	
stiffmat	8.55100000	51.2%	10	0.855099999998	0.75000000	4.5%
assemble	6.04800000	36.2%	2380	0.002541176471	6.04800000	36.2%
constraints	5.11200000	30.6%	780	0.006553846154	5.11200000	30.6%
isostress_elem	2.81100000	16.8%	4080	0.000688970588	2.81100000	16.8%
solve_equations	0.65000000	3.9%	698	0.000931232092	0.65000000	3.9%
rotatesuperelements	0.62100000	3.7%	10	0.062100000010	0.62100000	3.7%
constrainteq	0.17000000	1.0%	84	0.002023809524	0.17000000	1.0%

Figure 7.35: Modified profile report from Matlab.

Chapter 8

Discussion

8.1 Overview

A two-dimensional model of the scoliotic spine has been presented and provides the framework from which a complete three-dimensional pre-surgical tool can be built. Essential nonlinearities, including contact elements, nonlinear load application, nonlinear material properties, large deflection capabilities and nonlinear strain are all accounted for. In addition, several time saving features such as condensation and sparse matrix storage have been utilized. The code has been streamlined and vectorized where possible to create a fast and accurate solver. A user friendly interface allows loads and constraints to be manipulated easily, and access to several features to aid in viewing the scoliotic geometry and evaluating the model.

8.2 Conclusions

From the sensitivity analysis several conclusions can be made:

- The material properties of the vertebral bodies were not found to significantly affect spinal correction. Note that this model assumed uniform material properties while a more accurate model would include the ability to model cancellous bone for the center of the vertebrae. However, it is anticipated that, due to the relatively low sensitivity of the spinal deflection to the vertebral body material properties, that the differences in these models would be minimal. Therefore, at this time it can be concluded that patient specific material properties for the vertebral bodies do not need to be considered. However, testing will be required to determine if the same is true for the vertebral arch once the three-dimensional model is complete.

- The stiffness of the intervertebral discs was determined to be the most sensitive parameter tested. As such, enhanced modeling of the discs by including the nucleus pulposes is recommended. In addition, patient specific stiffness values may be required. Further studies should be completed to determine if these values can be obtained from the right and left bending test x-rays.
- The stiffness, prestress, and nonlinear strain of the intertransverse ligaments were insignificant to the spinal correction. However, these tests will need to be performed for the remaining six ligaments in the three-dimensional model before making a conclusion regarding the importance of patient specific properties. Note that accounting for prestress and nonlinear strain do not require significant time or memory storage and should therefore be accounted for regardless of the sensitivity of these components.
- The stiffness of the thoracic cage was found to affect spinal correction, particularly in the thoracic region. Due to the simplified model of the ribcage used in femSpine, further testing of the thoracic cage will also be required once the three-dimensional model is complete. A more complete understanding of the mechanics of the rib hump present in scoliotic patients is required to determine if patient specific geometry and material properties are required.
- The material properties of the sternum were not significant to spinal correction. This is due to the mechanics of the costo-vertebral and costo-transverse joints. As such, patient specific material properties of the sternum will not be required in the final model.
- The stiffness of the sternum to ground node does not appear to affect the spinal correction and therefore patient specific values should not be required.
- The contact elements were not found to contribute significantly to surgical correction in this model. However, the increased geometrical complexity of the

three-dimensional facet articulations may have a greater influence. In addition, articular facet geometry specific to scoliotic patients should be studied further and implemented in the model prior to further sensitivity analyses.

8.3 Future Work

While this project has been a huge step towards the final goal of creating preoperative tool for scoliosis surgery, many more advancements are required to meet that goal. The remaining work can be subdivided into four areas: expansion to a three-dimensional model of the spine, improving the model to better represent the scoliotic surgery, further increasing real time capabilities of the model, and modifying the program such that it can be used by surgeons. These areas will be discussed in detail in the following sections.

8.3.1 Expansion to a Three-dimensional Model

Using the existing two-dimensional finite element framework, the conversion into a three-dimensional model will require creating the three-dimensional spinal geometry, defining the corresponding discretization, and developing code for the three-dimensional elements. The spinal geometry should include three-dimensional vertebral bodies with a separate vertebral arch, all spinal ligaments, and a complex ribcage model complete with the ability to represent the rib hump. Axial rotation and axial deformation of the spine must also be built in to the model.

Some minor changes will also be required in the program to allow for the advancement to three dimensions. These improvements include improving the graphical representation of the model, enabling three-dimensional forces to be created, and enabling boundary conditions in the new plane. These changes should be relatively easy to implement as the code was created with the intent of eventually allow three-dimensional analysis.

In addition, it is strongly suggested that the constraint equations be updated to implement the augmented Lagrangian method[3], which is a combination of the currently used penalty method and Lagrangian multipliers. This method is preferred for use with an iterative solver as it is more stable.

8.3.2 Improved Modeling of Scoliotic Surgery

Further enhancement will then be necessary to improve the model's representation of the scoliotic surgery. These improvements can be further divided into improving the scoliotic geometry and improved representation of the surgical procedures. Once these improvements, discussed in detail below, have been made, further sensitivity analyses should be conducted.

Scoliotic Geometry

The results obtained from the pre-operative tool are only as useful as the information put into it. It is therefore imperative that patient specific geometry and material properties be used to create each model. It is anticipated that digital x-rays will enable the creation of patient specific geometry in the near future. However, this may not provide the initial geometry required by the pre-operative tool. In a recent study, partial correction of the scoliotic deformity was shown prior to instrumentation of the spine[5]. This correction, measured to be a mean of 10 degrees, is due to the patient's positioning during the surgery and the muscle stripping to expose the spine. Obviously, this change in geometry will also need to be estimated for each patient. Further analysis and study may be required to adequately account for this occurrence. Patient specific material properties will also be difficult to obtain. Once a three-dimensional prototype has been created, sensitivity testing should enable one to determine which material properties play a significant role in the surgical outcome. This will hopefully shape future research into determining those unknown properties.

An improved representation of the articular facets is also required to improve the scoliotic model. The anatomical facet orientation should be accounted for and constraints should be created to allow slipping movement within the articular joint, instead of just gluing nodes together. Note that a frictional force is not necessary as the synovial fluid within the joint is known to minimize frictional forces[36].

The anatomy of the intervertebral discs should also be better modeled, perhaps through the use of a compression only spring in center to model nucleus.

Finally, a mesh which allows for the differentiation of cortical and cancellous bone may be necessary for the vertebrae and ribcage. Three-dimensional sensitivity analyses should determine whether this step is crucial to achieving accurate results.

Surgical Procedures

Several steps need to be taken to better account for the surgical procedures. The patient specific geometry and material properties used must account for the patient lying down and the effect of the anaesthetic during surgery. More appropriate boundary conditions should be explored due to patient loading and traction on operating table. In addition, the forces on the spine should be added one after another in the order they are applied during surgery.

Further Tests

Sensitivity tests will be necessary to determine future modifications to the model. For example, a sensitivity analysis on the impact of the articular facets could determine if they can be simplified or omitted to decrease computational time and memory. Further tests will also be required to determine if more load steps will be required to accurately solve the three-dimensional model.

In addition, once a three-dimensional model has been created, tests should be performed to compare the model with surgical data currently being obtained.

8.3.3 Real Time Capabilities

The main purpose of the finished pre-surgical tool is to allow the surgeon to test multiple loading configurations for each patient. As such, a faster solver will allow the surgeon to perform a greater number of test runs. To estimate the time requirements for the final model, the number of elements required for the model was estimated as shown in Table 8.1. Two methods, discussed below, were used to approximate the time requirements for the three-dimensional model.

The first estimate is a crude approximation based on the increase in the femSpine solver time by increasing the number of spinal units. As shown in Figure 8.1, for a number of elements greater than 150, a linear relationship appears between the solver time and number of elements. Extrapolating this relationship to the estimated 1100 elements required for the three-dimensional model results in a solver time of 67 s.The second estimate is based on the current profile report generated in Matlab® and extrapolating these values. For the current two-dimensional model with condensation, the assembly of the global stiffness matrix takes up 53% of the 11.3 s required to solve

Table 8.1: Number of Elements Required for Three-dimensional Model

	Elements/Unit	**Units**	**Total Elements**
Vertebral Body	1	17	17
Vertebral Arch	10	17	170
Articular Facets	1	17 × 2	34
Intervertebral Discs	32	17	544
Spinal Ligaments	1	7 × 17 × 2	238
Ribs	1	10 × 2	20
Costal Ligaments	1	10 × 2 × 3	60
Sternum	1	6	6
Total			1089

the model. There are 2380 calls to the *assemble.m* subprogram, one for each element per load step (238 elements and 10 load steps). With the total number of elements estimated to be approximately 1100, this would require 11000 calls to the assemble.m program, for a total time requirement of 27.9 s. In addition, a total of 3.73 s was used to create the elemental stiffness matrices, therefore, assuming 1100 elements, the new estimate would be 17.3 s. The total time required to solve the finite element equations was extrapolated linearly to 1.2 s. The remaining components, accounting for 1.0 s are not expected to increase significantly for the three-dimensional model. However, because the model is becoming larger and more complex, the model may require more iterations to satisfy the error tolerances. Therefore, the estimated time requirement for the three-dimensional Matlab® model is approximately 50 s.

Once the three-dimensional Matlab model is complete, the code should be reformatted into a stand alone executable program. Since this program will not require Matlab® to be running in the background, additional time savings are expected. In addition, the current model is being run on a four year old computer with a 1.54 GHz processor and 512MB of RAM. It is expected that the final model will be run on a much faster computer which will allow for an even better processing time. It is hoped that the final model will be solved easily in under 30 s. This should allow the surgeon to perform multiple tests in just a few minutes time.

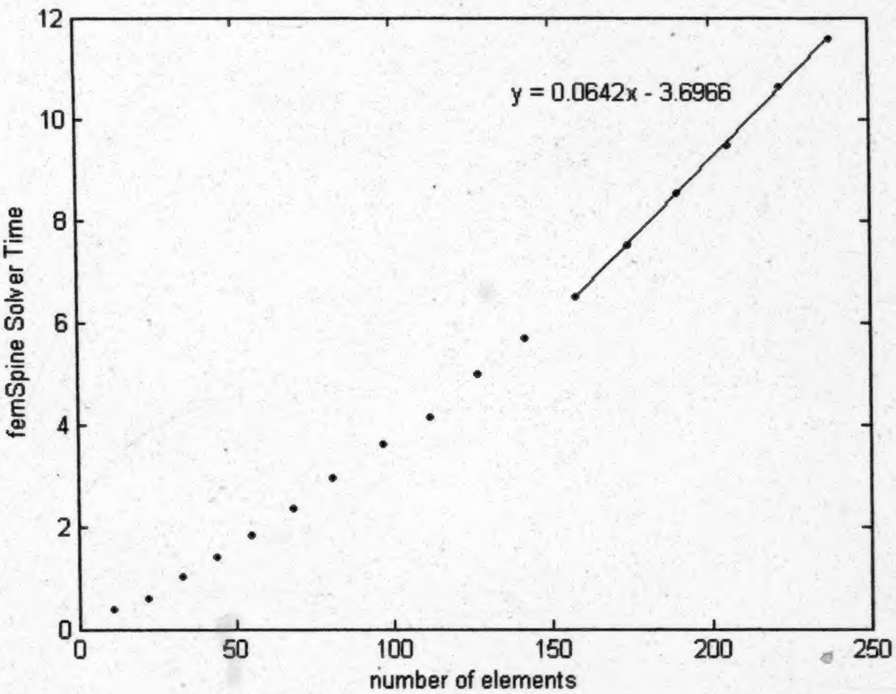

Figure 8.1: Current time requirements to solve femSpine for an increasing number of elements.

8.3.4 Improve ease of use by Surgeons

Ultimately, the model must be user friendly so that the surgeons will use it. While this will mainly involve creating a graphical user interface that is straight forward, several other tools will also make the program easier to use. The creation of a software tool to define the size and shape of the surgical rod in addition to the contact points with the spine and the order of attachment will increase the surgeon's ability to manipulate the spine without knowledge of the exact forces being applied. A database storing all of the previous tests and results could help the user to look up similar test cases and the optimal method of correction. Ultimately, an optimization that would determine the best hook and screw placement to minimize forces and stresses while maximizing correction would be quite effective.

While a considerable amount of work remains, the final goal of a pre-surgical tool is well within reach. This tool will not only eliminate the dependence on the surgeon's experience, but will allow the testing of several different surgical procedures for individual cases. This will ultimately benefit those individuals suffering from scoliosis.

Bibliography

[1] ANSYS *User's Manual Ansys* Revision 5.6.1, USA, 1999

[2] Aubin C.E., Descrimes J.L., Dansereau J., Skalli W., Lavaste F., Labelle H., Modelisation geometrique du rachis et du thorax pour l'analyse biomechanique par elements finis des deformations scoliotiques. *Annales de Chirurgie* V49, pp 749-761, 1995

[3] Bathe K.J, *Finite Element Procedures.* Prentice Hall, New Jersey, 1996

[4] Beer F.P., Johnston E.R., *Mechanics of Materials*, Second Edition. McGraw-Hill Book Company Europe, England, 1992

[5] Behairy Y.M., Hauser D.L., Hill D., Mahood J., Moreau M., Partial Correction of Cobb Angle Prior to Posterior Spinal Instrumentation, *Annals of Saudi Medicine*, Vol 20, N 5-6, pp398-401, 2000

[6] Boresi A.P., Schmidt R.J., Sidebottom O.M., *Advanced Mechanics of Materials.* John Wiley & Sons, USA, 1993

[7] Bradford, Lonstein, Ogilvie, Winter, *Moe's Textbook of Scoliosis and Other Spinal Deformities*, Second edition, W.B. Saunders Company, 1987

[8] Chandrupatla T.R., Belegundu A.D., *Introduction to Finite Elements in Engineering*, Third Edition. Prentice Hall, New Jersey, 2002

[9] Cook R.D., Malkus D.S., Plesha M.E., Witt R.J., *Concepts and Applications of Finite Element Analysis*, Fourth Edition. John Wiley & Sons, USA, 2002

[10] Crisfield M.A., *Non-linear Finite Element Analysis of Solids and Structures, Volume 1: Essentials.* John Wiley & Sons, England, 1991

[11] Fyfe K.R. *MecE 563 Finite Element Analysis for Mechanical Engineers.* University of Alberta, 2002

[12] Gardner-Morse M., Stokes I.A.F. Three-dimensional simulations of the scoliosis derotation maneuver with Cotrel-Dubousset instrumentation. *J. of Biomechanics* 27(2) pp 177-181, 1994.

[13] Harrington, P.R. Treatment of scoliosis, correction and internal fixation by spine instrumentation. *J Bone Joint Surgery* 44A:591-610, 1962

[14] Integrated Publishing http://www.tpub.com

[15] Kapandji, I.A., *The Physiology of the Joints Volume 3: Thr Trunk and Vertebral Column*, Second edition, Churchill Livingstone, USA, 1974

[16] Keim, H.A., *The Adolescent Spine* Second Edition, Springer-Verlag New York, 1982

[17] King, H.A., Moe, J.H., Bradford, D.S. The Selection of Fusion Levels in Thoracic Idiopathic Scoliosis *J. Bone Joint Surg.* Vol 65, pp1302-13, 1983

[18] MATLAB, Version 6.5.0 The MathWorks, Inc, 2002

[19] Martini F.H., Fundamentals of Anatomy & Physiology, Fifth Edition, Prentice Hall, New Jersey, 2001

[20] Mondoux J. Surgical Forces. *Personal Communication* Glenrose Rehabilitation Hospital, Alberta

[21] Myklebust, J. Pintar, F. Yoganandan N. Cusiak J.F., Maiman D., Myers M., and Sances A. Tensile Strength of Spinal Ligaments *Spine* Vol 13 Num 5, pp 527-31, 1988

[22] Netter, F.H., *Atlas of Human Anatomy*, CIBA-CEIGY Corporation, Summit, New Jersey, 1989

[23] Panjabi M.M., Goel V, Oxland T., Takata K. Human Lumbar Vertebrae, Quantitative Three-Dimensional Anatomy *Spine,* Vol 17, No 3, pp.299-306, 1992

[24] Panjabi M.M., Oxland T., Takata K., Goel V., Durnaceau J., Krag M. Articular Facets of the Human Spine - Quantitative Three-Dimensional Anatomy *Spine* Vol 18, No 10, pp 1298-1310, 1993

[25] Panjabi M.M., Takata K., Goel V., Federico D. Thoracic Human Vertebrae, Quantitative Three-Dimensional Anatomy Spine Vol 16, No 8, pp 888-901, 1990

[26] Papin P., Labelle H., Delorme S., Aubin C.-E., deGuise J.A., Dansereau J. Long-term three dimensional changes of the spine after posterior spinal instrumentation and fusion in adolescent idiopathic scoliosis *Eur Spine J* Vol 8, pp. 16-21, 1999

[27] Plouznikoff A., Aubin CE., Ozell B., Labelle H., Virtual Reality Scoliosis Surgery Simulator. *International Research Society of Spinal Deformities Symposium* 2004

[28] Pope M., Stokes I., Moreland M. The Biomechanics of Scoliosis, *CRC Critical Reviews in Biomedical Engineering*, Vol 11, Issue 3, pp. 157-188, 1984

[29] Skalli W., Robin S., Lavaste F., Dubousset J. A Biomechanical Analysis of Short Segment Spnal Fixation Using a Three-Dimensional Geometric and Mechanical Model, *Spine* Vol 18 pp. 536-545, 1993

[30] Spine-Heath.com http://www.spine-health.com

[31] Stokes I.A.F., Aronsson D.D. Disc and Vertebral Wedging in Patients With Progressive Scoliosis, *J of Spinal Disorders* Vol 14 pp 317-322, 2001

[32] Sundaram S.H., Feng C.C. Finite Element Analysis of the Human Thorax. *J of Biomechanics* 10, 505-516 1977

[33] Tamaki T., Jin H.M., Takahashi K., Kotani T., Akazawa T., Moriya H. Simulation of Reconstruction Surgery of Scoliosis by Finite Element Modelling *International Research Society of Spinal Deformities Symposium* 2004

[34] Tamaki T. Details Regarding Articular Facet Modeling and Time Requirements. *Personal Communication* Miyashiro, Saitama, Japan

[35] Thompson J.M. *A Finite Element Model of the Rib Cage.* Thesis, University of Alberta, 1995

[36] Tong S. *A Mechanical Model of the Normal Human Spine.* Thesis, University of Alberta, 1999

[37] White A.A. and Pajabi M.M. *Clinical Biomechanics of the Spine*, Second Edition. J.B. Lippincott, Philadelphia, PA 1990

[38] Young Y.C., Budynas R.G. *Roark's Formulas for Stress and Strain*, Seventh Edition, McGraw-Hill, USA, 2002

[39] Zeller R.D., Dubousset J. CD Horizon Surgical Technique for Posterior Scoliosis Correction. *SRS spinal deformities handbook* p 1-9, 1996

Appendix A

Element Derivations

A.1 Nonlinear Strain-Displacement Truss Element

To account for large deflection, the nonlinear strain-displacement equation for a truss should be used[6]:

$$\varepsilon_{xx} = \frac{\partial u}{\partial x} + \frac{1}{2}\left(\frac{\partial u}{\partial x}\right)^2 \tag{A.1}$$

Therefore, strain energy equation is now written as

$$\begin{aligned} U &= \frac{AE}{2}\int_0^\ell \left(\frac{\partial u}{\partial x} + \frac{1}{2}\left(\frac{\partial u}{\partial x}\right)^2\right)^2 dx && \text{(A.2)} \\ &= \frac{AE}{2}\int_0^\ell \left(\left(\frac{\partial u}{\partial x}\right)^2 + \left(\frac{\partial u}{\partial x}\right)^3 + \frac{1}{4}\left(\frac{\partial u}{\partial x}\right)^4\right) dx && \text{(A.3)} \end{aligned}$$

Evaluation of the strain energy equation results in the following stiffness matrix[10]:

$$k = \frac{AE}{\ell}\begin{bmatrix} 1 & -1 \\ -1 & 1 \end{bmatrix} + \frac{2AE}{\ell^2}u_{21}\begin{bmatrix} 1 & -1 \\ -1 & 1 \end{bmatrix} + \frac{3AE}{2\ell^3}u_{21}^2\begin{bmatrix} 1 & -1 \\ -1 & 1 \end{bmatrix} \tag{A.4}$$

where u_{21} is a shorthand notation for the element deflection, $u_2 - u_1$

A.2 Nonlinear Strain-Displacement Beam Element

Assuming a uniform elastic beam, one can show that

$$\begin{aligned} EI\frac{d^2v}{dx^2} &= \underbrace{M(x)}_{\text{Moment}} \\ EI\frac{d^3v}{dx^3} &= \underbrace{V(x)}_{\text{shear force}} \\ EI\frac{d^4v}{dx^4} &= \underbrace{p(x)}_{\text{distributed load}} \end{aligned}$$

We also know that

$$\begin{aligned} \sigma_{bending} &= -\frac{My}{I} \\ &= -EI\frac{d^2v}{dx^2}\frac{y}{I} \end{aligned}$$

Since, for elastic deflections $\sigma = E\varepsilon$,

$$\varepsilon_{bending} = -\frac{d^2v}{dx^2}y$$

The nonlinear strain-displacement equation for an axially loaded beam can be written as

$$\varepsilon_{xx} = \frac{\partial u}{\partial x} + \frac{1}{2}\left[\left(\frac{\partial u}{\partial x}\right)^2 + \left(\frac{\partial v}{\partial x}\right)^2\right]$$

Therefore,

$$\varepsilon = \frac{\partial u}{\partial x} + \frac{1}{2}\left(\frac{\partial u}{\partial x}\right)^2 + \frac{1}{2}\left(\frac{\partial v}{\partial x}\right)^2 - \frac{d^2v}{dx^2}y$$

The strain energy can be written as

$$\begin{aligned} dU &= \frac{1}{2}\int_A \sigma\varepsilon dA \\ &= \frac{E}{2}\int_A \varepsilon^2 dA \end{aligned}$$

Therefore,

$$\begin{aligned} dU &= \frac{E}{2}\int_A \left(\frac{\partial u}{\partial x} + \frac{1}{2}\left(\frac{\partial u}{\partial x}\right)^2 + \frac{1}{2}\left(\frac{\partial v}{\partial x}\right)^2 - \frac{d^2 v}{dx^2} y \right)^2 dA \\ &= \frac{E}{2}\int_A \left(\begin{array}{l} \left(\frac{\partial u}{\partial x}\right)^2 + \frac{1}{4}\left(\frac{\partial u}{\partial x}\right)^4 + \frac{1}{4}\left(\frac{\partial v}{\partial x}\right)^4 + \left(\frac{d^2 v}{dx^2}\right)^2 y^2 \\ + \left(\frac{\partial u}{\partial x}\right)^3 + \left(\frac{\partial u}{\partial x}\right)\left(\frac{\partial v}{\partial x}\right)^2 - 2\left(\frac{\partial u}{\partial x}\right)\left(\frac{d^2 v}{dx^2}\right) y \\ +\frac{1}{2}\left(\frac{\partial u}{\partial x}\right)^2\left(\frac{\partial v}{\partial x}\right)^2 - \left(\frac{\partial u}{\partial x}\right)^2\left(\frac{d^2 v}{dx^2}\right) y - \left(\frac{\partial v}{\partial x}\right)^2\left(\frac{d^2 v}{dx^2}\right) y \end{array} \right) dA \end{aligned}$$

Noting that $\int_A y^2 dA = I$ and that $\int_A y dA = 0$ (because y is measured from the neutral axis)

$$\begin{aligned} dU &= \frac{EA}{2}\left(\frac{\partial u}{\partial x}\right)^2 + \frac{EI}{2}\left(\frac{d^2 v}{dx^2}\right)^2 + \frac{EA}{2}\left(\frac{\partial u}{\partial x}\right)^3 + \frac{EA}{2}\left(\frac{\partial u}{\partial x}\right)\left(\frac{\partial v}{\partial x}\right)^2 \\ &\quad + \frac{EA}{8}\left(\frac{\partial u}{\partial x}\right)^4 + \frac{EA}{8}\left(\frac{\partial v}{\partial x}\right)^4 + \frac{EA}{4}\left(\frac{\partial u}{\partial x}\right)^2\left(\frac{\partial v}{\partial x}\right)^2 \end{aligned}$$

When we include the entire length of the beam,

$$\begin{aligned} U &= \frac{EA}{2}\int_0^\ell \left(\frac{\partial u}{\partial x}\right)^2 dx + \frac{EI}{2}\int_0^\ell \left(\frac{d^2 v}{dx^2}\right)^2 dx + \frac{EA}{2}\int_0^\ell \left(\frac{\partial u}{\partial x}\right)^3 dx \\ &\quad + \frac{EA}{2}\int_0^\ell \left(\frac{\partial u}{\partial x}\right)\left(\frac{\partial v}{\partial x}\right)^2 dx + \frac{EA}{8}\int_0^\ell \left(\frac{\partial u}{\partial x}\right)^4 dx \\ &\quad + \frac{EA}{8}\int_0^\ell \left(\frac{\partial v}{\partial x}\right)^4 dx + \frac{EA}{4}\int_0^\ell \left(\frac{\partial u}{\partial x}\right)^2\left(\frac{\partial v}{\partial x}\right)^2 dx \end{aligned}$$

We require the displacements, $u = u(x)$, $v = v(x)$, $\phi = \phi(x) = \frac{dv}{dx}$. Using a linear function to solve for u and a cubic function to solve for v and ϕ

$$\begin{aligned} u(x) &= \alpha_1 + \alpha_2 \left(\frac{x}{\ell}\right) \\ v(x) &= \beta_1 + \beta_2 \left(\frac{x}{\ell}\right) + \beta_3 \left(\frac{x}{\ell}\right)^2 + \beta_4 \left(\frac{x}{\ell}\right)^3 \\ \phi(x) &= \beta_2 \frac{1}{\ell} + 2\beta_3 \frac{x}{\ell^2} + 3\beta_4 \frac{x^2}{\ell^3} \end{aligned}$$

Or,

$$u(x) = \underbrace{\begin{bmatrix} 1 & \frac{x}{\ell} \end{bmatrix}}_{\{g_x\}} \begin{Bmatrix} \alpha_1 \\ \alpha_2 \end{Bmatrix}$$

$$v(x) = \underbrace{\begin{bmatrix} 1 & \frac{x}{\ell} & \left(\frac{x}{\ell}\right)^2 & \left(\frac{x}{\ell}\right)^3 \end{bmatrix}}_{\{g_y\}} \begin{Bmatrix} \beta_1 \\ \beta_2 \\ \beta_3 \\ \beta_4 \end{Bmatrix}$$

$$\phi(x) = \begin{bmatrix} 0 & \frac{1}{\ell} & \frac{2x}{\ell^2} & \frac{3x^2}{\ell^3} \end{bmatrix} \begin{Bmatrix} \beta_1 \\ \beta_2 \\ \beta_3 \\ \beta_4 \end{Bmatrix}$$

Using the end conditions, we can solve for α_i, β_i

$$\begin{aligned} @x = 0,\ u = u_1,\ v = v_1,\ \phi = \phi_1 \Longrightarrow \quad & u_1 = \alpha_1 \\ & v_1 = \beta_1 \\ & \phi_1 = \frac{\beta_2}{\ell} \\ @x = \ell,\ u = u_2,\ v = v_2,\ \phi = \phi_2 \Longrightarrow \quad & u_2 = \alpha_1 + \alpha_2 \\ & v_2 = \beta_1 + \beta_2 + \beta_3 + \beta_4 \\ & \phi_2 = \beta_2 \frac{1}{\ell} + 2\beta_3 \frac{1}{\ell} + 3\beta_4 \frac{1}{\ell} \end{aligned}$$

Or,

$$\begin{Bmatrix} u_1 \\ u_2 \end{Bmatrix} = \underbrace{\begin{bmatrix} 1 & 0 \\ 1 & 1 \end{bmatrix}}_{H_1} \begin{Bmatrix} \alpha_1 \\ \alpha_2 \end{Bmatrix}$$

$$\begin{Bmatrix} v_1 \\ \phi_1 \\ v_2 \\ \phi_2 \end{Bmatrix} = \underbrace{\begin{bmatrix} 1 & 0 & 0 & 0 \\ 0 & 1/\ell & 0 & 0 \\ 1 & 1 & 1 & 1 \\ 0 & 1/\ell & 2/\ell & 3/\ell \end{bmatrix}}_{H_2} \begin{Bmatrix} \beta_1 \\ \beta_2 \\ \beta_3 \\ \beta_4 \end{Bmatrix}$$

Solving for $\{\alpha\}$ and $\{\beta\}$

$$\begin{Bmatrix} \alpha_1 \\ \alpha_2 \end{Bmatrix} = \begin{bmatrix} 1 & 0 \\ -1 & 1 \end{bmatrix} \begin{Bmatrix} u_1 \\ u_2 \end{Bmatrix}$$

$$\begin{Bmatrix}\beta_1\\ \beta_2\\ \beta_3\\ \beta_4\end{Bmatrix} = \begin{bmatrix}1&0&0&0\\ 0&\ell&0&0\\ -3&-2\ell&3&-\ell\\ 2&\ell&-2&\ell\end{bmatrix}\begin{Bmatrix}v_1\\ \phi_1\\ v_2\\ \phi_2\end{Bmatrix}$$

We need to determine $\frac{\partial u}{\partial x}$, $\frac{\partial v}{\partial x}$, $\frac{d^2 v}{dx^2}$

$$\begin{aligned}\frac{\partial u}{\partial x} &= \frac{\partial}{\partial x}\left(\{g_x\}^T\right)\{\alpha\}\\ &= \left\{\begin{matrix}0 & \frac{1}{\ell}\end{matrix}\right\}\{\alpha\}\\ &= \left\{\begin{matrix}0 & \frac{1}{\ell}\end{matrix}\right\}\begin{bmatrix}1&0\\ -1&1\end{bmatrix}\begin{Bmatrix}u_1\\ u_2\end{Bmatrix} = \left\{\begin{matrix}u_1 & u_2\end{matrix}\right\}\begin{bmatrix}1&-1\\ 0&1\end{bmatrix}\begin{Bmatrix}0\\ \frac{1}{\ell}\end{Bmatrix}\\ &= \frac{1}{\ell}\left\{\begin{matrix}-1 & 1\end{matrix}\right\}\begin{Bmatrix}u_1\\ u_2\end{Bmatrix} = \frac{1}{\ell}\left\{\begin{matrix}u_1 & u_2\end{matrix}\right\}\begin{Bmatrix}-1\\ 1\end{Bmatrix}\end{aligned}$$

$$\begin{aligned}\frac{\partial v}{\partial x} &= \frac{\partial}{\partial x}\left(\{g_y\}^T\right)\{\beta\}\\ &= \left\{\begin{matrix}0 & \frac{1}{\ell} & \frac{2x}{\ell^2} & \frac{3x^2}{\ell^3}\end{matrix}\right\}\{\beta\}\\ &= \left\{\begin{matrix}0 & \frac{1}{\ell} & \frac{2x}{\ell^2} & \frac{3x^2}{\ell^3}\end{matrix}\right\}\begin{bmatrix}1&0&0&0\\ 0&\ell&0&0\\ -3&-2\ell&3&-\ell\\ 2&\ell&-2&\ell\end{bmatrix}\begin{Bmatrix}v_1\\ \phi_1\\ v_2\\ \phi_2\end{Bmatrix}\\ &= \left\{\begin{matrix}v_1 & \phi_1 & v_2 & \phi_2\end{matrix}\right\}\begin{bmatrix}1&0&-3&2\\ 0&\ell&-2\ell&\ell\\ 0&0&3&-2\\ 0&0&-\ell&\ell\end{bmatrix}\begin{Bmatrix}0\\ \frac{1}{\ell}\\ \frac{2x}{\ell^2}\\ \frac{3x^2}{\ell^3}\end{Bmatrix}\\ &= \frac{1}{\ell^3}\left\{\begin{matrix}-6x\ell+6x^2 & 1-4x\ell^2+3x^2\ell & 6x\ell-6x^2 & -2x\ell^2+3x^2\ell\end{matrix}\right\}\begin{Bmatrix}v_1\\ \phi_1\\ v_2\\ \phi_2\end{Bmatrix}\\ &= \frac{1}{\ell^3}\left\{\begin{matrix}v_1 & \phi_1 & v_2 & \phi_2\end{matrix}\right\}\begin{Bmatrix}-6x\ell+6x^2\\ 1-4x\ell^2+3x^2\ell\\ 6x\ell-6x^2\\ -2x\ell^2+3x^2\ell\end{Bmatrix}\end{aligned}$$

$$
\begin{aligned}
\frac{d^2v}{dx^2} &= \frac{\partial^2}{\partial x^2}\left(\{g_y\}^T\right)\{\beta\} \\
&= \left\{\begin{array}{cccc} 0 & 0 & \frac{2}{\ell^2} & \frac{6x}{\ell^3} \end{array}\right\} \begin{bmatrix} 1 & 0 & 0 & 0 \\ 0 & \ell & 0 & 0 \\ -3 & -2\ell & 3 & -\ell \\ 2 & \ell & -2 & \ell \end{bmatrix} \begin{Bmatrix} v_1 \\ \phi_1 \\ v_2 \\ \phi_2 \end{Bmatrix} \\
&= \left\{\begin{array}{cccc} v_1 & \phi_1 & v_2 & \phi_2 \end{array}\right\} \begin{bmatrix} 1 & 0 & -3 & 2 \\ 0 & \ell & -2\ell & \ell \\ 0 & 0 & 3 & -2 \\ 0 & 0 & -\ell & \ell \end{bmatrix} \begin{Bmatrix} 0 \\ 0 \\ \frac{2}{\ell^2} \\ \frac{6x}{\ell^3} \end{Bmatrix} \\
&= \frac{1}{\ell^3}\left\{\begin{array}{cccc} -6\ell+12x & -4\ell^2+6x\ell & 6\ell-12x & -2\ell^2+6x\ell \end{array}\right\} \begin{Bmatrix} v_1 \\ \phi_1 \\ v_2 \\ \phi_2 \end{Bmatrix} \\
&= \frac{1}{\ell^3}\left\{\begin{array}{cccc} v_1 & \phi_1 & v_2 & \phi_2 \end{array}\right\} \begin{Bmatrix} -6\ell+12x \\ -4\ell^2+6x\ell \\ 6\ell-12x \\ -2\ell^2+6x\ell \end{Bmatrix}
\end{aligned}
$$

Putting this all together,

$$
\begin{aligned}
U &= \frac{EA}{2}\int_0^\ell \left(\frac{\partial u}{\partial x}\right)^2 dx + \frac{EI}{2}\int_0^\ell \left(\frac{d^2v}{dx^2}\right)^2 dx + \frac{EA}{2}\int_0^\ell \left(\frac{\partial u}{\partial x}\right)^3 dx \\
&\quad + \frac{EA}{2}\int_0^\ell \left(\frac{\partial u}{\partial x}\right)\left(\frac{\partial v}{\partial x}\right)^2 dx + \frac{EA}{8}\int_0^\ell \left(\frac{\partial u}{\partial x}\right)^4 dx \\
&\quad + \frac{EA}{8}\int_0^\ell \left(\frac{\partial v}{\partial x}\right)^4 dx + \frac{EA}{4}\int_0^\ell \left(\frac{\partial u}{\partial x}\right)^2 \left(\frac{\partial v}{\partial x}\right)^2 dx
\end{aligned}
$$

$$
\begin{aligned}
U = {} & \frac{EA}{2}\int_0^{\ell}\left(\frac{1}{\ell^2}U_1\left\{\begin{array}{c}-1\\1\end{array}\right\}\left\{\begin{array}{cc}-1 & 1\end{array}\right\}U_1^T\right)dx \\
& +\frac{EI}{2}\int_0^{\ell}\left(\frac{1}{\ell^6}U_2\left\{a_1^T\right\}\left\{a_1\right\}U_2^T\right)dx \\
& +\frac{EA}{2}\int_0^{\ell}\left(\frac{1}{\ell^3}U_1\left\{\begin{array}{c}-1\\1\end{array}\right\}U_1\left\{\begin{array}{c}-1\\1\end{array}\right\}\left\{\begin{array}{cc}-1 & 1\end{array}\right\}U_1^T\right)dx \\
& +\frac{EA}{2}\int_0^{\ell}\left(\frac{1}{\ell}U_1\left\{\begin{array}{c}-1\\1\end{array}\right\}\right)\left(\frac{1}{\ell^6}U_2\left\{a_2^T\right\}\left\{a_2\right\}U_2^T\right)dx \\
& +\frac{EA}{8}\int_0^{\ell}\left(\frac{1}{\ell^2}U_1\left\{\begin{array}{c}-1\\1\end{array}\right\}\left\{\begin{array}{cc}-1 & 1\end{array}\right\}U_1^T\right)^2dx \\
& +\frac{EA}{8}\int_0^{\ell}\left(\frac{1}{\ell^6}U_2\left\{a_2^T\right\}\left\{a_2\right\}U_2^T\right)^2dx \\
& +\frac{EA}{4}\int_0^{\ell}\left(\frac{1}{\ell^2}U_1\left\{\begin{array}{c}-1\\1\end{array}\right\}\left\{\begin{array}{cc}-1 & 1\end{array}\right\}U_1^T\right)^2\left(\frac{1}{\ell^6}U_2\left\{a_2^T\right\}\left\{a_2\right\}U_2^T\right)^2dx \\
& +\frac{EA}{30\ell}U_1\left\{\begin{array}{c}-1\\1\end{array}\right\}U_2\begin{bmatrix}36 & 3\ell & -36 & 3\ell\\ 3\ell & 4\ell^2 & -3\ell & -\ell^2\\ -36 & -3\ell & 36 & -3\ell\\ 3\ell & -\ell^2 & -3\ell & 4\ell^2\end{bmatrix}U_2^T
\end{aligned}
$$

where:

$$
\begin{aligned}
U_1 &= \left\{\begin{array}{cc}u_1 & u_2\end{array}\right\} \\
U_2 &= \left\{\begin{array}{cccc}v_1 & \phi_1 & v_2 & \phi_2\end{array}\right\} \\
a_1 &= \left\{\begin{array}{cccc}-6\ell+12x & -4\ell^2+6x\ell & 6\ell-12x & -2\ell^2+6x\ell\end{array}\right\} \\
a_2 &= \left\{\begin{array}{cccc}-6x\ell+6x^2 & 1-4x\ell^2+3x^2\ell & 6x\ell-6x^2 & -2x\ell^2+3x^2\ell\end{array}\right\}
\end{aligned}
$$

$$
\begin{aligned}
U \;=\; & \frac{EA}{2\ell} U_3 \begin{bmatrix} 1 & 0 & 0 & -1 & 0 & 0 \\ 0 & 0 & 0 & 0 & 0 & 0 \\ 0 & 0 & 0 & 0 & 0 & 0 \\ -1 & 0 & 0 & 1 & 0 & 0 \\ 0 & 0 & 0 & 0 & 0 & 0 \\ 0 & 0 & 0 & 0 & 0 & 0 \end{bmatrix} U_3^T \\
& + \frac{EI}{2\ell^3} U_3 \begin{bmatrix} 0 & 0 & 0 & 0 & 0 & 0 \\ 0 & 12 & 6\ell & 0 & -12 & 6\ell \\ 0 & 6\ell & 4\ell^2 & 0 & -6\ell & 2\ell^2 \\ 0 & 0 & 0 & 0 & 0 & 0 \\ 0 & -12 & -6\ell & 0 & 12 & -6\ell \\ 0 & 6\ell & 2\ell^2 & 0 & -6\ell & 4\ell^2 \end{bmatrix} U_3^T \\
& + \frac{EA}{30\ell^2} u_{21} U_3 \begin{bmatrix} 0 & 0 & 0 & 0 & 0 & 0 \\ 0 & 36 & 3\ell & 0 & -36 & 3\ell \\ 0 & 3\ell & 4\ell^2 & 0 & -3\ell & -\ell^2 \\ 0 & 0 & 0 & 0 & 0 & 0 \\ 0 & -36 & -3\ell & 0 & 36 & -3\ell \\ 0 & 3\ell & -\ell^2 & 0 & -3\ell & 4\ell^2 \end{bmatrix} U_3^T
\end{aligned}
$$

where:

$$U_3 = \{\; u_1 \quad v_1 \quad \phi_1 \quad u_2 \quad v_2 \quad \phi_2 \;\}$$

Using Castigliano's Theorem:

$$P_i = \frac{\partial U}{\partial q_i} \qquad i = 1, 2, \ldots, n$$

$$
\begin{aligned}
k \;=\; & \frac{EA}{\ell}\begin{bmatrix} 1 & 0 & 0 & -1 & 0 & 0 \\ 0 & 0 & 0 & 0 & 0 & 0 \\ 0 & 0 & 0 & 0 & 0 & 0 \\ -1 & 0 & 0 & 1 & 0 & 0 \\ 0 & 0 & 0 & 0 & 0 & 0 \\ 0 & 0 & 0 & 0 & 0 & 0 \end{bmatrix}\begin{Bmatrix} u_1 \\ v_1 \\ \phi_1 \\ u_2 \\ v_2 \\ \phi_2 \end{Bmatrix} \\
& + \frac{EI}{\ell^3}\begin{bmatrix} 0 & 0 & 0 & 0 & 0 & 0 \\ 0 & 12 & 6\ell & 0 & -12 & 6\ell \\ 0 & 6\ell & 4\ell^2 & 0 & -6\ell & 2\ell^2 \\ 0 & 0 & 0 & 0 & 0 & 0 \\ 0 & -12 & -6\ell & 0 & 12 & -6\ell \\ 0 & 6\ell & 2\ell^2 & 0 & -6\ell & 4\ell^2 \end{bmatrix}\begin{Bmatrix} u_1 \\ v_1 \\ \phi_1 \\ u_2 \\ v_2 \\ \phi_2 \end{Bmatrix} \\
& + \frac{EA}{30\ell^2}u_{21}\begin{bmatrix} 0 & 0 & 0 & 0 & 0 & 0 \\ 0 & 36 & 3\ell & 0 & -36 & 3\ell \\ 0 & 3\ell & 4\ell^2 & 0 & -3\ell & -\ell^2 \\ 0 & 0 & 0 & 0 & 0 & 0 \\ 0 & -36 & -3\ell & 0 & 36 & -3\ell \\ 0 & 3\ell & -\ell^2 & 0 & -3\ell & 4\ell^2 \end{bmatrix}\begin{Bmatrix} u_1 \\ v_1 \\ \phi_1 \\ u_2 \\ v_2 \\ \phi_2 \end{Bmatrix}
\end{aligned}
$$